

Deformation and Strength Analysis of Glass Structures by Classical Continuum Mechanics and Peridynamics

DISSERTATION

zur Erlangung des akademischen Grades

Doktoringenieur
(Dr.-Ing.)

von M.Sc. Olha Sukhanova

geboren am 21.08.1996 in Charkiw, Ukraine

genehmigt durch die Fakultät für Maschinenbau
der Otto-von-Guericke-Universität Magdeburg

Gutachter:

1. apl. Prof. Dr.-Ing. habil. Konstantin Naumenko
2. Prof. Dr.-Ing. Oleksiy Larin (KhPI Charkiw)

Promotionskolloquium am 27.08.2025

Zusammenfassung

Das dynamische Verhalten und die Festigkeit von Glasstrukturen stellen aufgrund der spröden Natur des Glases sowie seiner Empfindlichkeit gegenüber Mikrorissen und Verarbeitungsdefekten eine modellierungstechnische Herausforderung dar. Diese Herausforderungen sind in verschiedenen Anwendungsbereichen von praktischer Relevanz – darunter Architektur, Bau- und Fahrzeugtechnik, sicherheitskritische Infrastrukturen, Luft- und Raumfahrt sowie Photovoltaikmodule –, bei denen Zuverlässigkeit unter dynamischer und statischer Belastung essenziell ist. Dies motiviert das Ziel der vorliegenden Dissertation, das darin besteht, das Verständnis und die Prognosefähigkeit des Verformungs- und Schädigungsverhaltens von laminierten und monolithischen Glasstrukturen zu verbessern. Ziel ist es, die strukturelle Integrität durch eine vertiefte Analyse des Einflusses geometrischer Parameter, Materialeigenschaften und Fertigungsfehler zu erhöhen. Besonderes Augenmerk liegt auf der Untersuchung der Initiierung und Ausbreitung von Schädigungen, dem Einfluss von Defekten sowie den Rissmustern, die in Glaskomponenten auftreten.

Zur Untersuchung dieser Phänomene wird eine Kombination aus klassischer Kontinuumsmechanik und nichtlokaler Peridynamiktheorie eingesetzt. Während das elastische Verhalten von Glas mit der traditionellen Finite-Elemente-Methode analysiert werden kann, erfordert die Modellierung der Schädigungsinitiierung und -ausbreitung die Anwendung der Peridynamik.

Für die numerische Untersuchungen des Glaslaminats bei einer Stoßbeanspruchung werden dreidimensionale Finite-Elemente-Modelle eingesetzt. Dabei dient die Modalanalyse zur Bestimmung der Eigenfrequenzen und Eigenschwingungsformen, während explizite dynamische Simulationen das zeitabhängige Verhalten bei unterschiedlichen Aufprallgeschwindigkeiten erfassen. Netzkonvergenzanalysen und parametrische Studien werden durchgeführt, um die Genauigkeit der Ergebnisse zu gewährleisten. In einer systematischen Parameterstudie wird der Einfluss geometrischer und materialbezogener Eigenschaften – einschließlich der Plattenkrümmung und der Dicke der Zwischenschicht – auf die Verformung und Spannungsverteilung untersucht.

Die Studie konzentriert sich zudem auf die Initiierung und Entwicklung von Schädigungen in monolithischen Glasplatten unter quasi-statischer Belastung. Hierzu werden Peridynamik-Modelle entwickelt und mit Finite-Elemente-Simulationen verglichen, um die Auswirkungen der Modelldiskretisierung und der Gitterkonfiguration im Rahmen elastischer quasi-statischer Verformungen zu untersuchen.

Der Einfluss der kritischen Dehnungswerts der Bindungen wird auf das Bruchverhalten von Glas unter koaxialer Doppelring-Biegung untersucht. Dabei werden sowohl homogenisierte Modelle mit einheitlichen kritischen Dehnungswerten als auch Modelle berücksichtigt, die Oberflächenschwächungseffekte einbeziehen. Bei einer Abminderung des kritischen Dehnungswerts an der Oberfläche zeigt sich eine Veränderung des Schädigungsmusters: von ausgeprägten radialen Rissen hin zu einer verteilten Zone von Oberflächenmikrorissen.

Das dynamische Bruchverhalten von Glasstrukturen wird mittels peridynamikbasierter Simulationen von Stahlkugel-Falltests untersucht. Die Empfindlichkeit des Schadensverhaltens gegenüber Eigenschaften geschwächter Schichten wird bewertet.

Der Einfluss technologischer Defekte (Oberflächenfehler) auf Bruchkraft, Schadensmuster und Rissausbreitung in Glasplatten wird untersucht. Die Auswirkungen von Defektgröße, -position und -dichte werden analysiert und mit experimentellen Daten aus der Literatur verglichen. Zufällig verteilte Defekte werden im peridynamischen Modell eingeführt und untersucht, um realistische Fertigungsschwankungen abzubilden.

Die rechnerischen Fortschritte dieser Arbeit liefern Richtlinien für die Modellierung von Verbundglas und erhöhen die Zuverlässigkeit der Bewertung unter quasi-statischen und dynamischen Belastungen.

Abstract

The dynamic behavior and fracture performance of glass structures represent modeling challenges due to the brittle nature of glass and its sensitivity to micro-cracks and technological imperfections. These challenges are of practical relevance across various applications, including architecture, structural and automotive engineering, safety-critical infrastructure, aerospace, and photovoltaic panels, where reliability under dynamic and static loads is essential. The mentioned motivates the current thesis aim, which focuses on improving the understanding and predictive capabilities of how laminated and monolithic glass structures deform and damage. The scope is to enhance structural integrity through a deeper analysis of the influence of geometric parameters, material properties, and manufacturing flaws. Special focus is given to studying the initiation and propagation of damage, the influence of flaws, and the cracking patterns occurring in glass components.

A combination of classical continuum mechanics and nonlocal peridynamic theory is employed to address these phenomena. While the elastic behaviour of glass can be analyzed using the traditional finite element method, modeling the initiation and propagation of damage requires the application of peridynamic theory.

An analysis of laminates subjected to impact loading, employing the finite element method in a three-dimensional framework, is carried out. Modal analysis is conducted to extract natural frequencies and eigenmodes, while explicit dynamic simulations capture the transient response under varying impact velocities. Mesh convergence studies and parametric analyses are performed to ensure the accuracy of the results. A systematic parametric study evaluates the influence of geometric and material properties, including plate curvature and interlayer thickness, on deformation and stress distribution.

The study also focuses on the initiation and evolution of damage in monolithic glass plates subjected to quasi-static loading. Peridynamic models are developed and compared with finite element simulations to examine the effects of model discretization and lattice configuration within the framework of elastic quasi-static deformation.

The influence of critical bond stretch value on glass fracture behavior under coaxial double-ring bending is studied. Homogenized models with uniform critical bond stretches and models accounting for surface weakening effects are considered. With the reduction of the critical bond stretch on the surface, a change in the damage pattern from distinct radial cracks to distributed region of surface micro-cracking with an almost smooth damaged zone is observed.

The dynamic fracture behavior of glass structures is analyzed using peridynamic-based simulations of steel ball drop tests. The sensitivity of weakened layer properties on damage behavior is evaluated.

The influence of technological flaws (surface defects) on fracture force, damage patterns, and crack propagation of glass plates is examined. The effect of flaw size, location, and density is analyzed and compared with experimental data from the literature. Randomly distributed imperfections are introduced and studied in the peridynamic framework to reflect realistic manufacturing variability.

The computational advancements of this work provide guidelines for modeling laminated glass, enhancing impact resistance, improves the reliability assessment under quasi-static and impact loads.

Contents

Figures	vii
Tables	xi
Nomenclature	xiii
1 Introduction	1
1.1 General information	1
1.2 Mechanical behavior of glasses and glass structures	4
1.3 Modeling approaches	8
1.4 Problem statement and outline of the thesis	13
2 Theoretical Background	17
2.1 Methodology of modeling	17
2.2 Modeling in framework of finite element method	17
2.2.1 Structural analysis	17
2.2.2 Determination of natural frequencies and eigenmodes	23
2.2.3 Forced and contact loading	24
2.2.4 Explicit dynamic analysis	26
2.3 Modeling using peridynamic theory	29
2.3.1 Basic formulation of linear peridynamic solid model	29
2.3.2 Damage and fracture modeling	31
3 Finite element modeling of laminated glasses under dynamic loading	33
3.1 Finite element model development and verification within linear modal and impact benchmarks	33
3.1.1 Monolithic glass plate benchmarks	33
3.1.2 Laminated glass finite element model accuracy estimation	39
3.2 Analysis of the influence of geometric parameters on laminated glass dynamics	44
3.3 Linear dynamic properties in curved laminated glasses	52
3.4 Deformation of laminated composite panels with different glass curvatures under impact loading	54
3.5 Influence of interlayer elasticity on laminated glass dynamics	57
4 Peridynamic modeling of glass plates	65
4.1 Discretization and boundary conditions	65
4.2 The influence of node lattice type and density	66
4.3 Comparative study based on peridynamic and finite element analysis	71
5 Analysis of damage and crack patterns	75
5.1 Influence of critical bond stretch parameter under quasi-static loading	75
5.2 Influence of critical bond stretch parameter under impact loading	81

5.3	Influence of initial defects (flaws) on fracture force, damage and crack patterns	88
5.4	Comparison with experimental data	96
5.4.1	Damage initiation modeling	96
5.4.2	Analysis of damage patterns	99
5.4.2.1	Quasi-homogeneous plate with mean value of critical bond stretch	100
5.4.2.2	Plate with initial imperfections at various locations	100
5.4.2.3	Plate with lower strength skin layer	102
5.5	Influence of the random distribution of defects (flaws) on fracture force, damage and crack patterns	103
6	Summary and Outlook	107
	References	113

Figures

1.1	Examples of damaged glass components	1
1.2	Laminated glass (LG)	2
1.3	Surface flaw distribution, after [70]	7
1.4	Modeling approaches	13
2.1	Material points interaction	29
2.2	Peridynamic deformation state	30
3.1	Simulation model	34
3.2	Mesh size of the model. a) 95.7 mm, b) 12.76 mm, c) 3.19 mm	35
3.3	Natural plate modes according to frequencies. a) first frequency number (FN), b) third FN, c) fourth FN, d) fifth FN, e) sixth FN, f) seventh FN	36
3.4	Dependence of the contact force on time	37
3.5	Dependence of the plate displacement u_z on time. a) at point (a/2, b/2), b) at point (a/2, b/4), c) at point (a/4, b/4)	38
3.6	Dependence of the stress tensor component σ_{xx} of the plate on time at point (a/4, b/4)	39
3.7	LG boundary conditions	40
3.8	Mesh sizes of the model. a) 10 mm, b) 5 mm, c) 2 mm	41
3.9	Dependence of the total displacements on mesh size	43
3.10	The magnitude of the displacement vector of LG with 0.38 mm PVB interlayer with the ball free-fall velocity 3 m/s	44
3.11	Dependence of u_{max} on v_b and h_{int}	44
3.12	First principal stress of LG with 0.38 mm PVB interlayer with the ball free-fall velocity 3 m/s	46
3.13	Dependence of σ_1 in t_{max} on v_b and h_{int}	46
3.14	First principal strain of interlayer with 0.38 mm thickness with the ball free-fall velocity 3 m/s. a) $t = 0.025$ ms, b) $t = 0.2$ ms, c) $t = 1.0$ ms, d) $t = 1.5$ ms, e) $t = 1.7$ ms, f) $t = 1.8$ ms, g) $t = 2.0$ ms, h) $t = 2.4$ ms, i) $t = 2.5$ ms	47
3.15	LG with different curvatures. a) straight LG, a) curved LG	48
3.16	Dependence of maximum displacement on the curvature parameter with the ball velocity 3 m/s	50
3.17	Dependence of first principal stress on the curvature parameter with the ball velocity 3 m/s	51
3.18	Equivalent strain in PVB interlayer with the ball velocity 3 m/s. a) $c = 0$ mm, b) $c = 38$ mm, c) $c = 76$ mm, d) $c = 152.5$ mm	51
3.19	LG with different curvatures. a) straight LG, b) curved LG	52
3.20	Laminated glass mode frequency	53
3.21	LG with different curvatures. a) straight LG, b) curved LG	55
3.22	LG boundary conditions	55
3.23	Magnitude of the displacement vector in LG with the ball velocity 8 m/s. a) $c = 0$ mm, b) $c = 31$ mm, c) $c = 94$ mm, d) $c = 250$ mm	56

3.24	Dependence of maximum displacements in LG on the curvature parameter	57
3.25	FE mesh of the model	58
3.26	Dependence of u_{max} of ball bottom and plate top center node on time	59
3.27	Dependence of σ_1 of plate bottom center node on time	59
3.28	Dependence of u_{max} of plate bottom center node on Young's modulus of interlayer	59
3.29	Dependence of first and second peak of σ_1 of plate bottom center node on Young's modulus of interlayer	59
3.30	Maximum displacement at the bottom central point of the plate vs time for different values of Young's modulus of the interlayer	62
3.31	First principal stress at the bottom central point of the plate vs time for different values of Young's modulus of the interlayer	62
3.32	Maximum displacement at the bottom central point of the plate vs time for different interlayer thickness values	62
3.33	First principal stress at the bottom central point of the plate vs time for different interlayer thickness values	62
3.34	Dependence of u_{max} of plate bottom center node on the thickness of interlayer .	63
3.35	Dependence of first and second peak of σ_1 of plate bottom center node on the thickness of interlayer	63
3.36	Dependence of u_{max} of ball bottom and plate top center node on time	64
3.37	Dependence of F of plate top center node on time	64
4.1	Peridynamic model	65
4.2	Geometry of circular plate and loading for the ring bending test	67
4.3	Comparison of solutions of displacements via radial coordinate	67
4.4	Dependence of bottom middle node displacement on time with $\delta = 1.36$ mm and different number of nodes	69
4.5	Dependence of bottom middle node displacement on time with $\delta = 1.55$ mm and different number of nodes	69
4.6	Dependence of bottom middle node displacement on time with $\delta = 1.81$ mm and different number of nodes	70
4.7	Discretisation of the simulation model. a) FEM mesh, b) PD lattice	72
4.8	Distribution of displacement over the bottom side. a) FEM solution, b) PD solution	72
5.1	Damage distribution on the bottom side of a plate. a) $t = 51.7253$ s, b) $t = 51.7253$ s + 0.5 ms, c) $t = 51.7253$ s + 4.4 ms	76
5.2	Damage distribution on the bottom side of a plate with different critical stretch value. a) $s_c = 1.0 \cdot 10^{-3}$ at $t = 25.5$ s, b) $s_c = 0.75 \cdot 10^{-3}$ at $t = 19.1$ s, c) $s_c = 0.5 \cdot 10^{-3}$ at $t = 12.7$ s	77
5.3	Damage distribution on the bottom side of a plate with $s_c = 1.5 \cdot 10^{-3}$ at the surface nodes of bottom layer. a) $t = 38.601$ s, b) $t = 38.601$ s + 1.6 ms, c) $t = 38.601$ s + 10 ms	78
5.4	Damage distribution on the bottom side of a plate with $s_c = 1.0 \cdot 10^{-3}$ at the surface nodes of bottom layer. a) $t = 35.12$ s, b) $t = 35.12$ s + 7.9 ms, c) $t = 35.12$ s + 9.6 ms	79
5.5	Damage distribution on the bottom side of a plate with $s_c = 0.75 \cdot 10^{-3}$ at the surface nodes of bottom layer. a) $t = 27.2$ s, b) $t = 34.0074$ s, c) $t = 34.0109$ s .	80
5.6	Damage distribution on the bottom side of a plate with $s_c = 0.5 \cdot 10^{-3}$ at the surface nodes of bottom layer. a) $t = 19.8$ s, b) $t = 33.001$ s, c) $t = 33.0082$ s .	80
5.7	Peridynamic impact model	82

5.8	Damage distribution on the bottom side of a plate with different initial velocities of the ball. a) $v = 6$ m/s at $t = 0.668$ ms, b) $v = 9$ m/s at $t = 0.476$ ms, c) $v = 12$ m/s at $t = 0.073$ ms, d) $v = 15$ m/s at $t = 0.034$ ms, e) $v = 30$ m/s at $t = 0.004$ ms	83
5.9	Damage distribution on the bottom side of a plate with $v = 6$ m/s and $s_c = 1.0 \cdot 10^{-3}$ at the surface nodes of bottom layer. a) $t = 0.009$ ms, b) $t = 0.156$ ms, c) $t = 1.153$ ms	84
5.10	Damage distribution on the bottom side of a plate with $v = 9$ m/s and $s_c = 1.0 \cdot 10^{-3}$ at the surface nodes of bottom layer. a) $t = 0.005$ ms, b) $t = 0.142$ ms, c) $t = 0.389$ ms	85
5.11	Damage distribution on the bottom side of a plate with different initial velocities of the ball. a) $v = 12$ m/s at $t = 0.004$ ms, b) $v = 15$ m/s at $t = 0.004$ ms, c) $v = 30$ m/s at $t = 0.002$ ms	85
5.12	Damage distribution on the bottom side of a plate with $v = 6$ m/s and $s_c = 0.5 \cdot 10^{-3}$ at the surface nodes of bottom layer. a) $t = 0.009$ ms, b) $t = 0.1$ ms, c) $t = 2.3$ ms	86
5.13	Damage distribution on the bottom side of a plate with $v = 9$ m/s and $s_c = 0.5 \cdot 10^{-3}$ at the surface nodes of bottom layer. a) $t = 0.005$ ms, b) $t = 0.009$ ms	86
5.14	Dependence of critical time on the initial velocity if the ball with different s_c values	87
5.15	Damage distribution on the bottom side of a plate with $v = 3$ m/s and different critical stretch values. a) $s_c = 2.0 \cdot 10^{-3}$ at $t = 3.5$ ms, b) $s_c = 1.0 \cdot 10^{-3}$ for the surface nodes of the bottom layer at $t = 1.0$ ms, c) $s_c = 0.5 \cdot 10^{-3}$ for the surface nodes of the bottom layer at $t = 3.4$ ms	88
5.16	Modeling of initial defects with Peridynamics. a) 1 node, b) 2 nodes	89
5.17	Damage distribution on the bottom side of a plate with 1 defect node under the load ring. a) $t = 51.9504$ s, b) $t = 51.9504$ s + 0.1 ms, c) $t = 51.9504$ s + 0.7 ms	90
5.18	Damage distribution on the bottom side of a plate with 2 defect nodes under the load ring. a) $t = 51.0916$ s, b) $t = 51.0916$ s + 0.3 ms, c) $t = 51.0916$ s + 1.5 ms	91
5.19	Damage distribution on the bottom side of a plate with 4 defect nodes under the load ring. a) $t = 48.0097$ s, b) $t = 48.0097$ s + 0.3 ms, c) $t = 48.0097$ s + 1.2 ms	91
5.20	Dependence of critical time/force on the number of nodes with attached low critical stretch bonds	92
5.21	Damage distribution on the bottom side of a plate with 1 defect node under the load ring with $s_c = 0.75 \cdot 10^{-3}$ at the surface nodes of bottom layer. a) $t = 34.0$ s, b) $t = 34.0$ s + 7.7 ms, c) $t = 34.0$ s + 8.1 ms	94
5.22	Damage distribution on the bottom side of a plate with 4 defect nodes under the load ring with $s_c = 0.75 \cdot 10^{-3}$ at the surface nodes of bottom layer. a) $t = 27.2$ s, b) $t = 34.0$ s + 7.6 ms, c) $t = 34.0$ s + 8.5 ms	95
5.23	Loading configuration, strain and stress states in a plate under ring bending. a) Top view, b) bottom view, c) region inside load ring radius, d) semi-circular surface flaw in under equibiaxial stress	96
5.24	Damage distribution on the bottom side of a plate without initial imperfections (case 1). a) $t = 51.9806$ s, b) $t = 51.9809$ s, c) $t = 51.982$ s, d) $t = 51.9826$ s, e) $t = 51.9832$ s, f) $t = 51.9856$ s, comparison with experimental damage pattern presented in [53]	100
5.25	Damage distribution on the bottom side of a plate with an initial imperfection on the load ring radius at the bottom side (case 2). a) $t = 51.9606$ s, b) $t = 51.9609$ s, c) $t = 51.9612$ s, d) $t = 51.9615$ s, e) $t = 51.9618$ s, f) $t = 51.9653$ s, comparison with experimental damage pattern presented in [53]	101

5.26	Damage distribution on the bottom side of a plate with an initial imperfection outside the load ring radius at the bottom side (case 3). a) $t = 51.9505$ s, b) $t = 51.9507$ s, c) $t = 51.9509$ s, d) $t = 51.9513$ s, e) $t = 51.9523$ s, f) $t = 51.9653$ s, comparison with experimental damage pattern presented in [53]	102
5.27	Comparison of time and force to reach final damage states for a plate without initial imperfections (case 1), with initial imperfection on the load ring radius (case 2), and with initial imperfection outside the load ring radius (case 3). a) time to final damage state, b) force required to reach final the damage state	102
5.28	Damage distribution on the bottom side of a plate with a softer skin layer ($s_c = 7.5 \cdot 10^{-4}$) at the bottom side. a) $t = 27.2$ s, b) $t = 34.0006$ s, c) $t = 34.0076$ s, d) $t = 34.0103$ s, e) $t = 34.0104$ s, f) $t = 34.0109$ s, comparison with experimental damage pattern presented in [53]	103
5.29	The lattice of random distribution of defects with $s_c = 1.0 \cdot 10^{-4}$ on the bottom side of a plate with $s_c = 1.5 \cdot 10^{-3}$ at the surface nodes of bottom layer. a) first case, b) second case, c) third case	104
5.30	Damage distribution of random defects with $s_c = 1.0 \cdot 10^{-4}$ on the bottom side of a plate with $s_c = 1.5 \cdot 10^{-3}$ at the surface nodes of bottom layer. a) first case $t = 34.51$ s, b) second case $t = 36.01$ s, c) third case $t = 37.01$ s	105

Tables

1.1	Mechanical properties	4
1.2	Strength parameters, after [53]	6
3.1	The results of frequencies calculations	36
3.2	Material properties	40
3.3	Dependence of the results on model mesh size and ball velocity	42
3.4	Dependence of the results at a speed of 6 m/s on the model mesh size	43
3.5	Dependence of the results on interlayer size and ball velocity	45
3.6	Dependence of the results on interlayer size and ball velocity	49
3.7	Regression parameters	50
3.8	Dependence of laminated glass mode frequency on curvature	53
3.9	Calculation results	56
3.10	Displacement, first principal stress, and first principal strain at different time points	60
5.1	The results of s_c and model lattice influence on the damage.	81

Nomenclature

Symbols

a	plate length	r_{sr}	radius of the support ring
a_{crack}	radius of semi-circular crack	R	radius of the plate
a_{min}	minimum flaw size	R_0	rate of exponential function
a_{max}	maximum flaw size	R^*	effective curvature radius
A_0	offset of cubic polynomial function	s	bond stretch
A_1	coefficient of cubic polynomial function	S	surface
A_2	coefficient of cubic polynomial function	S_0	initial value of exponential function
A_3	coefficient of cubic polynomial function	s_c	critical bond stretch
b	plate width	t	time
c	curvature parameter	T	kinetic energy
D	bending stiffness	t_m	time at maximum force value
E	Young's modulus	t_1	time of maximum value of
E^*	effective elastic modulus		LG displacement
f	line force	t_2	time of maximum stress/strain
f_s	surface load		experienced over the entire impact
F	concentrated contact force	u_{max}	maximum value of displacement
F_c	critical force	V	volume
F_{max}	maximum value of contact force	v_b	ball velocity
F_p	cumulative failure probability	W	work of external forces
F_{res}	resultant force	x	geometrical coordinate
G	shear modulus	y	geometrical coordinate
G_c	Griffith critical energy release rate	y_0	offset of exponential function
h	plate thickness	z	geometrical coordinate
h_{int}	interlayer thicknesses	δ	horizon
H	normal mode	δ_{kl}	Kronecker symbol
H_x	finite size spherical neighborhood	Δt	small time increments
K	bulk modulus	ε_0	strain state at the tensile surface
K	fracture toughness	ε_1	first principal strain
K_I	stress intensity factor	ε_{eq}	equivalent strain
L	Lagrange function of action	ε_r	radial strain component
m	weighted volume	ε_φ	circumferential strain component
m_b	ball mass	ζ_j	penalties
m_w	Weibull modulus	η	acceptable error
M_r	radial bending moment	θ	nonlocal dilatation
M_φ	circumferential bending moment	λ_i	Lagrange multipliers
p_1	eigenfrequency	μ	stretch condition
P	potential energy	ν	Poisson's ratio
q_{nk}	natural frequencies of plate vibrations	ρ	material mass density
r_{lr}	radius of the load ring	σ_1	first principal stress

Nomenclature

σ_W	Weibull characteristic fracture strength	\mathbf{f}_c	contact force vector
$\sigma_{\theta W}$	Weibull characteristic fracture strength	\mathbf{I}	second-rank unit tensor
σ_{I_l}	lower bounds of fracture stress	\mathbf{K}	stiffness matrix
σ_{I_u}	upper bounds of fracture stress	\mathbf{M}	mass matrix
τ	impact time	\mathbf{n}	unit normal to the plate face
ϕ	constant phase	\mathbf{p}	external force vector
φ	damage variable	\mathbf{q}	system configuration generalized coordinates
ω	eigenfrequency	\mathbf{s}	normal mode vector
\mathbf{A}	matrix of indexes	\mathbf{T}	peridynamic force density state
\mathbf{b}	peridynamic external force density	\mathbf{u}	vector of displacement
\mathbf{B}	matrix of derivatives over shape functions	\mathbf{x}	material point
\mathbf{D}	matrix of derivatives	\mathbf{x}'	material point
\mathbf{e}^d	deviatoric part of extension	\mathbf{Y}	peridynamic deformation state
\mathbf{E}	matrix of material elastic characteristics	ε	strain tensor
\mathbf{f}	external load vector	$\boldsymbol{\sigma}$	Cauchy stress tensor
		ξ	bond
		ω	influence function

Abbreviations

CCM	classical continuum mechanics
FEM	finite element method
FN	frequency number
LG	laminated glass
LPS	linear peridynamic solid
PD	peridynamics
PVB	polyvinyl butyral

1 Introduction

1.1 General information

The application of glass has experienced a significant rise in recent times and found widespread use across various industries, including architecture [16, 25, 41], structural engineering [14, 58, 99], automotive manufacturing (especially for windshields) [1, 3, 13, 49, 53], safety and security measures in vulnerable buildings [77, 100], defense applications [72], railway transportation [50], aerospace [62, 86], and even as encapsulant materials for solar cell modules [51, 60, 69], among other uses. Their versatility stems from their ability to be customized and tailored to meet specific requirements [31, 66, 86]. Glass structures encompass elements that not only support a portion of the loads but also serve a functional role [40, 50].

Figure 1.1 illustrates examples of glass plates used in the automotive industry as automobile windshields with various types of damage.



Figure 1.1: Examples of damaged glass components

Structural glass refers to components that bear their weight and applied live loads, typically over considerable spans [24, 31, 40, 89]. This material is amorphous, with a random atomic structure [76]. It is characterized by its complexity, good electrical and thermal insulation, brittleness, primary transparency, chemical inertness, lack of a precise melting point, high compressive

strength, and isotropy. Amorphous solids include metallic alloys, ionic melts, aqueous solutions, molecular liquids, and polymers like acrylic sheets, polycarbonate, and polyethylene terephthalate [92]. The most common type is soda-lime-silica glass, composed of sand (containing silica), soda ash, limestone, and small quantities of additives [19, 85]. Annealed variants, the primary product of the float process, are produced by heating the constituents until they fuse, followed by controlled cooling to relieve internal stresses. However, annealed ones tend to fracture into large, jagged shards, making them unsuitable for many applications. These base materials are often processed further to create advanced products such as toughened, laminated, or coated varieties [92]. For example, tempered or toughened glass is produced through controlled chemical or thermal treatments, enhancing its strength and altering its fracture pattern; surface coatings are added to improve transmission, absorption properties, and resistance to scratches or corrosion. Heat treatments introduce surface compression, producing materials with intermediate strength between tempered and annealed varieties [64].

In addition to the technological modifications of monolithic plates, a lamination process is widely employed, resulting in laminated glass (LG) [4, 78]. These structures consist of two or more layers of material separated by a thin polymer interlayer (Figure 1.2).

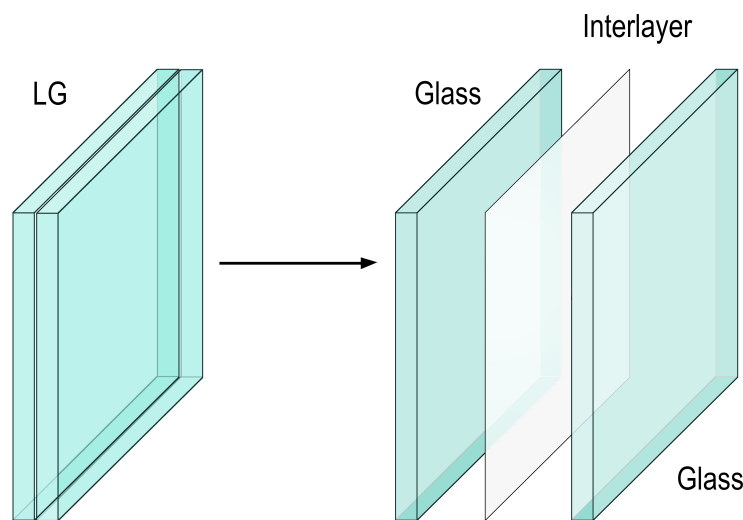


Figure 1.2: Laminated glass (LG)

LG demonstrates enhanced resistance to forces that lead to cracking. Moreover, the lamination process reduces the risk of dangerous consequences after fracture, as the interlayer holds the broken fragments together and prevents dangerous shard formation. The composite can support its weight even in a fractured state, as only one of the layers fails. This ensures significant residual strength after breakage [13, 58, 73].

An internal layer of LG influenced by various aspects, such as stiffness, impact strength, fracture pattern, and load-bearing capacity, is well-established. Typically, polyvinyl butyral films (PVB) and Cross-Linked Ethylene Vinyl Acetate (EVA) are the most commonly used interlayer materials. However, in addition to PVB and EVA, Ionoplast Polymers, Cast in Place (CIP) liquid resin, and Thermoplastic polyurethane (TPU) are also used as interlayers [91, 92].

LG is engineered to ensure the interlayer holds broken fragments together in the event of a fracture. It absorbs impact energy and enhances the fracture behavior compared to monolithic plates, making it a preferred choice in applications where injury risks from breakage are a con-

cern. Given its diverse applications across industries, specific interlayers are chosen to meet the unique requirements of each use case [92].

Studies reported in [78, 79] demonstrated that most LG has been composed of glass components ranging from 2 mm to 25 mm thick, with polymer interlayers typically falling between 0.38 mm and 2.5 mm thick. This results in a glass-to-polymer thickness ratio of around 3 to 10. Laminates comprising thin glass and thick ionoplast interlayers exhibit strengths comparable to 3 mm to 5 mm monolithic glass. Since modern laminates are predominantly polymer-based, these thin glass ionomer laminates offer substantial strength-to-weight ratio advantages over monolithic or conventionally structured LG. Given the unconventional glass-to-polymer thickness ratio in these high-performance laminates, it becomes necessary to investigate the structural behavior of such laminates and develop a rational design approach to achieve optimal laminate structures.

Results presented in [58] have described PVB as the most commonly used interlayer material. It is a highly flexible hyper-elastic material that can withstand significant strains before failure without undergoing substantial permanent deformation. Additionally, PVB is nearly incompressible, further contributing to its suitability for LG applications. One of the distinctive characteristics of PVB is its nonlinear behavior, which varies depending on the loading rate and temperature. At high strain rates, the stress-strain history displays an initial rapid increase in stress, followed by an abrupt decrease. However, this initial rise in stress is not observed at low strain rates. These properties make PVB a valuable choice for applications where impact resistance and safety are critical factors.

PVB is an amorphous thermoplastic material that demonstrates linear-viscoelastic behavior [1, 12, 47, 71]. A critical characteristic of viscoelastic materials is their mechanical properties vary with frequency (or time) and temperature. Since the tensile modulus of PVB is significantly lower than glass's, it results in substantial transverse shear within the viscoelastic layer. As a consequence, LG does not behave elastically, and the sections of the material do not conform to the assumptions of Euler-Bernoulli beam theory, where plane sections remain plane [1]. Due to the effects of shear strain, this non-elastic behavior makes the structural analysis of LG elements more complex [17].

Most of the studies in the literature have focused on flat glass panels. Nevertheless, there is significance in studying initially curved ones due to their potential to demonstrate enhanced functional and operational attributes such as improved aerodynamics and higher load capacity. It's important to maintain that curved LG exhibits distinct differences from straight LG, particularly in its static and dynamic behavior [4]. Curved plates have not been widely utilized in practical applications due to a lack of comprehensive knowledge about their structural behavior [22]. The distinctive feature of a curved LG compared to a straight one lies in its initial curvature, which significantly affects its behavior. The majority of the research has focused on the linear behavior of curved plates, mainly due to the mathematical complexities associated with analyzing nonlinear behavior. However, understanding nonlinear behavior is essential to assess real-world performance accurately. LG used in curved plates is prone to experiencing large deflections in the transverse direction when subjected to lateral loads. The glass layers' thicknesses are relatively small compared to other dimensions, making them more sensitive to deformation. Developing a mathematical model based on large deflection theory is necessary to predict the strength and behavior of curved LG plates. Such a model would be considered for the nonlinearity and complexities involved, allowing for a more accurate understanding of the structural response of curved plates under various loading conditions. This development could lead to broader applications of curved LG in the future [4].

It has become increasingly popular in modern architecture, particularly for creating free-form

roofs and facades that offer unique and visually striking design opportunities. Traditionally, the fabrication of curved LG relies on hot-forming techniques. One common method is sag bending, in which flat glass plates are placed on a negatively curved mold and heated until the material becomes pliable. Gravity ensures uniform contact with the mold; as the material cools, it retains the desired shape. Another approach is press bending, where stainless steel mold surfaces and pressing heads shape the glass into the required curvature. Once cooled and solidified, the resulting panels exhibit complementary curvatures. Polymeric interlayers are inserted between the curved glass sheets to produce the final laminated assembly, and the entire stack undergoes lamination in an autoclave. Press bending supports the creation of single- and double-curvature panels, although this technique requires a dedicated mold for each shape. As a result, producing larger quantities of identical panels is more cost-effective, while crafting molds for unique designs can be both time-intensive and expensive. Despite these challenges, curved LG remains highly valued in contemporary architecture for its versatility and ability to generate striking and distinct architectural designs [25].

Computer-aided modeling and design advancements have significantly contributed to integrating freely shaped geometries in architectural design processes. Curved glass has become a key feature among these innovations, particularly in facades. A notable example of its application is in the automotive industry, where it has been used for windshields with a curvature radius as small as 1.5 m. Despite its growing use, a standardized method for assessing the strength of curved glass is still lacking, presenting a critical challenge. Continued research and development efforts are imperative. These efforts would enable the creation of reliable testing protocols for accurately evaluating strength across various applications, including architectural and automotive uses [48, 49].

1.2 Mechanical behavior of glasses and glass structures

Glass is typically characterized as a linear-elastic material in mechanical modeling [21]. Its mechanical properties can exhibit high variability depending on chemical composition, technological, manufacturing, and handling processes and intended applications. However, several key data frames are commonly associated with most types of glass (Table 1.1) [13, 41, 50, 73, 76, 97, 98, 99, 100].

Table 1.1: Mechanical properties

Mohs Hardness	5.5 – 7
Brittleness	low tensile strength but high compressive strength
Young's Modulus (GPa)	50 – 90
Tensile Strength (MPa)	30 – 300
Compressive Strength (MPa)	500 – 1500
Density (kg/m ³)	2400 – 2800
Poisson's ratio	0.17 – 0.30

Due to the technological process, glass plates exhibit significant variations in fracture strength. This variability is influenced mainly by differences in the glass surface created during production. A prime example of such a process is the production of float glass. This leads to distinct characteristics on the two surfaces of the glass: one side, known as the "tin side," comes into direct

contact with the tin, while the other side, known as the "air side," is exposed to the air. Tin can penetrate the glass through an ion-exchange process with silicon, and the depth of tin diffusion on the tin side can range from 10 μm to 50 μm . As a result of these surface differences, the two sides of the float glass exhibit distinct mechanical behaviors, particularly in terms of strength characteristics [53].

The strength of materials such as glass is often analyzed using statistical models, one of which is the Weibull distribution [93]. This model is beneficial for estimating the strength of glass because it accounts for the probabilistic nature of material failure. In the context of the "weakest-link-in-the-chain" concept, which assumes that failure initiates at the weakest point in the material, Weibull statistics can be applied to estimate the strength of glass based on the critical force value [53]. The Weibull distribution allows us to model the variability in strength characteristics and predict the probability of material failure under different loads. The two-parameter Weibull distribution is formulated as follows [93]

$$F_p(\sigma_W) = 1 - \exp \left[- \left(\frac{\sigma_W}{\sigma_{\theta W}} \right)^{m_w} \right], \quad (1.1)$$

where F_p is the cumulative failure probability for the material subjected to stress σ_W , $\sigma_{\theta W}$ is the Weibull characteristic fracture strength and m_w is the Weibull modulus, its value indicates the degree of strength variation: the larger the value of m_w , the smaller the scatter.

From [53], it is known that the air side generally shows higher strength values than the tin side. The determined strength parameters are presented in Table 1.2. The contrast between the air and tin sides highlights the importance of considering surface-specific characteristics when evaluating glass strength [6]. According to [53], for the tin side, the experimental data are in good agreement with the Weibull distribution. The fracture strength of the tin side is relatively predictable and can be modeled reliably using Weibull statistics. In contrast, the air side exhibits noticeably higher fracture stresses compared to the tin side, suggesting that it has the potential to withstand greater loads before failure. However, the raw, unfiltered data from the air side show significant scatter, which makes it challenging to apply the Weibull distribution directly. The air side exhibits high fracture strength, as the increased characteristic strength shows. This characteristic strength is a critical parameter, representing the stress level at which there is a 63.2% probability of failure. Additionally, the 5% quantile, another critical metric, captures the lower bound of the strength distribution, indicating the stress level at which 5% of the samples are expected to fail. On the air side, the combination of high scatter and increased characteristic strength results in these two values being relatively close to each other. This suggests that while the air side can achieve high strength in some instances, its overall strength distribution is broad and inconsistent. Particularly for the air side of the glass, the large scatter in the experimental data is reflected in a low Weibull modulus. m_w is a key parameter that quantifies the variability in the material's strength: a lower modulus indicates a broader distribution of strength values, suggesting greater unpredictability and the presence of more significant flaws or microstructural inconsistencies on the air side. This large scatter suggests that the fracture strength of the air side can vary considerably, likely due to the presence of micro-defects or surface irregularities that developed during the manufacturing process [57].

Studies reported in [58] describe that the mechanical properties of float glass are primarily characterized by brittle fracture behavior, which exhibits probabilistic fracture strength. This strength is influenced by various factors, including the geometry of the glass plate, the loading conditions

Table 1.2: Strength parameters, after [53]

	Characteristic fracture, (MPa)	Weibull modulus [-]	Strength, 5% quantile, (MPa)
Tin side	191.7(185.0 ... 198.7)	8.27(6.57 ... 10.4)	133.9
Air side	221.9(210.7 ... 233.8)	8.41(5.97 ... 11.8)	155.9

it experiences, and the boundary conditions applied to it. The presence of microscopic surface flaws plays a significant role in determining the probabilistic fracture strength of glass. These flaws are where fractures typically initiate when stress is applied to the glass. Glass plates tend to fail primarily in tension. Consequently, the tensile strength of glass is typically much lower than its compressive strength. It's worth noting that if these microscopic surface flaws are removed or reduced, such as through processes like chemical etching of the glass surface, the fracture strength of the glass can be significantly increased. This reduction in flaws can make the glass more resistant to fracture. Another important aspect to consider is the loading rate. The fracture strength of glass is rate-dependent, meaning it can vary with the speed at which the load is applied. This rate dependency has been demonstrated in various studies and applies to loading in both tension and compression. In essence, the fracture behavior of glass can be influenced by its inherent flaws and characteristics and by the rate at which external forces are applied [75].

The strength of glass is primarily influenced by surface flaws that typically range in size from 10 μm to 300 μm (Figure 1.3), which arise during the manufacturing process. Tin can penetrate the glass through an ion-exchange process with silicon, and the depth of tin diffusion on the tin side can range from 10 μm to 50 μm [70, 94]. On the tin side, flaws generally form around tin-oxide particles adhering to the surface. In addition, both the tin and air sides can develop flaws due to thermal gradients during the float glass production process. On average, the flaws on the air side are 1.5 to 2.0 times smaller than those on the tin side. These variations in flaw distribution result in differing strength characteristics between the two sides. Flexural strength values of the air side typically being up to twice that of the tin side [53].

Micro-cracks in brittle materials due to high-stress concentrations can significantly influence crack propagation. These micro-cracks, located around the tip of a macro-crack, can shield or amplify the main crack, leading to variations in stress intensity factors. Recent studies [10, 70] have shown that these micro-cracks and the associated shielding effect can enhance material toughness, a phenomenon known as "micro-crack toughening". These micro-cracks' specific location, orientation, and density are important in altering toughening mechanisms and main crack propagation. While analytical solutions for uniformly distributed micro-cracks have been presented, studying the impact of non-uniformly arranged micro-cracks analytically is challenging due to the materials' complex mechanical behavior. Some researchers have explored the effect of micro-cracks on main crack propagation, deriving solutions through analytical approximations under certain restrictive assumptions [7, 63].

While understanding the mechanical behavior of monolithic glass is essential, real-world applications often rely on more complex glass systems, such as LG, which introduces additional layers of complexity and performance considerations. The brittle nature of single-layer glass presents unique challenges, particularly in fracture behavior; however, when it is laminated with interlayers, its structural performance under impact and load can be significantly enhanced.

The structural behavior of an LG plate lies between two extreme cases in terms of stiffness:

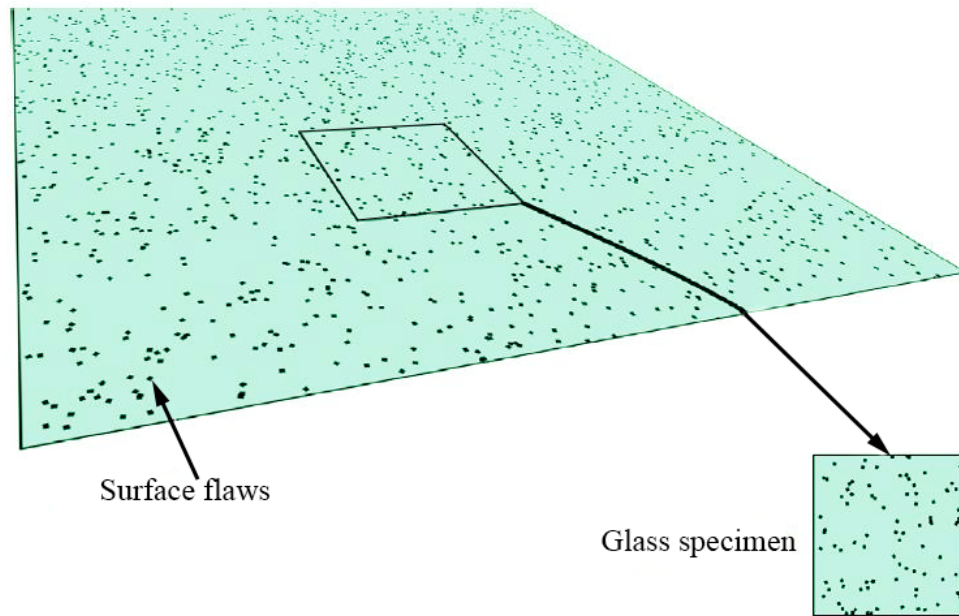


Figure 1.3: Surface flaw distribution, after [70]

the layered limit (lower bound) and the monolithic limit (upper bound) [24, 66]. The degree of composite action the interlayer provides influences the actual behavior, which can deviate from the layered limit and approach the monolithic limit. The significant difference between these limits necessitates considering the exact behavior when designing and assessing LG plates rather than relying solely on the limiting behaviors. The layered limit might be overly conservative, while the monolithic limit could pose significant safety risks. Therefore, an appropriate model that accounts for the genuine composite action is required for LG plate design and assessment [1, 13, 24, 51, 58, 73].

Damage probability models have been developed, utilizing the Weibull distribution to represent failures as well as for monolithic glasses. These models have been refined by comparing predictions and actual measurements [11].

The prediction of the elastic constants of homogenized multiphase materials has been a subject of active research for several decades. Researchers seek to establish upper and lower bounds for the overall stiffness of these materials. Variational theorems for strain and complementary energy are often used in this context. An approach based on Hashin's method for cross-ply laminates with interlaminar cracks is applied for cracked LG. This method involves assessing stress perturbations in the interlayer due to the presence of cracks. A set of equilibrated stress fields is constructed, and the principle of minimum complementary energy is employed to determine an optimal approximation within this set. This approximation provides a reasonable estimate of the effective stiffness of the composite material. In the context of LG, where Young's modulus of glass is significantly higher than that of the polymer interlayer, the cracked laminate is viewed as a combination of a polymeric layer and rigid glass fragments that act as stiffening elements. These glass fragments are assumed to be detached from the interlayer at their ends for a specific length [26].

Based on the existing discussion, there are some important approaches to modeling the strength of LG. However, many questions remain unanswered, highlighting the need for further investigation. A comprehensive understanding of the cracking processes and the formation characteristics

of the laminate structure is fundamentally tied to the behavior of the monolithic glass components [4]. This underscores the importance of in-depth studies into the processes of fracture and cracking in monolithic glass, as they play a pivotal role in determining the overall strength and processes of damage and cracking of monolithic glasses.

1.3 Modeling approaches

Various methods are used to predict and analyze the mechanical behavior of glass structures under different loading conditions [54]. The studies are carried out through analytical, numerical, and experimental analyses. Conducting direct experiments can be prohibitively expensive; experimental tests might cause random results influenced by unpredictable factors. As a cost-effective alternative, various innovative computational methods have been developed to address the complexities of fracture and fragmentation in LG [3]. Next, some fundamental approaches and considerations are described.

First-order shear deformation theory (FSDT) is commonly used to analyze sandwich and laminate structures [2]. It assumes that the normals to the mid-surface of a plate behave like rigid bodies during deformation, and forces and moments characterize mechanical interactions between cross-sections. FSDT allows for solving governing differential equations analytically, making it suitable for plates of various shapes. However, it may not accurately predict deformation properties for laminates with extreme differences in stiffness properties [51].

Zig-zag and layer-wise theories are alternative approaches to analyzing laminated structures [51, 74]. Zig-zag theory approximates displacements using piecewise functions through the thickness coordinate to ensure layer compatibility [23]. This reduces the three-dimensional elasticity equations to two-dimensional plate equations. Layer-wise theory, on the other hand, derives balance and constitutive equations for individual layers. It assumes that skin layers deform according to the Bernoulli–Euler beam theory, neglecting transverse shear deformations, while the soft core layer handles transverse shear stresses. Layer-wise theory can provide equations that are easier to solve in closed analytical forms than zig-zag theories and can explicitly analyze load transfer between layers. The layer-wise theory has been applied to LG plates, where the Kirchhoff plate theory describes layers' deformation while the core is modeled as the shear layer. This approach simplifies the analysis, focusing on membrane and bending states while ignoring transverse shear deformations [51].

The choice of analysis method depends on the laminated structure's specific characteristics and the accuracy level required. FSDT is suitable for more straightforward cases. Zig-zag and layer-wise theories offer alternatives that can balance accuracy and computational efficiency, and layer-wise theory, in particular, is found to be efficient for analyzing LG plates [53].

Due to the substantial computational demands of full-scale numerical analyses, simpler analytical methods are often employed to approximate the response of impacted plates and impactors. These methods, such as the energy-balance approach assuming quasi-static behavior or spring-mass models incorporating simplified dynamics, play a primary role in preliminary design stages. They enable swift assessments of contact force, contact duration, or the impactor and target's overall response. Spring-mass models featuring single- or multi-degree-of-freedom systems have been applied in various contexts, including composite laminates and sandwich structures. These models provide estimates of maximum force and impact duration and approximate the contact force by solving simplified equations of motion. Typically, the model comprises

several springs representing structural stiffness, nonlinear membrane stiffness, nonlinear contact stiffness, and two masses representing the structure's effective and the projectile's mass. The stiffness values for the springs are derived based on the plate's shape and boundary conditions, while the contact stiffness is determined using a contact law. For soft impacts, energy dissipation and damping must be considered in the energy balance of the models [31].

The core aspect of simulation lies in creating an appropriate contact interaction and deformation model between the target and the impactor. In simplified approaches, the Hertz contact law is commonly used to describe the contact problem. This classical law can be applied in finite element impact analyses where the impactor is indirectly approximated by a mass connected to the impacted plate. In commercial finite element software, the prevention of interpenetration between two bodies is primarily addressed using the penalty approach or the method of Lagrange multipliers. In the penalty-based contact method, penetration is countered by a force proportional to the penetration depth. While easy to implement, this method allows some interpenetration and can suffer from ill-conditioning, especially at high contact stiffness. Alternatively, the Lagrange multipliers approach treats contact forces as primary unknowns, enforcing the condition of impenetrability. Although this method increases computational cost due to additional unknowns, it prevents numerical errors related to ill-conditioning. Several improved methods have been proposed, such as the perturbed Lagrangian or augmented Lagrangian methods, based on these two techniques. When comparing contact pressures between a glass surface and a spherical impactor, classical Hertz theory's penetration depth and the contact area's radius, as calculated by the finite element method incorporating contact constraints for impenetrability, are the main parameters to consider [31].

Contact-impact problems are important in various engineering fields, particularly in glass structures, where much attention has been given to windshield glazings in the automobile industry [12]. When simulating the response of these structures, detailed numerical modeling of fracture patterns and LG elements has been a key focus. Several techniques have been employed, including continuum damage models, element deletion methods incorporating local or non-local failure criteria, the extended finite element method, and intrinsic cohesive zone models. In the case of monolithic glass, comparative studies have explored detailed models based on different numerical techniques such as the finite element method (FEM), extended finite element method (XFEM), discrete element method (DEM), and combined finite-discrete element method (FEM-DEM) [31].

FEM is used to analyze LG and photovoltaic panels accurately, a three-dimensional theory of elasticity can be applied, and numerical solutions can be obtained [74]. Commercial software provides various continuum shell finite elements and three-dimensional solid finite elements. Due to significant differences in material properties and the relatively low thickness of the core layer, careful meshing of the core layer is essential to accurately computing transverse shear strains and related stresses [23, 51]. FEM is widely employed for analyzing the impact fracture and fragmentation of LG. The explicit FEM has become a standard tool in crash simulations for addressing complex, non-linear, time-dependent issues such as head impacts on windscreens [3].

Challenges persist, including mesh distortion during large deformations and simulating crack propagation. These issues stem from FEM's dependency on mesh grid quality. To address these challenges, re-meshing schemes are proposed, albeit at a significant computational cost. In response, the meshfree particle method is introduced. This method's interpolation relies on a set of particles within a specific domain, offering flexibility in handling large deformations and fracture problems without the limitations of mesh grids. Its advantages have garnered attention

and found applications in various fields.

While the FEM can predict crack initiation and propagation in LG with reasonable accuracy, it struggles to simulate fragmentation and interactions between fragments due to its inherent continuity requirements [13]. Enhanced shape functions like XFEM don't fully address this issue. XFEM is a robust numerical technique for simulating crack propagation. It improves the traditional FEM by incorporating additional enrichment functions within the cracking region. This approach offers a notable advantage: cracks can be represented without requiring adjustments to the finite element meshes, eliminating the necessity for remeshing during crack growth modeling [12].

For analyzing the impact fracture and fragmentation of LG, the DEM is better suited to handle the inherent discontinuities. In this approach, an extrinsic cohesive fracture model is used to represent the brittle fracture of glass, while the interlayer is assumed to remain intact during the impact. However, when using spherical discrete elements to simulate post-damage behavior, the resulting crack patterns often lack precision, and some cracks are non-recognizable. DEM was initially developed to address non-continuum problems involving interactions between particles or blocks. The core concept of this method consists of dividing the computational domain into discrete elements (DEs) and characterizing the movements of these DEs using Newton's second law. Interactions between DEs are typically managed using contact algorithms. As cracking behaviors involve transitioning from a continuum to a discontinuum, similar to non-continuum problems, DEM has been extended to simulate cracking behaviors [12]. To capture these behaviors, apart from the contact model, a connection model is necessary to link discrete elements into a continuum before cracking occurs [13]. Generally, DEM performs well in simulating the fragments and fragmentation of LG under impact, but its accuracy in predicting crack initiation and fracture patterns is usually unsatisfactory [3].

Indeed, considering the occurrence of numerous cracks in LG during impact and utilizing inter-element separation in the FEM-DEM approach, it becomes a suitable method for modeling impact fracture and fragmentation in LG. FEM-DEM is supposed to tackle large-scale transient dynamics scenarios incorporating contact and fracture phenomena [13]. However, it is essential to highlight that the potential failures of the interlayer and interface are predefined. Still, whether these failure criteria are utilized in FEM-DEM simulations depends on the example's specifics.

The reality is that both material properties and failure mechanisms in composites are notably intricate and exhibit significant variations contingent upon manufacturing, processing, geometry, and testing conditions. These variations present various challenges when monitoring or simulating their failure. In a broad sense, applying mechanical and/or thermal loads induces the formation of microcracks within the matrix and gives rise to small-scale delaminations at the layered interfaces. As these loads are further intensified, these microcracks progress into mesoscale cracks, leading to fiber breakages and fostering delamination. Ultimately, this culminates in the development of macroscale cracks and fiber pullouts at the point of failure. This progression underscores that damage initiation and evolution in composite materials inherently occur at multiple scales and in a progressive manner. After initiation, there are several distinct degradation stages before final failure occurs [5].

In this context, various approaches have been developed to test, monitor, characterize, and simulate the failure process in composites. However, these approaches differ in several aspects, including the length scale they target, their precision and reliability in establishing a connection between local damage and global behavior, and their feasibility for use in real-world structures versus limited applicability to laboratory conditions [5].

The explicit FEM has become a well-established tool for highly nonlinear, time-dependent prob-

lems, such as simulating head impacts on windscreens in crash scenarios. In modeling component failure and crack propagation, the most commonly used approach is the element erosion technique. However, this method comes with certain disadvantages, including mass and energy conservation issues. One notable drawback of the element erosion technique is its inability to describe the fracture of glass resulting from crack propagation accurately. This limitation primarily arises from the high stress intensity at the crack tip, which is a characteristic of brittle materials and is predicted by linear elastic fracture mechanics (LEFM). Importantly, this stress intensity is not precisely represented by classical FEM and heavily relies on the size of the finite elements used. A substantial number of very small elements would be required to capture this stress intensity accurately. Conversely, a massive number of small elements could lead to the prediction of a singularity in the stress field near the crack tip. Nevertheless, element erosion remains an easy-to-implement technique and can be readily combined with conventional failure criteria like the maximum principal strain or stress criterion. Several alternative approaches, such as the DEM and the Cohesive Zone Modeling, demonstrate that accurately modeling the failure behavior of materials remains a significant challenge. Additionally, the XFEM poses complexities in its application. However, these alternative methods are not widely adopted in engineering practice due to intricate theories, lack of essential input parameters, or excessively high computational demands. Many of these modeling techniques are currently far from being practically applicable in industrial contexts [3].

When modeling failure in composites, there are primarily two approaches: fracture mechanics and damage mechanics [44]. The fracture mechanics approach aims to explicitly represent internal discontinuities like cracks while cracking equivalent effects such as stiffness and strength reduction are typically turned to using damage mechanics methods. Fracture mechanics approaches for composites have been applied through diverse numerical techniques. On the other hand, damage mechanics approaches commonly employ continuum-based failure criteria, which establish relationships between stresses and experimental data on material strength to predict failure initiation [5].

Traditional failure criteria alone are insufficient to capture the quasi-brittle failure of composite laminates comprehensively. This failure, arising from multiple mechanisms, necessitates a more nuanced approach. Continuum damage mechanics (CDM) methods have been developed to study the nonlinear response due to accumulating damage [20, 77, 86]. In CDM methods, damage accumulation is simulated by reducing specific material properties, leading to a loss of load capacity in particular directions. The macroscopic stress-strain behavior gradually changes due to a distributed network of microcracks. Initially applied in metals through a single scalar damage parameter representing microcrack density within a continuum medium, this concept suggests the existence of intermediate phases between intact material and final fracture. This approach has evolved to incorporate multiple damage variables associated with various failure mechanisms to model damage initiation and evolution in composites. A constitutive model for anisotropic damage was developed to describe the relationship between material damage and effective elastic properties for structure stress analysis. Internal variables were introduced to depict the evolution of the damage state under loading and subsequent material stiffness degradation. CDM treats damaged materials in this framework as continuous despite inherent heterogeneities, micro-cavities, and defects. The nonlinear response to loading conditions is predicted based on constitutive relations between macroscopic variables (such as stress and strain) and internal variables, representing irreversible changes occurring at the microscopic level [5].

Results presented in [13] showed a cohesive crack model utilized for glass. According to this model, a crack initiates when the bonding stress reaches the material's tensile strength, indicating

the onset of damage. Past this point, the bonding stress is assumed to decrease gradually as the crack width increases. When the crack width reaches a critical value, the bonding stress drops to zero, indicating that the crack is fully open [15].

The element deletion method (EDM) is called the erosion contact method [27, 28]. The fundamental concept behind this method involves removing elements from the global mass matrix or setting the stress of elements to zero to represent their failure. This approach has been incorporated into various commercial finite element solvers. In EDM, shell elements are typically employed to model glass, aiming to reduce the element count and consequently save computational resources. Glass is commonly assumed to be an elasto-plastic material in conjunction with a plastic strain fracture criterion within the EDM framework [12].

CDM postulates that the damage incurred by a material is reflected in its stress-strain response. This approach considers the material's degradation in mechanical properties due to damage, allowing for the modeling of progressive failure and structural integrity more comprehensively [5].

The existing literature lacks comprehensive solutions regarding the interaction of intricate micro-crack patterns [61]. An article [90] delves into the influence of small cracks on macro-crack propagation, establishing relationships between crack locations, density, numbers, and macro-crack speed. The study explores various models, including a single crack collinear with the main crack, two symmetrical cracks, and horizontal and transverse arrays of cracks. In a separate study, [7] explored diverse micro-crack patterns using bond-based models. It was discovered that the distribution of micro-cracks near the macro-crack tip resulted in significant shielding effects, substantially enhancing material toughness. Both studies involved two-dimensional plates with macro-cracks along their mid-axis, subjected to displacement-controlled tensile loads [36].

Silling and Askari [82] introduced the peridynamics (PD) method, a revolutionary approach to crack modeling, nucleation, and progression within a continuum, addressing the limitations of classical numerical methods. PD, established by Silling [80], represents a non-local form of continuum mechanics, differing significantly from the local differential form of classical continuum mechanics (CCM) [81]. In PD, a continuum body is defined by material points (particles) possessing a volume in space. These material points can interact with other points within a specified distance, known as the horizon. The interaction forces between a material point and others within the horizon dictate its behavior. PD, rooted in integro-differential equations rather than spatial derivatives, handles problems involving discontinuities such as cracks [18, 32, 42, 46, 59].

Unlike other methods, PD's governing equations are in integral form rather than spatial partial derivatives. Interactions between particles are determined by pairwise forces, known as PD forces. This model enables straightforward simulation of fractures by severing connection forces between particles. Due to its simplicity in fracture simulation, PD has been extensively studied and implemented in fracture mechanics [29, 30].

Silling presented a PD solution as part of the validation process, determining the crack propagation angle from the vertical axis using bond-based PD [45]. The article [68] introduced the dual horizon PD formulation to reduce calculation costs and explored this problem from this perspective. Investigating the effects of plate dimensions and model parameters, such as impact velocity and plate thickness, on crack propagation speed and crack angles, the study utilized the state-based PD model. However, the influence of micro-cracks on crack propagation in materials subjected to impact loads remains a gap in the literature that necessitates further investigation. The research [10] applied bond-based PD to explore the effect of micro-cracks on dynamic crack propagation, introducing a novel approach by defining two-dimensional micro-cracks and exam-

ining the impact of stochastically pre-located micro-cracks on a three-dimensional body using PD theory.

PD offers a distinct advantage over other computational methods like FEM and the boundary element method when it comes to simulating crack nucleation and extension. In FEM and boundary element methods, managing cracks typically involves complex and cumbersome remeshing procedures. However, in PD, the initiation and propagation of cracks result from the movement of material points, eliminating the need for remeshing. This characteristic makes PD an attractive choice for simulating failure and, more specifically, for modeling the interaction between a relatively large number of cracks [18, 55].

The diagram of generalized modeling approaches is given in Figure 1.4.

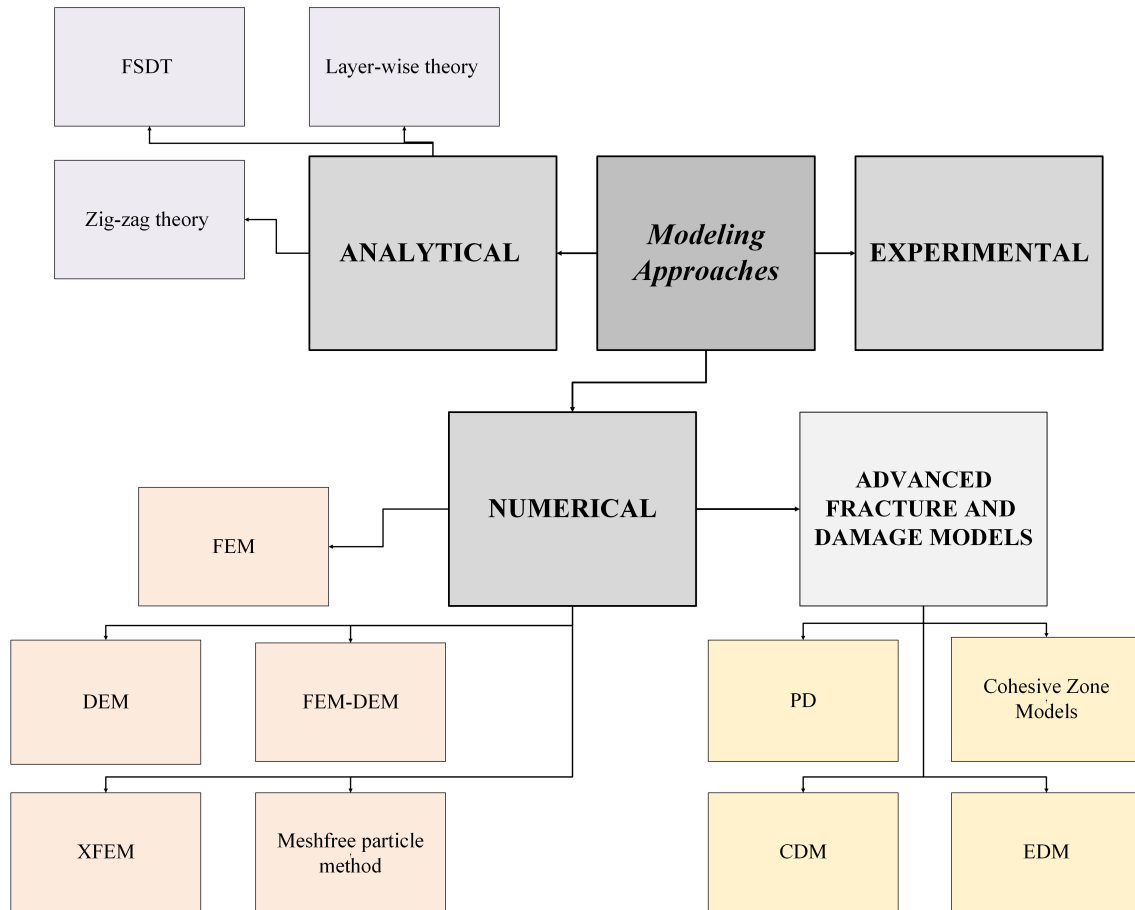


Figure 1.4: Modeling approaches

1.4 Problem statement and outline of the thesis

Considering what was described before, one could conclude that, despite extensive research on laminated and monolithic glass structures, several gaps limit a comprehensive understanding of their mechanical behavior and structural integrity in practical applications. Most studies have focused on straight LG panels, while curved LG panels exhibit distinct structural behavior and remain insufficiently studied. There is a significant gap in understanding the dynamic behavior of curved LG structures, particularly under impact loading.

Fracture behavior is the primary focus of studies on monolithic glasses nowadays. Many experimental and numerical works for modeling crack initiation have been conducted. Experimentally, it has been established that glass strength characteristics show significant value spread, which is explained as caused by technological factors, particularly imperfections such as defects. However, the initiation of crack patterns, flaw size, distribution, and depth influence the fracture force and crack propagation, which has been insufficiently studied. While statistical data on strength parameters and the possible distribution of defects across the surface exist, studies that connect these statistics are not much, and the existing ones do not consider the physical basis of the crack formation process.

Among the methods for studying glass strength, FEM and peridynamic theory are emphasized. Peridynamics has various justified advantages for studying damage and fracture, but few studies explore how the damage model parameter in peridynamic simulations influences the crack formation and strength determination. The impact of technological defects and the general variation in critical strength values observed experimentally has not been examined within the peridynamic framework. Statistical evaluations within the context of peridynamics have not been addressed in any works known to the author.

In conclusion, the gap in laminated and monolithic glass structure behavior investigation lies in the insufficient understanding of the dynamic behavior of curved LG panels, fracture behavior of glass structures, influence of micro-cracks, and technological flaws on fracture propagation. Advanced peridynamic modeling is needed to simulate these behaviors under dynamic impact conditions. This presents an opportunity to address these challenges through the project's general aim, which seeks to explore these phenomena comprehensively.

This work aims to investigate the behavior of laminated and monolithic glass structures comprehensively. It focuses on how material properties, geometric parameters, and technological imperfections (such as flaws) influence their performance to improve structural integrity in glass-based materials for practical applications. By employing both FEM and peridynamic modeling approaches, the research strives to develop and validate accurate models for simulating dynamic and quasi-static responses while exploring elastic response, initiation, and progression of damage, crack patterns, and the effects of flaws on fracture behavior.

The way to achieve this aim, there are specific goals that will be done within this research:

1. Study the elastic behavior of LG under impact loading.

This goal focuses on understanding how material properties and geometric parameters influence LG performance using FEM.

In particular, the following points must be addressed:

- Develop, test, and validate FEM models for LG structures to simulate dynamic behavior under impact.
- Investigate the influence of LG curvature parameters on the modal characteristics of LG.
- Analyze the influence of interlayer material properties and geometrical peculiarities on the dynamic behavior of LG under impact loading.

2. Study initial cracking and damage in monolithic glass plates under quasi-static loading.

This goal focuses on understanding damage formation and initial crack propagation in

monolithic glass plates, exploring how key damage parameter influences fracture behavior.

Tasks:

- Develop, test, and validate peridynamic models for the deformation of monolithic glass plates, ensuring accuracy through comparison with FEM.
 - Analyze the influence of node lattice type and density in peridynamic models on the accuracy of damage behavior.
 - Investigate the influence of the critical stretch parameter on the initiation and progression of damage and fractures in glass plates.
3. Study the dynamic cracking of glass structures under impact loading.
- This goal focuses on understanding the fracture response of glass plates under dynamic impact loading using peridynamic modeling and includes the following points:
- Perform dynamic impact simulations (e.g., ball drop tests) on glass plates to assess damage initiation, crack propagation, and fracture behavior.
 - Investigate the influence of the key damage parameter on the initiation and progression of fractures.
4. Study the influence of technological flaws (defects) on the behavior of glass plates under quasi-static loading.
- This goal focuses on understanding how the flaws (defects) characteristics influence the response of glass structures using peridynamic modeling.

Here the following tasks are addressed:

- Investigate the effect of size, density, and location of flaws on damage progression and crack patterns in glass plates during quasi-static simulations, comparing with experimental results from the literature.
- Analyze the influence of random distributions of flaws on the fracture force, damage, and crack patterns in glass plates under quasi-static loading.

2 Theoretical Background

2.1 Methodology of modeling

According to the problem statement, this research will investigate the static and dynamic behavior under impact loading of monolithic glass and LG panels and glass fracture. The solution strategy for modeling elastic and dynamic responses uses the FEM formulation [56, 67, 101, 102]. The challenges of cracking and fracture will be addressed through PD theory [45, 84].

FEM is utilized for its widespread applicability and efficiency in classical structural analysis. In contrast, PD is employed to overcome FEM's limitations in accurately simulating damage initiation and progression, providing a comprehensive approach to understanding glass behavior.

In this study, the materials are assumed to be linearly elastic, with viscosity effects neglected due to the nature of the scenarios analyzed. For static and impact loading, the low viscosity of glass justifies this simplification. In the case of LG, the interlayer is also considered non-viscous, as the focus is on the short initial reaction time of the plate under impact. This approach ensures that the modeling remains accurate while simplifying the analysis of dynamic and static responses.

2.2 Modeling in framework of finite element method

2.2.1 Structural analysis

A structural analysis evaluates the displacements, stresses, strains, and forces within structures or components under the influence of loads [56, 67, 101, 102]. Within the current research problem statement, an explicit dynamic analysis should be performed. The general statement for dynamic analysis formulation within the FE framework is based on the Hamilton-Ostrogradsky principle that is given through the Lagrange equation of the second kind in an assumption of conservativeness as follows

$$\frac{d}{dt} \left(\frac{\partial L}{\partial \dot{\mathbf{q}}} \right) + \frac{\partial L}{\partial \mathbf{q}} = 0, \quad (2.1)$$

where \mathbf{q} are the generalized coordinates that describe the configuration of the system, $\dot{\mathbf{q}}$ are the generalized velocities, L is the Lagrange function of action that presents the sum of kinetic energy T and potential energy P

$$L = T + P \quad (2.2)$$

Let's look through the theoretical formulation of the FE description of energies and how that provides the theoretical background for the FE modeling strategy [101] used in a current study.

Let \mathbf{u} be used for denoting the vector of displacement that has three components ($u_x(x, y, z, t)$, $u_y(x, y, z, t)$, $u_z(x, y, z, t)$) as a function of geometrical coordinates (x, y, z) and time (t)

$$\mathbf{u} = \{u_x \ u_y \ u_z\}^T, \quad (2.3)$$

where upper index T here and later means operation of matrix vector transpose.

When the kinetic energy of a structurally deformed and moved body could be presented as

$$T = \frac{1}{2} \int_V \dot{\mathbf{u}}^T \rho \dot{\mathbf{u}} dV, \quad (2.4)$$

where $\rho = \rho(x, y, z)$ is material mass density, V is volume of the body(ies) which is dynamically deformed. In the formula 2.4 and later the dot, upper the function, means the derivative by time, i.e. $(\dot{\cdot}) = \frac{d}{dt}(\cdot)$.

The structural elastic deformation leads to the formation of potential energy, which could be considered as a work of strains (relative deformations) on stresses

$$P = \frac{1}{2} \int_V \boldsymbol{\sigma}^T \boldsymbol{\varepsilon} dV, \quad (2.5)$$

where $\boldsymbol{\sigma}$ is a vector of stresses that describes Voigt notations of the Cauchy stress tensor representing 6 independent terms (3 normal stresses $\sigma_x(x, y, z, t)$, $\sigma_y(x, y, z, t)$, $\sigma_z(x, y, z, t)$ and 3 shear stresses $\tau_{xy}(x, y, z, t)$, $\tau_{yz}(x, y, z, t)$, $\tau_{xz}(x, y, z, t)$) and similar in Voigt notations the strain tensor $\boldsymbol{\varepsilon}$ is presented as 6 component vector (3 uniaxial strains $\varepsilon_x(x, y, z, t)$, $\varepsilon_y(x, y, z, t)$, $\varepsilon_z(x, y, z, t)$ and 3 shear strains $\gamma_{xy}(x, y, z, t)$, $\gamma_{yz}(x, y, z, t)$, $\gamma_{xz}(x, y, z, t)$)

$$\boldsymbol{\sigma} = \{\sigma_x \ \sigma_y \ \sigma_z \ \tau_{xy} \ \tau_{yz} \ \tau_{xz}\}^T, \quad (2.6)$$

$$\boldsymbol{\varepsilon} = \{\varepsilon_x \ \varepsilon_y \ \varepsilon_z \ \gamma_{xy} \ \gamma_{yz} \ \gamma_{xz}\}^T \quad (2.7)$$

The strain tensor represents the relative dimensionless deformation that stays within the concept of small displacements and small strains described by the Cauchy formulas

$$\begin{aligned} \varepsilon_x &= \frac{\partial u_x}{\partial x}, & \varepsilon_y &= \frac{\partial u_y}{\partial y}, & \varepsilon_z &= \frac{\partial u_z}{\partial z}, \\ \gamma_{xy} &= \frac{\partial u_x}{\partial y} + \frac{\partial u_y}{\partial x}, & \gamma_{yz} &= \frac{\partial u_y}{\partial z} + \frac{\partial u_z}{\partial y}, & \gamma_{zx} &= \frac{\partial u_x}{\partial z} + \frac{\partial u_z}{\partial x} \end{aligned} \quad (2.8)$$

One can represent the last in a matrix form

$$\boldsymbol{\varepsilon} = \mathbf{D}\mathbf{u}, \quad (2.9)$$

where \mathbf{D} is matrix of derivatives

$$\mathbf{D} = \begin{bmatrix} \frac{\partial}{\partial x} & 0 & 0 \\ 0 & \frac{\partial}{\partial y} & 0 \\ 0 & 0 & \frac{\partial}{\partial z} \\ \frac{\partial}{\partial y} & \frac{\partial}{\partial x} & 0 \\ 0 & \frac{\partial}{\partial z} & \frac{\partial}{\partial y} \\ \frac{\partial}{\partial z} & 0 & \frac{\partial}{\partial x} \end{bmatrix} \quad (2.10)$$

Then potential energy takes the form

$$P = \frac{1}{2} \int_V \boldsymbol{\sigma}^T \mathbf{D}\mathbf{u} dV \quad (2.11)$$

The stresses and strains have physical relations between them. In this work, the dynamic deformation of glasses is considered elastic up to the fracture and, with enough good accuracy, is subjected to Hooke's law in the isotropic statement

$$\boldsymbol{\sigma} = \mathbf{E}\boldsymbol{\varepsilon}, \quad (2.12)$$

where \mathbf{E} is the matrix of elastic characteristics of the material

$$\mathbf{E} = \frac{E}{(1+\nu)(1-2\nu)} \begin{bmatrix} 1-\nu & \nu & \nu & 0 & 0 & 0 \\ \nu & 1-\nu & \nu & 0 & 0 & 0 \\ \nu & \nu & 1-\nu & 0 & 0 & 0 \\ 0 & 0 & 0 & \frac{1-2\nu}{2} & 0 & 0 \\ 0 & 0 & 0 & 0 & \frac{1-2\nu}{2} & 0 \\ 0 & 0 & 0 & 0 & 0 & \frac{1-2\nu}{2} \end{bmatrix}, \quad (2.13)$$

where E is Young's modulus, ν is Poisson's ratio.

So far, the potential and kinetic energy have been described as functions of the displacement vector

$$P = \frac{1}{2} \int_V \mathbf{u}^T \mathbf{D}^T \mathbf{E}^T \mathbf{D}\mathbf{u} dV \quad (2.14)$$

The substitution of Equations (2.4) and (2.14) into the Lagrange equation of the second kind (2.1)

provides a weak formulation of dynamic structural analysis that is used in the current research.

Within the FE framework, the unknown solution for the displacement vector is supposed to be approximated by the shape functions. These are assumed to be simple linear (tri-linear) or quadratic in this study.

Such simple approximations are suitable for small gradients of displacements changing and simple linear geometry of the body. To extend the usability of such simple approximations, the FE concept proposes virtually dividing the total body into small elements, called FE, with a regular geometric shape. That virtual dividing provides a partial discretization of the body, and for relatively small sizes of FE, all the approximative assumptions ought to be satisfied.

The weak formulations of explicit structural dynamics are the same as for the whole body and for each part, i.e., FE, as well, so the kinetic energy can be formulated for the element as follows

$$T_e = \frac{1}{2} \int_{V_e} \dot{\mathbf{u}}^T \rho \dot{\mathbf{u}} dV_e \quad (2.15)$$

The potential energy is determined as follows

$$P_e = \frac{1}{2} \int_{V_e} \mathbf{u}^T \mathbf{D}^T \mathbf{E}^T \mathbf{D} \mathbf{u} dV_e, \quad (2.16)$$

where V_e is a volume of e^{th} FE.

Within a region of some e^{th} FE, the approximation of the displacement vector could be given by shape functions

$$\mathbf{u}_e(x,y,z,t) = \mathbf{N}_e(x,y,z) \mathbf{q}_e(t), \quad (2.17)$$

where \mathbf{q}_e is a nodal displacement vector, which presents the values of displacements in the nodes of e^{th} FE. So, for some FE with volume, V_e , one can obtain

$$T_e = \frac{1}{2} \int_{V_e} \dot{\mathbf{q}}_e^T \mathbf{N}_e^T \rho \mathbf{N}_e \dot{\mathbf{q}}_e dV_e \quad (2.18)$$

Equation (2.18) can be rewritten as follows

$$T_e = \frac{1}{2} \dot{\mathbf{q}}_e^T \left(\int_{V_e} \mathbf{N}_e^T \rho \mathbf{N}_e dV_e \right) \dot{\mathbf{q}}_e \quad (2.19)$$

As a result it follows that

$$T_e = \frac{1}{2} \dot{\mathbf{q}}_e^T \mathbf{M}_e \dot{\mathbf{q}}_e, \quad (2.20)$$

where \mathbf{M}_e is a mass matrix of e^{th} FE.

For the potential energy we obtain

$$P_e = \frac{1}{2} \int_{V_e} \mathbf{q}_e^T \mathbf{N}_e^T \mathbf{D}^T \mathbf{E}^T \mathbf{D} \mathbf{q}_e dV_e, \quad P_e = \frac{1}{2} \mathbf{q}_e^T \left(\int_{V_e} \mathbf{N}_e^T \mathbf{D}^T \mathbf{E}^T \mathbf{D} \mathbf{N}_e dV_e \right) \mathbf{q}_e, \quad (2.21)$$

$$P_e = \frac{1}{2} \mathbf{q}_e^T \mathbf{K}_e \mathbf{q}_e, \quad (2.22)$$

where \mathbf{K}_e is a FE stiffness matrix

$$\mathbf{K}_e = \int_{V_e} \mathbf{B}_e^T \mathbf{E}^T \mathbf{B}_e dV_e, \quad (2.23)$$

with \mathbf{B}_e being the matrix of derivatives over shape functions

$$\mathbf{B}_e = \mathbf{D} \mathbf{N}_e \quad (2.24)$$

All mentioned formulations are satisfied for all FE for the discretization of the whole body and are required to provide an assembling procedure [56].

Such a procedure is organized algorithmically considering the node numbering and neighboring. Mathematically, we have a simple matrix relation between the global vector of all nodes in the FE model and the local one representing one particular e^{th} element

$$\mathbf{q}_e = \mathbf{A}_e \mathbf{q}, \quad (2.25)$$

where \mathbf{A}_e is the matrix of indexes which has "1" and "0", so just filtered some \mathbf{q}_e from a global vector.

For the kinetic energy we obtain

$$T_e = \frac{1}{2} \dot{\mathbf{q}}^T \mathbf{A}_e^T \mathbf{M}_e \mathbf{A}_e \dot{\mathbf{q}} \quad (2.26)$$

So, the kinetic energy of the e^{th} FE is described through the global vector of nodal velocities. The total kinetic energy T is the sum of the kinetic energies of each FE

$$T = \sum_e T_e = \sum_e \frac{1}{2} \dot{\mathbf{q}}^T \mathbf{A}_e^T \mathbf{M}_e \mathbf{A}_e \dot{\mathbf{q}} = \frac{1}{2} \dot{\mathbf{q}}^T \left(\sum_e \mathbf{A}_e^T \mathbf{M}_e \mathbf{A}_e \right) \dot{\mathbf{q}}, \quad (2.27)$$

$$T = \frac{1}{2} \dot{\mathbf{q}}^T \mathbf{M} \dot{\mathbf{q}}, \quad (2.28)$$

where \mathbf{M} is expressed as

$$\mathbf{M} = \sum_e \mathbf{A}_e^T \mathbf{M}_e \mathbf{A}_e \quad (2.29)$$

Similarly, for total potential energy P , we obtain

$$P = \sum_e P_e = \sum_e \frac{1}{2} \mathbf{q}^T \mathbf{A}_e^T \mathbf{K}_e \mathbf{A}_e \mathbf{q} = \frac{1}{2} \mathbf{q}^T \left(\sum_e \mathbf{A}_e^T \mathbf{K}_e \mathbf{A}_e \right) \mathbf{q}, \quad (2.30)$$

where

$$P_e = \frac{1}{2} \mathbf{q}^T \mathbf{A}_e^T \mathbf{K}_e \mathbf{A}_e \mathbf{q} \quad (2.31)$$

In the compact form, we can write

$$P_e = \frac{1}{2} \mathbf{q}^T \mathbf{K} \mathbf{q}, \quad (2.32)$$

where

$$\mathbf{K} = \sum_e \mathbf{A}_e^T \mathbf{K}_e \mathbf{A}_e, \quad (2.33)$$

with \mathbf{M} and \mathbf{K} being the global mass and stiffness matrix, respectively [101].

Substituting the last to the Lagrange equation of the second kind, one can obtain a general structural dynamic matrix formulation within the FE framework

$$\mathbf{M} \ddot{\mathbf{q}} + \mathbf{K} \mathbf{q} = 0 \quad (2.34)$$

Equation (2.34) represents the dynamic statement of the conservative system (without damping

phenomena) and it doesn't consider any external forces. The first assumption can be justified in the present work as all the studies are supposed to be done in static or impact.

The external forces could be considered additionally. Such a case will be described below.

However Equation (2.34) has its own practical importance, as its solution provides us the spectrum of natural frequencies and eigen modes.

2.2.2 Determination of natural frequencies and eigenmodes

Modal analysis is an analysis of the dynamic characteristics of a mechanical system that allows us to estimate possible frequency responses under real dynamic influences, to search for linear approximations by series decomposition, etc. [67, 101, 102]. In this study, the modal analysis was performed in order to test the computational models and verify them with analytical solutions based on simplified partial expansions. In addition, estimation of the natural frequencies spectrum helps determine the integration parameters over time in explicit dynamics and, of course, in the peridynamic setting. The identified frequencies allow us to quantitatively divide the load rates into those that can be considered quasi-static and those that are dynamic.

Formally, mathematical modal analysis is obtaining non-trivial solutions of a conservative homogeneous dynamic system given in Equation (2.34). The physical non-trivial solution of Equation (2.34) is a hypothetical motion in which all material points of the system will perform harmonic vibrations with the same frequency [101, 102]

$$\mathbf{q} = \mathbf{s} \sin(\omega t + \phi), \quad (2.35)$$

where \mathbf{s} is normal mode vector, ω is eigen frequency (in radians), ϕ is constant phase.

Substitution Equations (2.35) into (2.34) gives us

$$(-\omega^2 \mathbf{M} \mathbf{s} + \mathbf{K} \mathbf{s}) \sin(\omega t + \phi) = 0, \quad (\mathbf{K} - \omega^2 \mathbf{M}) \mathbf{s} = 0 \quad (2.36)$$

This is a homogeneous system of linear algebraic equations with constant coefficients for which non-trivial solutions exist if the determinant of the matrix is zero. This requirement provides an equation for finding the frequency at which modal motions are possible

$$\omega : \det(\mathbf{K} - \omega^2 \mathbf{M}) = 0 \quad (2.37)$$

Considering the problem's dimensionality, this equation has as many solutions as the degrees of freedom in the system, that is, the dimensions of the mass and stiffness matrices. Since \mathbf{K} and \mathbf{M} are symmetric and positive definite, then ω are all real.

2.2.3 Forced and contact loading

In the case of forced dynamics, i.e., external forces, one could modify the Lagrange functions, including the work of external forces [67]

$$L = T + P - W, \quad (2.38)$$

where W is the work of external forces

$$W = \int_S \mathbf{u}^T \mathbf{p} dS, \quad (2.39)$$

with S being the surface on which the distributed forces \mathbf{p} are applied respectively

$$\mathbf{p} = \{p_1(x, y, z, t) \ p_2(x, y, z, t) \ p_3(x, y, z, t)\}^T \quad (2.40)$$

Considering Equations (2.39) and (2.38), we can modify an equation for the general structural dynamic matrix formulation with external forces

$$\mathbf{M}\ddot{\mathbf{q}} + \mathbf{K}\mathbf{q} = \mathbf{f}(t), \quad (2.41)$$

where \mathbf{f} is the vector of external loads reduced to nodes.

Vector of external loads reduced to nodes has the form

$$\mathbf{f}_e(t) = \int_S \mathbf{N}_e^T(x, y, z) \mathbf{p}(x, y, z, t) dS, \quad \mathbf{f}(t) = \sum_e \mathbf{A}_e^T \mathbf{f}_e(t) \quad (2.42)$$

Additional problems arise when one body impacts another, so the current work should solve the contact problem. Two bodies interact with each other through contact forces. These forces are unknown until the deformation itself and depend on how the bodies come into contact and how their surfaces are deformed. Mathematically and formally, the whole problem will ultimately come down to the fact that contact forces will be added to the system [34].

Let's define pairs of nodes of the finite element partition $\bar{\mathbf{q}}_c = \{q_i^{contact}, q_i^{target}\}_{i=1}^{N_c}$, that can potentially come into contact during the process of structure deformation. We compile a set of penetration conditions (restrictions) for each pair of contact nodes $a_i(\bar{\mathbf{q}}_c) \geq 0, \forall i, \overline{1, N}$.

A pair of contact nodes is chosen, for which the following condition is satisfied

$$\mathbf{a}(\mathbf{q}_c) \geq 0 \quad (2.43)$$

Thus, the minimization of the functional, which is formally presented in the Lagrange equations of the second kind, cannot be performed as before since it involves a constraint in the form of an inequality. The problem of constrained minimization can be reduced to an unconstrained minimization based on the Kuhn-Tucker theorem by introducing additional Lagrange multipliers and penalty terms. Without delving into the details of this mathematical procedure, since it is classical and was used in this work in its simplest form, it should be noted that this formally leads to a modification of the expression for potential energy, Equation (2.5), by adding terms that, for each pair of contact nodes, connect the non-penetration equations $\mathbf{a}(\mathbf{q}_c)$ and the Lagrange multipliers

$$\bar{P} = P(\mathbf{q}) + \sum_{j=1}^{N_c} \frac{\zeta_j}{2} \left(a_j(\bar{\mathbf{q}}_c) + \frac{\lambda_j^2}{\zeta_j} \right)^2 - \sum_{i=1}^{N_c} \frac{\lambda_i^2}{2\zeta_i}, \quad (2.44)$$

where λ_i are the Lagrange multipliers, which have a mechanical meaning as contact reactions. ζ_j are penalties that have a mechanical meaning as stiffness.

After substituting the new function \bar{P} into the Lagrange equation, we obtain an additional term $\mathbf{f}_c(\mathbf{q})$

$$\mathbf{M}\ddot{\mathbf{q}} + \mathbf{K}\mathbf{q} + \mathbf{f}_c(\mathbf{q}) = \mathbf{f}(t), \quad (2.45)$$

where \mathbf{f}_c is contact force vector, which depends on \mathbf{q}

$$\mathbf{f}_c(\mathbf{q}) = \sum_{j=1}^{N_c} \zeta_j \left(a_j(\bar{\mathbf{q}}_c) + \frac{\lambda_j}{\zeta_j} \right) \nabla a_j(\bar{\mathbf{q}}_c) \quad (2.46)$$

In this case, Equation (2.45) becomes non-linear. Typically it could be solved iteratively. A simple iterative approach is applied to static problems as well as to dynamic ones when using an explicit time integration scheme at each step.

In the static formulation Equation (2.45) takes the form

$$\mathbf{K}\mathbf{q} + \mathbf{f}_c(\mathbf{q}) = \mathbf{f}(t), \quad (2.47)$$

and the solution algorithm can be formulated as follows

1. The contact node pairs are determined, and the geometric non-penetration condition is established for each pair. These expressions may vary depending on the type of contact elements, which consider conditions such as node-to-node, node-to-surface, and surface-to-surface interactions. In this work, the surface-to-surface approach was used.
2. The initial values of the Lagrange multipliers and penalty terms are set and determined based on the contact stiffness.
3. The contact forces are calculated for these initial values of the Lagrange multipliers, penalty

terms, and non-penetration conditions.

4. The static equation is solved to determine the nodal displacement vector of the system under the external load and the current value of the contact force vector

$$\mathbf{K}\mathbf{q}^{k+1} = \mathbf{f}(t) - \mathbf{f}_c(\mathbf{q}^k) \quad (2.48)$$

5. The Lagrange multipliers are iteratively updated

$$\lambda_j^{k+1} = \lambda_j^k + \zeta_j a_j(\bar{\mathbf{q}}^k) \quad (2.49)$$

In this process, the non-penetration condition is evaluated using the displacements of the contact nodes determined in the previous step.

6. Steps 3–5 are repeated until convergence

$$|q^k| - |q^{k-1}| < \eta, \quad (2.50)$$

where η is the error considered to be acceptable.

The presented formulations and algorithm are provided for frictionless contact in a general schematic formulation. In dynamic problems, the same scheme is applied but embedded within the general explicit time integration algorithm, which will be considered in the next section. The penalty parameters serve as control parameters of the algorithm (essentially defined by the user) and physically represent contact stiffness. This work used a standard approach to be calculated based on material properties and geometry under Hertzian theory to estimate this value

$$K_c = \frac{4}{3}E^*\sqrt{R^*}, \quad (2.51)$$

where E^* is the effective elastic modulus, and R^* is the effective curvature radius.

2.2.4 Explicit dynamic analysis

The current work used transient analysis to solve dynamic impact problems with the linear elastic material model. In transient analysis, the objective is to study the response of a system over time when subjected to time-varying loads, capturing how displacements, velocities, stresses, and strains evolve with time [8]. Damping was not considered in the research, so we will not take it into account in further equations.

The equation of motion is

$$\mathbf{M}\ddot{\mathbf{q}} + \mathbf{K}\mathbf{q} + \mathbf{f}_c(\mathbf{q}) = \mathbf{f}(t) \quad (2.52)$$

To obtain \mathbf{q} itself, we need to solve the system of linear differential equations. These can be solved by integration concerning time. This time, integration can be accomplished numerically using a finite difference scheme. The corresponding procedure is referred to as the explicit finite element procedure.

The whole time interval of the dynamic problem in consideration is subdivided into small time increments Δt . We consider this time increment around the current time moment t and assume that the vector of degrees of freedom \mathbf{q} is known at t and $t - \Delta t$. Developing then \mathbf{q} in Taylor series around the time point $t + \Delta t/2$ we get

$$\mathbf{q}(t) = \mathbf{q}|_{t+\frac{\Delta t}{2}} + \dot{\mathbf{q}}|_{t+\frac{\Delta t}{2}} \left[t - \left(t + \frac{\Delta t}{2} \right) \right] + \dots \quad (2.53)$$

$$\mathbf{q}(t) = \mathbf{q} \left(t + \frac{\Delta t}{2} \right) - \dot{\mathbf{q}} \left(t + \frac{\Delta t}{2} \right) \frac{\Delta t}{2} + \dots \quad (2.54)$$

$$\mathbf{q}(t + \Delta t) = \mathbf{q}|_{t+\frac{\Delta t}{2}} + \dot{\mathbf{q}}|_{t+\frac{\Delta t}{2}} \left[t + \Delta t - \left(t + \frac{\Delta t}{2} \right) \right] + \dots \quad (2.55)$$

$$\mathbf{q}(t + \Delta t) = \mathbf{q} \left(t + \frac{\Delta t}{2} \right) + \dot{\mathbf{q}} \left(t + \frac{\Delta t}{2} \right) \frac{\Delta t}{2} + \dots \quad (2.56)$$

The Equations (2.54) and (2.56) can be used to obtain algebraic equations for the velocity in the middle time point of the time step.

Subtracting the second equation from the first one and neglecting second and higher order terms, we get

$$\dot{\mathbf{q}} \left(t + \frac{\Delta t}{2} \right) = \frac{\mathbf{q}(t + \Delta t) - \mathbf{q}(t)}{\Delta t} \quad (2.57)$$

The numerical procedure evaluating a function's derivative in the interval's middle point from the values in its ends is referred to as the central difference scheme. Similarly, we can also write

$$\dot{\mathbf{q}} \left(t - \frac{\Delta t}{2} \right) = \frac{\mathbf{q}(t) - \mathbf{q}(t - \Delta t)}{\Delta t} \quad (2.58)$$

Applying the same procedure for the second time derivative of $\mathbf{q}(t)$ we get

$$\ddot{\mathbf{q}}(t) = \frac{\dot{\mathbf{q}} \left(t + \frac{\Delta t}{2} \right) - \dot{\mathbf{q}} \left(t - \frac{\Delta t}{2} \right)}{\Delta t} \quad (2.59)$$

Inserting now the values obtained for $\dot{\mathbf{q}}\left(t + \frac{\Delta t}{2}\right)$ and $\dot{\mathbf{q}}\left(t - \frac{\Delta t}{2}\right)$ yields

$$\ddot{\mathbf{q}}(t) = \frac{\mathbf{q}(t + \Delta t) - 2\mathbf{q}(t) + \mathbf{q}(t - \Delta t)}{\Delta t^2} \quad (2.60)$$

and consequently

$$\mathbf{q}(t + \Delta t) = \ddot{\mathbf{q}}(t)\Delta t^2 + 2\mathbf{q}(t) - \mathbf{q}(t - \Delta t), \quad (2.61)$$

$$\ddot{\mathbf{q}}(t) = \mathbf{M}^{-1}(\mathbf{f}(t) - \mathbf{K}\mathbf{q}(t) - \mathbf{f}_c(\mathbf{q})) \quad (2.62)$$

Thus, the workflow of an explicit finite element procedure can be represented as follows

- Calculate the mass matrix
- Update surface load vector \mathbf{f} (which can depend on displacements)
- Update deformations

$$\mathbf{q}(t + \Delta t) = \mathbf{M}^{-1}(\mathbf{f}(t) - \mathbf{K}\mathbf{q}(t) - \mathbf{f}_c(\mathbf{q}))\Delta t^2 + 2\mathbf{q}(t) - \mathbf{q}(t - \Delta t) \quad (2.63)$$

- Set $t := t + \Delta t$ and return to second step

The following numerical features of the explicit finite element method should be taken into account.

- Stability condition and time step size. The explicit finite element procedure is generally stable for somewhat small time step sizes which should satisfy the condition

$$\Delta t < \frac{4\pi}{\omega}, \quad (2.64)$$

where ω denotes the highest natural frequency (eigenfrequency) of the (whole) structure in consideration. However, the calculation of the latter one is in general difficult since it requires the eigenfrequency analysis which is numerical expensive. For this reason, the generally higher eigenfrequency of particular elements is used for the stability criterion

- Diagonal mass matrix is crucial for the efficiency and practicability of the explicit finite element procedure. For this reason, the generally non-diagonal mass matrix \mathbf{M} is diagonalized. The most simple procedure of the diagonalization is to sum up the elements of the mass matrix column or row wise as follows

$$\bar{M}_{kl} = \delta_{kl} \sum_{i=1}^n M_{ik}, \quad (2.65)$$

where δ_{kl} is the Kronecker symbol.

- Mass scaling can additionally be applied in order to improve efficiency of the explicit finite element procedure. In this case, the values of the lumped mass matrix \bar{M}_{kl} are proportionally increased. The additional error introduced by this scaling is shown to be acceptable as far as the kinetic energy of the system does not exceed 10% of its whole energy.

2.3 Modeling using peridynamic theory

2.3.1 Basic formulation of linear peridynamic solid model

Peridynamic theory is a generalized continuum mechanics to account for long-range force interactions between material points [9, 84]. In contrast to the CCM, the balance equations do not contain partial derivatives concerning spatial coordinates [52].

In contrast to the CCM, differential line elements are not introduced. The vector between \mathbf{x} and any point in its family is called a bond, defined as ξ with the finite size and presented in Figure 2.1. It connects material points \mathbf{x} and \mathbf{x}' , in the reference configuration is considered as

$$\xi = \mathbf{x}' - \mathbf{x} \quad (2.66)$$

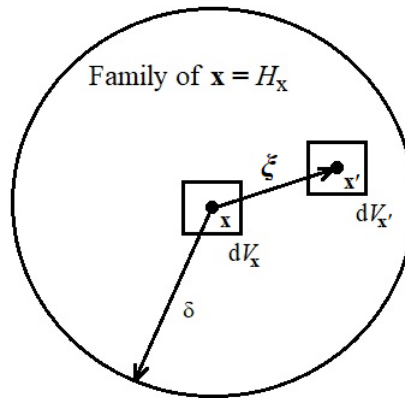


Figure 2.1: Material points interaction

Peridynamic models are frequently written using states ($\langle \text{text in angle brackets} \rangle$), which are operators that act on vectors in H_x , that is a finite size spherical integral region with \mathbf{x} as the center and δ , which is called the horizon, as the radius. A vector state is an operator whose image is a vector and may be viewed as a generalization of a second-rank tensor. The peridynamic deformation state is $\underline{\mathbf{Y}}\langle \xi \rangle$ (Figure 2.2), where the notation is understood to mean that the vector state $\underline{\mathbf{Y}}$ maps a bond vector ξ which belongs to H_x to a vector in three-dimensional (3D) state. In a real configuration $\underline{\mathbf{Y}}[\mathbf{x}, t]\langle \xi \rangle$ we can now express as the difference between new configuration in this position $\mathbf{y}(\mathbf{x} + \xi, t)$ and the previous one $\mathbf{y}(\mathbf{x}, t)$ for current time. Square brackets of the deformation state $\underline{\mathbf{Y}}$ are introduced to represent that the state currently depends on a coordinate \mathbf{x} and time t

$$\underline{\mathbf{Y}}[\mathbf{x}, t] \langle \xi \rangle = \mathbf{y}(\mathbf{x} + \xi, t) - \mathbf{y}(\mathbf{x}, t), \quad \mathbf{y} = \mathbf{x} + \mathbf{u} \quad (2.67)$$

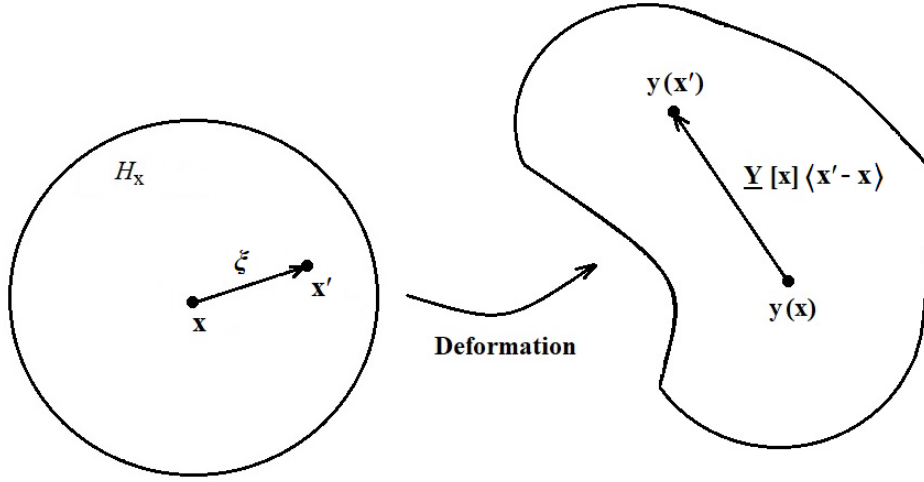


Figure 2.2: Peridynamic deformation state

For actual configuration, the balance of linear momentum states that the rate of change of momentum for any part of the solid is equal to the resultant force acting on that part. So that linear momentum balance is the volume integral over all forces around all bonds [84] described in the formula below

$$\rho \ddot{\mathbf{u}}(\mathbf{x}, t) = \int_{H_x} (\underline{\mathbf{T}}[\mathbf{x}, t] \langle \mathbf{x}' - \mathbf{x} \rangle - \underline{\mathbf{T}}[\mathbf{x}', t] \langle \mathbf{x} - \mathbf{x}' \rangle) dV_{\mathbf{x}'} + \mathbf{b}(\mathbf{x}, t), \quad (2.68)$$

where ρ is the mass density, \mathbf{u} is the displacement vector. $\underline{\mathbf{T}}[\mathbf{x}, t] \langle \mathbf{x}' - \mathbf{x} \rangle$ is the peridynamic force density state for the bond ξ , $dV_{\mathbf{x}'}$ is the infinitesimal small volume associated with \mathbf{x}' , \mathbf{b} represents the external body force density of \mathbf{x} . The Equation of motion (2.68) can also be formulated as follows

$$\rho \ddot{\mathbf{u}} = \int_H (\underline{\mathbf{T}}[\mathbf{x}, t] \langle \xi \rangle - \underline{\mathbf{T}}[\mathbf{x}', t] \langle -\xi \rangle) dV_{\xi} + \mathbf{b} \quad (2.69)$$

The peridynamic force density state is related to the deformation state for each particular bond by the defining equation. In the current study, the linear peridynamic solid material model is applied [83]

$$\underline{\mathbf{T}} \langle \xi \rangle = \underline{\mathbf{t}} \langle \xi \rangle \underline{\mathbf{M}} \langle \xi \rangle, \quad \underline{\mathbf{M}} = \frac{\underline{\mathbf{Y}}}{|\underline{\mathbf{Y}}|} \quad (2.70)$$

with

$$\underline{t}(\xi) = \frac{3K}{m} \theta \underline{\omega}(\xi) |\xi| + \frac{15G}{m} \underline{\omega}(\xi) \underline{e}^d(\xi), \quad (2.71)$$

where $\underline{\omega}(\xi)$ is the influence function, G is the shear modulus, the bulk modulus K is defined by

$$K = \frac{E}{3(1 - 2\nu)} \quad (2.72)$$

The nonlocal dilatation θ , the weighted volume m and the deviatoric part of extension $\underline{e}^d(\xi)$ are defined as follows

$$\theta = \frac{3}{m} \int_H (|\underline{Y}(\xi)| - |\xi|) \underline{\omega}(\xi) |\xi| dV_\xi, \quad (2.73)$$

$$m = \int_H \underline{\omega}(\xi) |\xi|^2 dV_\xi, \quad (2.74)$$

$$\underline{e}^d(\xi) = |\underline{Y}(\xi)| - |\xi| - \frac{1}{3} \theta |\xi| \quad (2.75)$$

2.3.2 Damage and fracture modeling

The previously described formulations allow us to introduce the subsequent damage model since the broken bonds are the deformed state parameter of getting to some level. Damage to brittle materials is introduced at the bond level [53]. For such permission, a new stretch parameter of the bond should be introduced, which can be calculated as the relative difference between the bond state of deformed and previous positions. The stretch of the bond s is calculated as follows

$$s(\xi) = \frac{|\underline{Y}(\xi)| - |\xi|}{|\xi|} \quad (2.76)$$

In a 3D state, each point has a certain number of neighbors and many different bonds. To introduce the general damage variable, we can introduce an interpretive representation, which will be the general integral over the volume of the investigated point \mathbf{x} along the horizon divided by its volume. The damage variable φ is

$$\varphi = \frac{\int_H (1 - \mu) dV_\xi}{\int_H dV_\xi}, \quad (2.77)$$

2 Theoretical Background

where μ is a piecewise function for condition of stretch for one bond ξ . If the tensile bond stretch reaches the critical value s_c , the bond is considered broken [9, 33, 82]. The damaged state at point \mathbf{x} is the result of a collection of broken bonds

$$\mu(\xi, t) = \begin{cases} 1 & s_T(\xi, t') < s_c \quad 0 \leq t' \leq t \\ 0 & \text{otherwise} \end{cases}, \quad (2.78)$$

where the tensile bond stretch is

$$s_T = \frac{s + |s|}{2} \quad (2.79)$$

With the damage function μ the Equations (2.71) and (2.73) take the form

$$\underline{t}(\xi) = \frac{\mu \underline{\omega}(\xi)}{m} (3K\theta|\xi| + 15G\mathbf{e}^d(\xi)), \quad (2.80)$$

$$\theta = \frac{3}{m} \int_H (|\underline{\mathbf{Y}}(\xi)| - |\xi|) \mu \underline{\omega}(\xi) |\xi| dV_\xi \quad (2.81)$$

Equations (2.70 – 2.81) are substituted into (2.68) and integrated for each points to get the governing dynamic differential equation for \mathbf{x} coordinate point [82].

3 Finite element modeling of laminated glasses under dynamic loading

3.1 Finite element model development and verification within linear modal and impact benchmarks

3.1.1 Monolithic glass plate benchmarks

Studying glass plates' behavior subjected to impact loading is valuable for investigating thin-walled structural elements. Practical applications encounter numerous challenges: the presence of complex boundary conditions, difficulties with convergence in computations, the influence of multilayered structures, and variations in curvilinear geometries. Such challenges demand advanced numerical methodologies for accurate problem-solving. However, to gain acceptance and reliability, it is essential to validate these computational models rigorously, especially in controlled scenarios where empirical data or analytical solutions can be obtained to serve as benchmarks. A fundamental aspect of this validation process is to assess the fidelity of numerical models by comparing their solutions for impact-induced dynamic responses with those derived from linearized vibration analysis of plates under impact loads.

This part provides an investigation of the linear transient dynamics of glass plates, focusing on frequency analysis and displacement characteristics under impact conditions.

The following steps will be performed to solve the glass plate benchmark:

- To set up an analytical solution that characterizes the behavior of a glass plate under impact loading conditions, establishing a reference for further comparisons.
- To perform a modal analysis of a glass plate to compare with analytical values.
- To develop a computational mathematical model that enables investigation of the impact force on a glass plate and to conduct numerical analyses.
- To compare the results of numerical and analytical studies, evaluate the accuracy level, and provide recommendations regarding the parameters of the computation model.

A glass plate with length $a = 500$ mm, width $b = 750$ mm and thickness $h = 6.38$ mm is modeled and studied (Figure 3.1). The material properties of glass model with density $\rho = 2500$ kg/m³, Young's modulus $E = 70$ GPa, and Poisson ratio $\nu = 0.23$ were used. A hit on a plate with a solid body of mass $m_b = 1$ kg that moves with a velocity of $v_b = 8$ m/s was considered. The current data correspond to the majority of experimental data in the literature. The boundary conditions of the plate were set as simply supported all sides.

This part of the work will focus on the elastic body hit theory. The function $u_z(t)$ describes the lateral displacement of the plate caused by the concentrated contact force $F(t)$ at the contact

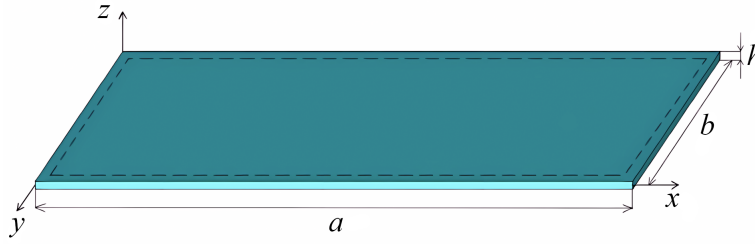


Figure 3.1: Simulation model

point in the center of the plate with the coordinates (x_c, y_c) . This displacement can be determined through the differential equation governing the constrained vibrations of the plate, influenced by a surface load $f_s(x, y, t)$ that depends on time and coordinates

$$D\nabla^4 u_z + \rho h \frac{\partial^2 u_z}{\partial t^2} = f_s, \quad (3.1)$$

where D is the bending stiffness defined as follows

$$D = \frac{Eh^3}{12(1 - \nu^2)} \quad (3.2)$$

Equation (3.1) includes $f_s(x, y, t)$, which in this specific case is used as a concentrated contact force $F(t)$ to simulate the impact. The solution to Equation (3.1) can be obtained analytically in a linear statement. For this purpose, the series expansion in the plate's natural modes was used. Natural frequencies and normal modes could be figured out from modal analysis, and then we set a zero right-hand side in Equation (3.1)

$$D\nabla^4 u_z + \rho h \frac{\partial^2 u_z}{\partial t^2} = 0 \quad (3.3)$$

Here, we will find harmonic motions as follows

$$u_z(x, y, t) = H(x, y) \sin(\omega t), \quad (3.4)$$

where $H(x, y)$ is function that describe the normal mode of plate in CCM, ω is natural frequency.

Since the Equation (3.3) is ordinary, there will be an infinite number of solutions like Equation (3.4). Substituting Equation (3.4) to (3.3) considering free support boundary conditions, one will find the following formulas for the natural frequencies of the plate

$$\omega_{nk} = hp_{nk}^2 \sqrt{\frac{E}{3\rho(1 - \nu^2)}}, \quad (3.5)$$

$$p_{nk}^2 = \left(\frac{n\pi}{a}\right)^2 + \left(\frac{k\pi}{b}\right)^2, \quad n, k = 1.. \infty \quad (3.6)$$

We will use these analytical values of natural frequencies to test the models (see Table 3.1).

The solution to Equation (3.5) is obtained in the form of decomposition by normal modes H_{nk} at the point of contact (x_c, y_c)

$$H_{nk} = \sin\left(\frac{n\pi x}{a}\right) \sin\left(\frac{k\pi y}{b}\right) \quad (3.7)$$

The natural frequency and normal modes spectrum were determined using numerical methods within a 3D computer modeling framework and the FEM. A preliminary assessment of the numerical model's accuracy was conducted by comparing numerical results with analytical solutions for a given case, giving recommendations for key modeling parameters, including the optimal FE mesh density.

Modal analysis was performed using a hexagonal FE with 20 nodes, each with 3 degrees of freedom. The plate was modeled under a linear-elastic physical assumption. FE meshes of varying element sizes were created for the analysis. The FE mesh model is illustrated in Figure 3.2.

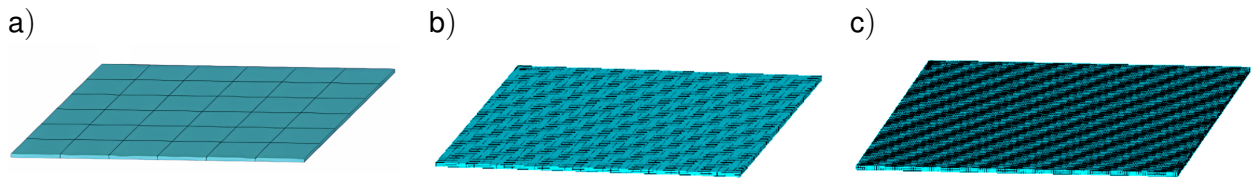


Figure 3.2: Mesh size of the model.
a) 95.7 mm, b) 12.76 mm, c) 3.19 mm

Three different meshes of the glass plate with 95.7 mm (6 elements in length, 1 element in thickness), 12.76 mm (39 elements in length, 2 elements in thickness) and 3.19 mm (157 elements in length, 3 elements in thickness) were considered. Natural frequencies were calculated to assess computational accuracy for each mesh size. A comparison between analytical and numerical results demonstrates a strong correlation, indicating that the FEM approach can reliably approximate natural frequencies. The relative error between frequency values for mesh sizes of FEs 95.7 mm and 12.76 mm is over 2%, while the error between mesh sizes of 12.76 mm and 3.19 mm is minimal. Thus, for this study, a mesh size of 12.76 mm was selected as a balance between computational efficiency and accuracy.

Table 3.1 presents a detailed comparison between analytical and numerical frequencies using the mentioned mesh. The table shows a minor relative error for each frequency value, with most errors under 1%, underscoring the accuracy of the FEM model. Additionally, Figure 3.3 illustrates various natural modes corresponding to the calculated frequencies. This visual representation provides insight into the vibrational behavior of the plate, reinforcing the validity of both the numerical and analytical approaches in capturing the plate's characteristics.

Table 3.1: The results of frequencies calculations

Frequency number (FN)	Wave number n k	Analytical frequency (Hz)	Numerical frequency (Hz)	Relative error (%)
1	1 1	90.88	90.46	0.46
2	1 2	174.78	173.84	0.54
3	1 3	314.60	313.16	0.46
4	1 4	510.35	508.14	0.43
5	2 1	279.65	278.81	0.30
6	2 2	363.54	361.41	0.59
7	2 3	503.36	499.74	0.72
8	2 4	699.11	693.78	0.76
9	3 1	594.25	592.22	0.34
10	3 2	678.14	674.31	0.56

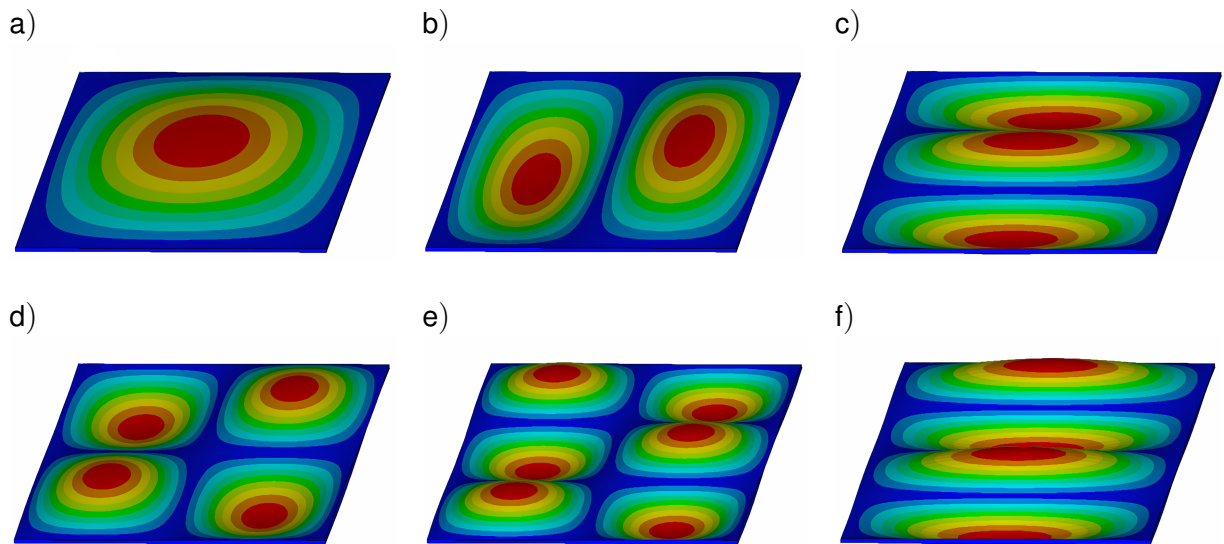


Figure 3.3: Natural plate modes according to frequencies.

a) first frequency number (FN), b) third FN, c) fourth FN, d) fifth FN, e) sixth FN, f) seventh FN

An equally important aspect of verifying the accuracy of numerical modeling is comparing the numerical results of the impact interaction between a plate and another solid body and an approximate analytical calculation for the plate under impact loading. This comparison becomes particularly relevant if the time dependence of the force transmitting the impact load aligns with the contact interaction force.

In the following sections of this work, the problem of the impact loading of a ball on a plate will be solved. At this stage, we aim to replace the actual surface load of the ball with an approximate force function. The comparison of the results for both models aids in refining the model parameters to enhance its predictive accuracy for impact scenarios.

To obtain an analytical distribution, it is necessary to define how the contact force (or pressure) is applied over time in the equations. This ensures that the analytical solution gives accurate

results. Various sources in the literature suggest approximating this force using simplified shapes such as half-sine waves, half-ellipses, and triangular or rectangular impulses, each of which significantly influences the analytical solution. It is essential to account for the contact interaction time and impact value. Typically, analytical studies rely on contact time estimates derived from experimental data.

Two half-sine waves ensure a smooth loading process while making the impact asymmetric (rapid at the beginning and slower afterward) since this better represents the actual impact process. The duration and peak force were selected to match the values used in computational simulations. Then, we compare how well the resulting displacements and stresses across the entire plate, excluding the contact problem, are accurately reflected in the analytical model. The two-sine-wave approximation is validated by comparing it with the actual simulation results, as shown in Figure 3.4, where blue line shows the results for ball impact problem calculation data, and the dashed gray line is a suggested approximation in the form of half-wave sines.

Upon impact, the load function is determined at the contact force's application point $F(\tau)$. The force of the interaction at the point of contact (x_c, y_c) is set

$$F = \begin{cases} F_{\max} \sin\left(\frac{\pi\tau}{2t_m}\right), & \tau < t_m \\ F_{\max} \sin\left(\frac{\pi(\tau - (2t_m - t_{\max}))}{2(t_{\max} - t_m)}\right), & t_m < \tau < t_{\max} \\ 0, & \tau > t_{\max} \end{cases}, \quad (3.8)$$

where τ is impact time, t_m is the time at maximum force value, t_{\max} is the end loading time, F_{\max} is the maximum value of contact force.

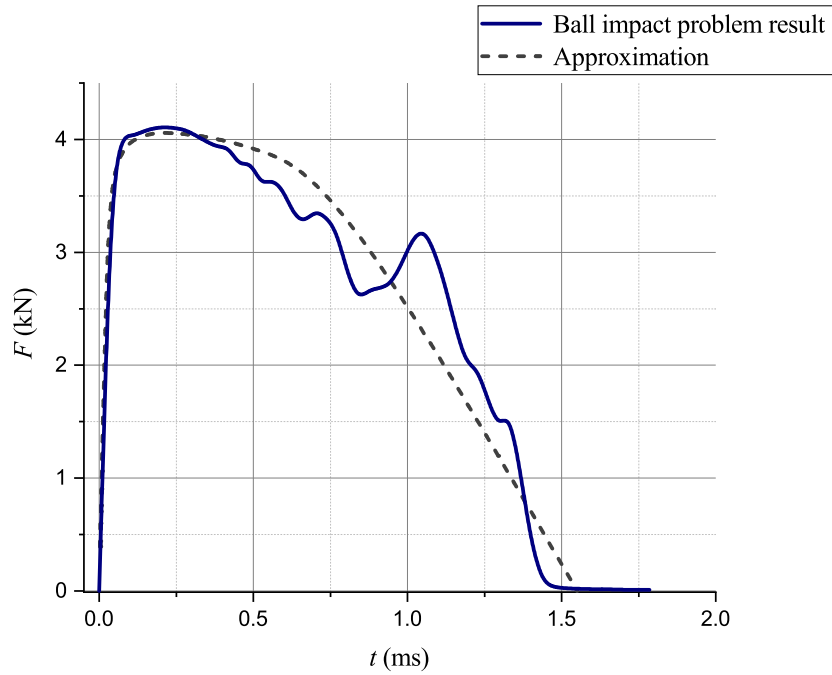


Figure 3.4: Dependence of the contact force on time

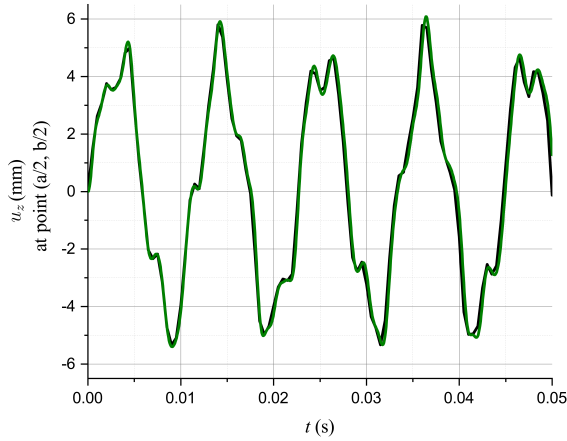
This problem setup was selected based on the approximate analytical solution to the boundary value problem available for such plates. The applied theory accounts for displacement at the

impact point and its influence on the deformation of the plate

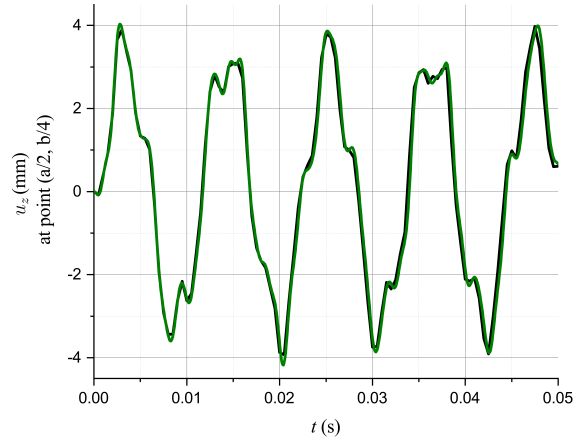
$$u_z(x, y, t) = \frac{1}{2h\rho} \sum_{n=1}^{\infty} \sum_{k=1}^{\infty} \frac{H_{nk}(x, y) H_{nk}(x_c, y_c)}{q_{nk} \iint H_{nk}^2 dx dy} \int_0^t F(\tau) \sin(q_{nk}(t - \tau)) d\tau \quad (3.9)$$

$$\sigma_{xx} = -\frac{12Dz}{h^3} \left(\frac{\partial^2 u_z}{\partial x^2} + \nu \frac{\partial^2 u_z}{\partial y^2} \right) \quad (3.10)$$

a)



b)



c)

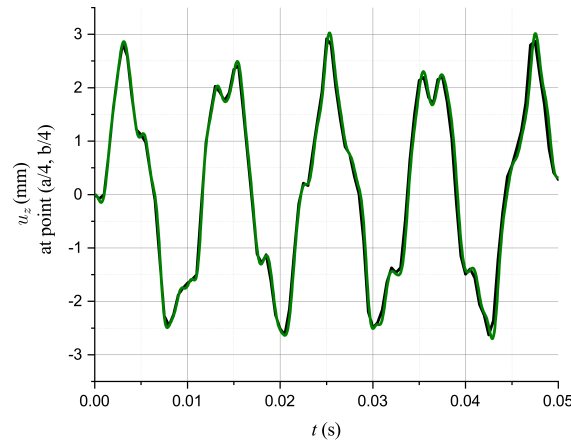


Figure 3.5: Dependence of the plate displacement u_z on time.

a) at point $(a/2, b/2)$, b) at point $(a/2, b/4)$, c) at point $(a/4, b/4)$

A numerical solution was obtained using the expansion method in a series of natural modes within the FE framework. The behavior of glass samples was modeled through transient analysis using 3D modeling and the FEM. For glass plate, displacements at various points were calcu-

lated, as shown in Figure 3.5, where the black line shows the analytical solution and the green line is the numerical solution.

The comparison between the analytical and numerical solutions for displacements at different points of the plate shows strong agreement, according to the graphs.

Based on the assumed parameters of the glass plate and the applied impact force, the tensor σ_{xx} was calculated at a point offset from the plate's center (Figure 3.6). This location was intentionally selected to avoid the singularity at the plate's center, where stresses are expected to reach theoretically infinite values due to the concentrated impact.

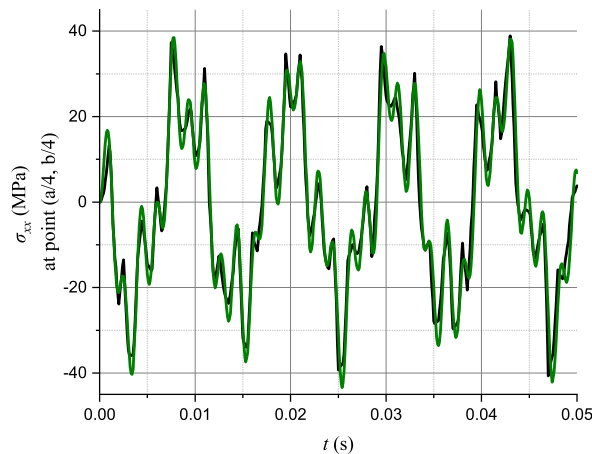


Figure 3.6: Dependence of the stress tensor component σ_{xx} of the plate on time at point $(a/4, b/4)$

The tensor σ_{xx} results are in good agreement with an error of less than 2%.

This level of accuracy confirms the model's reliability, making it suitable for further calculations. As a result, we can confidently apply this model and its parameters in future analyses of more complex models and scenarios. The validated accuracy in displacement and stress calculations provides a solid basis for extending the model's application to predict behavior under a broader range of conditions, supporting more advanced engineering and material studies.

For modal analysis, it is recommended to use 2 elements in the thickness of the glass plate with such dimensions to ensure a relatively high calculation speed and result accuracy.

3.1.2 Laminated glass finite element model accuracy estimation

Following the benchmark analysis of a monolithic glass plate described above, this chapter extends the study to model the dynamic response of LG composite subjected to the impact of a rigid ball.

The LG model verification will be achieved through the following steps:

- 1) to develop a computer-based mathematical model for investigation of the impact interaction between a spherical rigid body and a three-layer glass composite in the FEM framework;
- 2) to perform simulations with a fixed ball velocity and interlayer thickness, evaluating the effect of varying FE mesh sizes on result accuracy.

3) to conduct simulations with varying ball velocities for different FE meshes, comparing results to estimate the numerical error of simulation results.

A three-layer LG composite subjected to the impact of a smooth solid steel ball, 83 mm in diameter (2.3 kg), was analyzed. The composite consists of two outer glass layers, each 5 mm thick, separated by a PVB interlayer with varying thicknesses of 0.38 mm, 0.76 mm, and 1.52 mm (effective interlayer thicknesses). The plate dimensions of LG are 305 mm wide and 305 mm long.

The behavior of LG with PVB interlayer was modeled as transient analysis in the 3D statement of explicit dynamic formulation of FEM. Hexagonal FE with eight nodes with three degrees of freedom was used.

As boundary conditions, the ball drop was simulated at the center of the plate, and LG was fixed on two opposite sides (Figure 3.7). The ball was modeled as a rigid body, and the composite was modeled in a three-dimensional (3D) framework within a physically linear-elastic setting. The interaction of the ball and LG was carried out using a one-way contact approach based on the "surface-to-surface" algorithm. Air resistance during the impact was neglected.

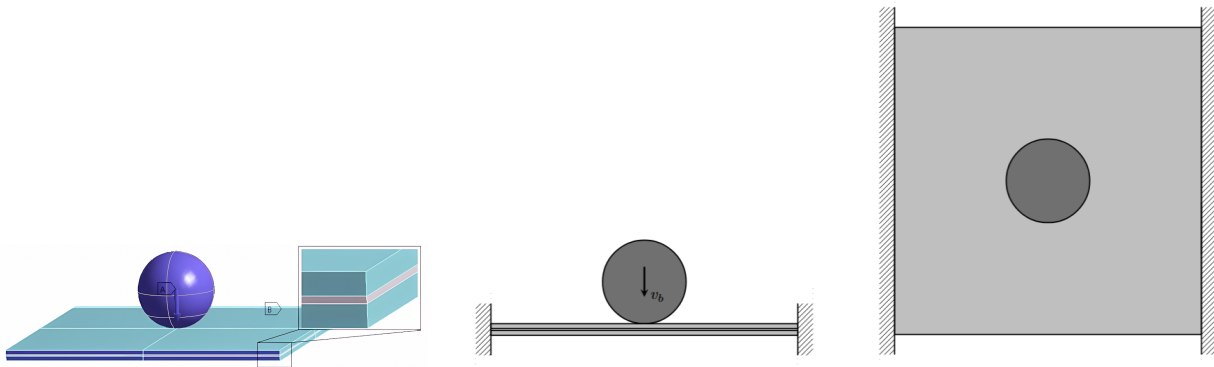


Figure 3.7: LG boundary conditions

Material properties for the glass layers, the PVB interlayer, and the ball are summarized in Table 3.2.

Table 3.2: Material properties

Material	ρ (kg/m ³)	E (GPa)	ν
Steel	7850	200	0.3
Glass	2500	70	0.23
PVB	1100	0.22	0.495

FE meshes with varying FE sizes were generated to analyze the LG model and evaluate computational accuracy. FE mesh for the laminated glass plate was modeled using a regular Cartesian grid to ensure uniformity and simplicity. Different mesh sizes were employed to systematically evaluate which configuration provides the best balance of accuracy for the model.

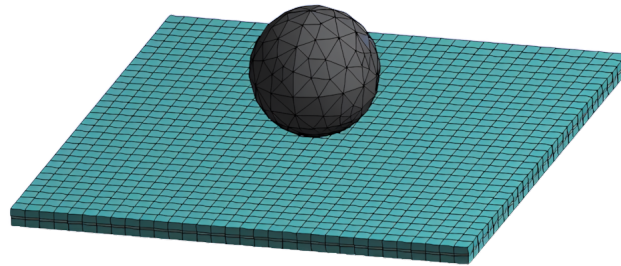
The method for finer mesh refinement near the contact region with the plate was implemented to the steel ball, ensuring higher accuracy where maximum displacements occur. The refinement

near the contact zone is critical for capturing the localized effects of the impact, thereby improving result convergence.

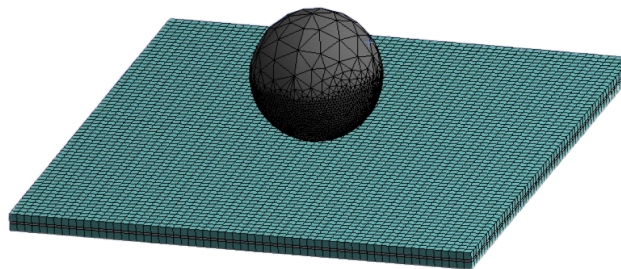
This approach allows for a detailed analysis of how mesh resolution affects the precision of displacement results across the plate.

The three FE mesh sizes are considered (Figure 3.8). For 10 mm mesh, the model has 30 elements in length and 3 elements in thickness. For 5 mm mesh, the model has 61 elements in length and 3 elements in thickness. For 2 mm mesh, the model has 152 elements in length and 5 elements in thickness.

a)



b)



c)

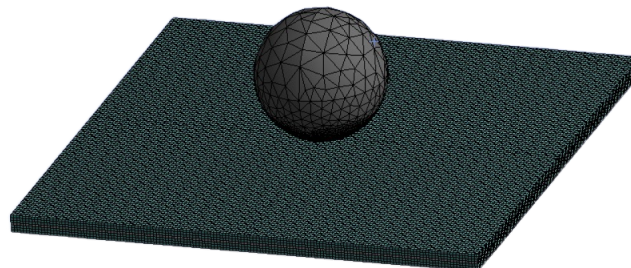


Figure 3.8: Mesh sizes of the model.

a) 10 mm, b) 5 mm, c) 2 mm

The maximum total displacements (u_{max}) were calculated for each mesh size. The simulation was performed on the LG with a 1.52 mm PVB interlayer, subjected to the impact of a ball with varying free-fall velocities (v_b). The calculated displacement values for different mesh sizes and velocities are presented in Table 3.3, providing a detailed comparison of model performance across different configurations. The number of nodes used in the FE model corresponds to FE mesh size. For each model, four cases with different free ball fall velocities, such as 3 m/s, 4.85

Table 3.3: Dependence of the results on model mesh size and ball velocity

FE mesh size (mm)	Number of nodes	v_b (m/s)	u_{max} (mm)
10	4825	3	2.87
		4.85	4.61
		5.3	5.79
		6	6.52
5	17322	3	3.13
		4.85	4.67
		5.3	5.01
		6	5.21
2	206294	3	1.86
		4.85	2.96
		5.3	3.22
		6	3.64

m/s, 5.3 m/s and 6 m/s are considered. The value of maximum total displacements for each case is obtained.

The coarsest mesh size (10 mm) provides a rough approximation of the maximum deformation, particularly for lower ball velocities (e.g., 3 m/s and 4.85 m/s). However, at higher velocities (e.g., 5.3 m/s and 6 m/s), the 10 mm mesh exhibits significant discrepancies compared to finer meshes, with percent differences exceeding 15% when compared to the 5 mm mesh. This highlights the limitations of coarser meshes in capturing the sharp deformation gradients induced by higher impact energies. The 5 mm mesh significantly improves accuracy compared to the 10 mm mesh, with percent differences for lower velocities (e.g., 4.85 m/s) dropping to approximately 1.29%. This indicates that the 5 mm mesh is sufficient for capturing the deformation response under moderate impact velocities with minimal numerical error. However, at higher velocities, discrepancies of 25% or more between the 5 mm and 10 mm meshes suggest that additional refinement may still be required. The 2 mm mesh provides the most accurate results, showing the convergence of the deformation values for all tested velocities. Percent differences between the 5 mm and 2 mm meshes remain significant (ranging from 30% to 40%, depending on velocity), emphasizing that the 5 mm mesh, while reasonable, still overestimates deformation compared to the highly refined 2 mm mesh.

As the ball velocity increases, the differences between the coarse (10 mm) and refined (5 mm and 2 mm) meshes become more pronounced. This highlights the increasing importance of mesh refinement at higher impact velocities to capture the localized deformation and stress distributions accurately.

Additional calculations with different mesh sizes were performed for the particular velocity 6 m/s, and the results for deformations were received, shown in Table 3.4.

The table demonstrates that refining the mesh size improves the accuracy of the deformation results, with notable improvements observed when transitioning from coarse (5 mm) to moderately fine (2 mm) meshes. Smaller mesh sizes provide finer discretization, leading to more precise results. The 2 mm mesh provides a good compromise between accuracy and computational efficiency, as it captures most of the deformation obtained with the finest 1 mm mesh while requiring significantly fewer computational resources.

Table 3.4: Dependence of the results at a speed of 6 m/s on the model mesh size

FE mesh size (mm)	Number of nodes	u_{max} (mm)
5	17322	5.21
4	39793	3.95
3	69080	3.83
2.5	98814	3.78
2	206294	3.64
1.5	493677	3.58
1	1310812	3.54

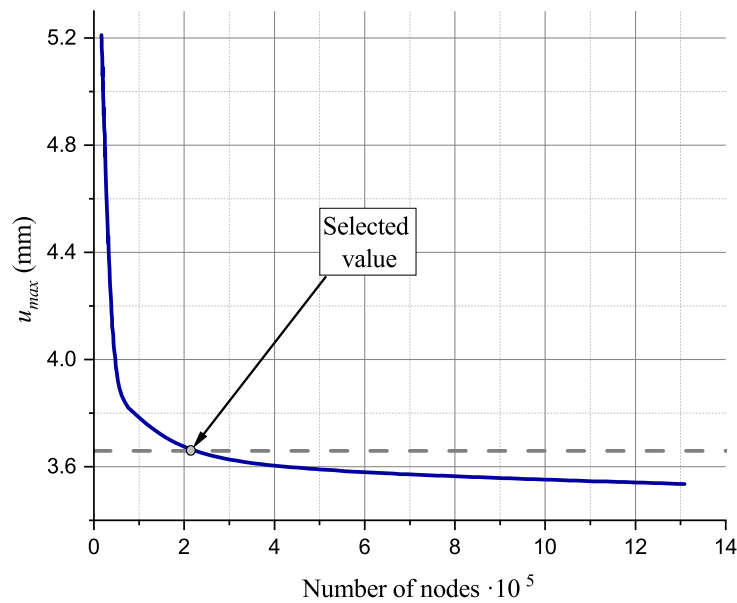


Figure 3.9: Dependence of the total displacements on mesh size

Similar estimation studies for the composite with the same size and conditions have been made in [91]. A comparison of the results shows good consistency with the results. The dependence of deformations on the mesh size (specified in the nodes) is shown in Figure 3.9, where the dashed line indicates the value in [91].

It can be seen that at first the accuracy between the bend values of the meshes, which have FE with dimensions of 5 mm and 4 mm, is quite large and constitutes 24%, but later it noticeably decreases to 3% between meshes of 4 mm and 3 mm, and between 2 mm and 1 mm it measures 2.8%.

In impact calculations for a flat plate, it is reasonable to use an element size of 2 elements per glass layer thickness (5 elements per LG thickness). This resolution is sufficient to accurately capture displacements and stresses while maintaining a relatively high computation speed without excessive runtime. In further tasks, we will consider models with a mesh size of 2 mm and adhere to this element size or use a slightly finer mesh if needed.

3.2 Analysis of the influence of geometric parameters on laminated glass dynamics

This section focuses on the LG plate, with its dimensions and material properties outlined in the previous section. The plate consists of two outer glass layers and a PVB interlayer, with the interlayer thickness (h_{int}) being a variable parameter in the analysis. The study examines the response of the LG plate to the impact of a steel ball under varying conditions, including different PVB interlayer thicknesses and ball drop velocities. This part of the work also considers the dynamic response of multilayer composites with different LG curvatures (c). By varying the curvature from flat to highly curved configurations, this part examines how the structural geometry of LG influences its ability to absorb and distribute impact forces. The analysis includes the maximum total displacements available. The FE mesh size was 2 mm. The chosen mesh size balances accuracy and computational efficiency, allowing for analyzing the LG plate's dynamic response.

The dynamic impact of a steel ball on LG with varying PVB interlayer thicknesses (h_{int}) and ball drop velocities (v_b) has been comprehensively analyzed to assess the mechanical response of the composite material. The study focused on maximum total displacements (u_{max}), first principal stresses (σ_1), and strains (ε_1) of the LG. Results were evaluated at two specific moments during the impact. t_1 corresponds to the time of maximum value of LG displacement, and t_2 to the time of maximum stress/strain experienced over the entire impact. The values of σ_1 and ε_1 are evaluated in the middle bottom center point, where the most extensive deformation occurs, and significant stress localization is observed. This point avoids the singularity of stress that naturally occurs where the laminate interacts directly with the perfectly rigid steel ball. By focusing on this location, the results represent accurate stress distribution without the influence of artificial stress concentrations. The values obtained from the calculation are shown in Table 3.5.

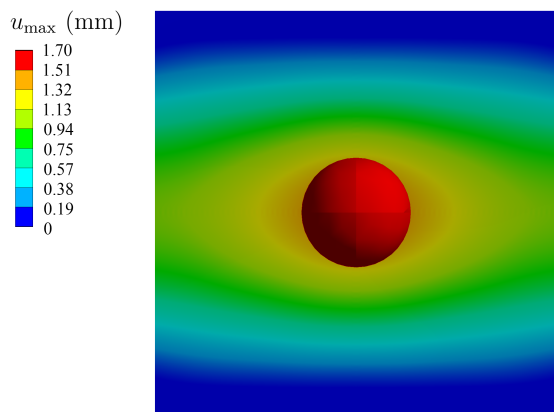


Figure 3.10: The magnitude of the displacement vector of LG with 0.38 mm PVB interlayer with the ball free-fall velocity 3 m/s

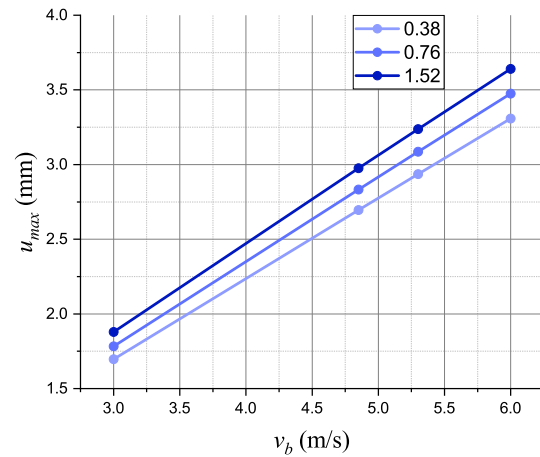


Figure 3.11: Dependence of u_{max} on v_b and h_{int}

Figure 3.10 presents the displacement distribution in LG with a 0.38 mm PVB interlayer subjected to the impact of a steel ball dropped at a velocity of 3 (m/s). As expected, the maximum

Table 3.5: Dependence of the results on interlayer size and ball velocity

h_{int} (mm)	v_b (m/s)	u_{max} (mm)	σ_1 (MPa) in t_1	σ_1 (MPa) in t_2	$\varepsilon_1 \cdot 10^{-3}$ in t_1	$\varepsilon_1 \cdot 10^{-3}$ in t_2
0.38	3	1.7	182.36	274.16	2.15	3.18
	4.85	2.7	334.7	451.87	3.95	5.26
	5.3	2.93	365.12	496.44	4.31	5.78
	6	3.31	412.77	565.94	4.88	6.6
0.76	3	1.78	205.13	255.94	2.4	2.92
	4.85	2.83	355.43	425.19	4.18	4.85
	5.3	3.09	388.58	466.49	4.57	5.32
	6	3.48	440.74	530.24	5.19	6.09
1.52	3	1.88	205.4	231.12	2.4	2.68
	4.85	2.98	345.29	382.43	4.06	4.45
	5.3	3.24	378.45	420.5	4.45	4.89
	6	3.64	430.22	479.83	5.06	5.59

displacement occurs in the impact zone, while the minimum displacement is observed along the fixed edges of the model. Similar displacement patterns are observed at higher velocities and interlayer thicknesses.

Figure 3.11 summarises the results of maximum displacements and shows the values within ball velocity and interlayer thickness. As the h_{int} increases, the u_{max} increases slightly (by approximately 5%) for the same v_b . This trend is consistent across all tested velocities. Thicker interlayers allow for somewhat higher flexibility in the LG system, resulting in more significant deformations than thinner interlayers. The differences in u_{max} between consecutive interlayer thicknesses 0.38 mm with 0.76 mm and 0.76 mm with 1.52 mm are consistent across all velocities, ranging between 4.5% and 5.1%. This indicates that the differences are relatively small, while interlayer thickness affects displacement. Maximum displacement increases with the ball velocity for all interlayer thicknesses. Higher velocities correspond to more impact energy, leading to more significant displacements. The thinner interlayers (0.38 mm) exhibit lower displacement values at all velocities than thicker interlayers, providing less flexibility in the composite structure. At higher velocities (6 m/s), the increase in displacement is more pronounced, but the overall percent differences between interlayer thicknesses remain consistent.

Figure 3.12 shows the first principal stress distribution in the bottom side of LG with a 0.38 mm PVB interlayer subjected to the impact of a steel ball dropped at a velocity of 3 (m/s). The maximum stress occurs on the center of the LG bottom side. Similar stress patterns are observed at higher velocities and interlayer thicknesses.

Figure 3.13 illustrates the relationship between the first principal stresses and the impact velocity of the steel ball for LG with varying PVB interlayer thicknesses. Across all interlayer thicknesses, the maximum principal stresses increase linearly with the steel ball's impact velocity. Increasing the PVB interlayer thickness significantly reduces the maximum principal stresses and strains for a given impact velocity. The thinnest interlayer (0.38 mm) results in the highest values, while the thickest interlayer (1.52 mm) shows the lowest values, highlighting the energy-absorbing capability of the thicker interlayers.

Considering the first principal elastic strains, the observed tendency aligns closely with the first

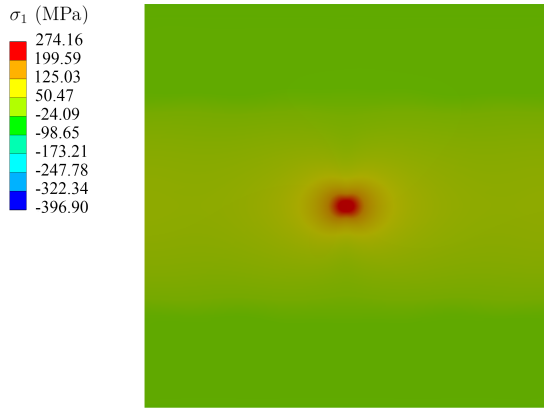


Figure 3.12: First principal stress of LG with 0.38 mm PVB interlayer with the ball free-fall velocity 3 m/s

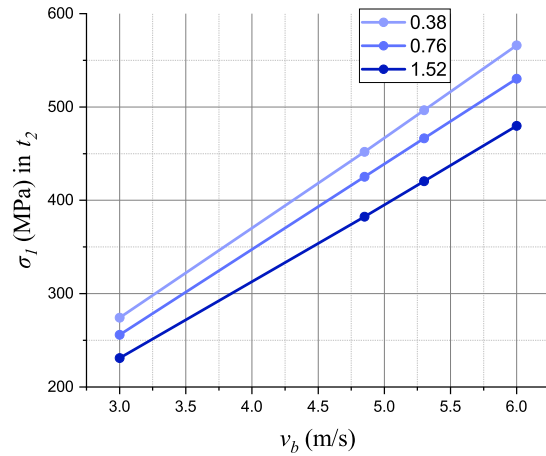


Figure 3.13: Dependence of σ_1 in t_{max} on v_b and h_{int}

principal stresses. The behavior within the PVB offers unique insights into the deformation mechanisms during the impact. Figure 3.14 highlights the strain distribution within the interlayer during the impact.

At the initial stages of impact, the strain is highly localized under the point of contact, reflecting the direct transfer of kinetic energy from the steel ball to the PVB layer. As the energy disperses, the strain propagates outward, forming concentric patterns that highlight the viscoelastic nature of the PVB interlayer. Unlike the glass layers, which exhibit a more brittle response, the PVB interlayer displays a viscous deformation behavior. This allows the strain to spread more uniformly across the interlayer, reducing the likelihood of catastrophic failure in the laminated structure. The localized strains suggest areas where energy absorption is most pronounced, contributing to the LG's overall impact resistance.

The observed strain distribution underscores the critical role of the PVB interlayer in absorbing and dissipating the energy from the impact. The viscoelastic behavior of the interlayer allows it to deform significantly, protecting the brittle glass layers from excessive stress concentrations.

These results demonstrate the combined effects of impact velocity and PVB interlayer thickness on LG's deformation behavior. Higher ball velocities lead to more significant deformation due to the increased impact energy, while thicker PVB interlayers provide additional flexibility, slightly expanding the deformation under the same loading conditions. Thicker interlayers are more effective at dissipating impact energy, leading to reduced stress on the glass surface and delaying potential failure. The linear trend in stress and strain for impact velocity suggests a predictable response of the glass under varying loading conditions, which is valuable for design optimization. Laminated glass with a thicker PVB interlayer is better suited for applications with expected high-impact velocities, offering improved structural integrity and safety.

Building on the analysis of the influence of ball velocity and PVB interlayer thickness on the behavior of LG, the study now transitions to investigating how the curvature of LG affects its dynamic response under impact loading.

The curvature parameter ranges from 0 mm (flat LG) to 152.5 mm (a curved cylindrical shell with

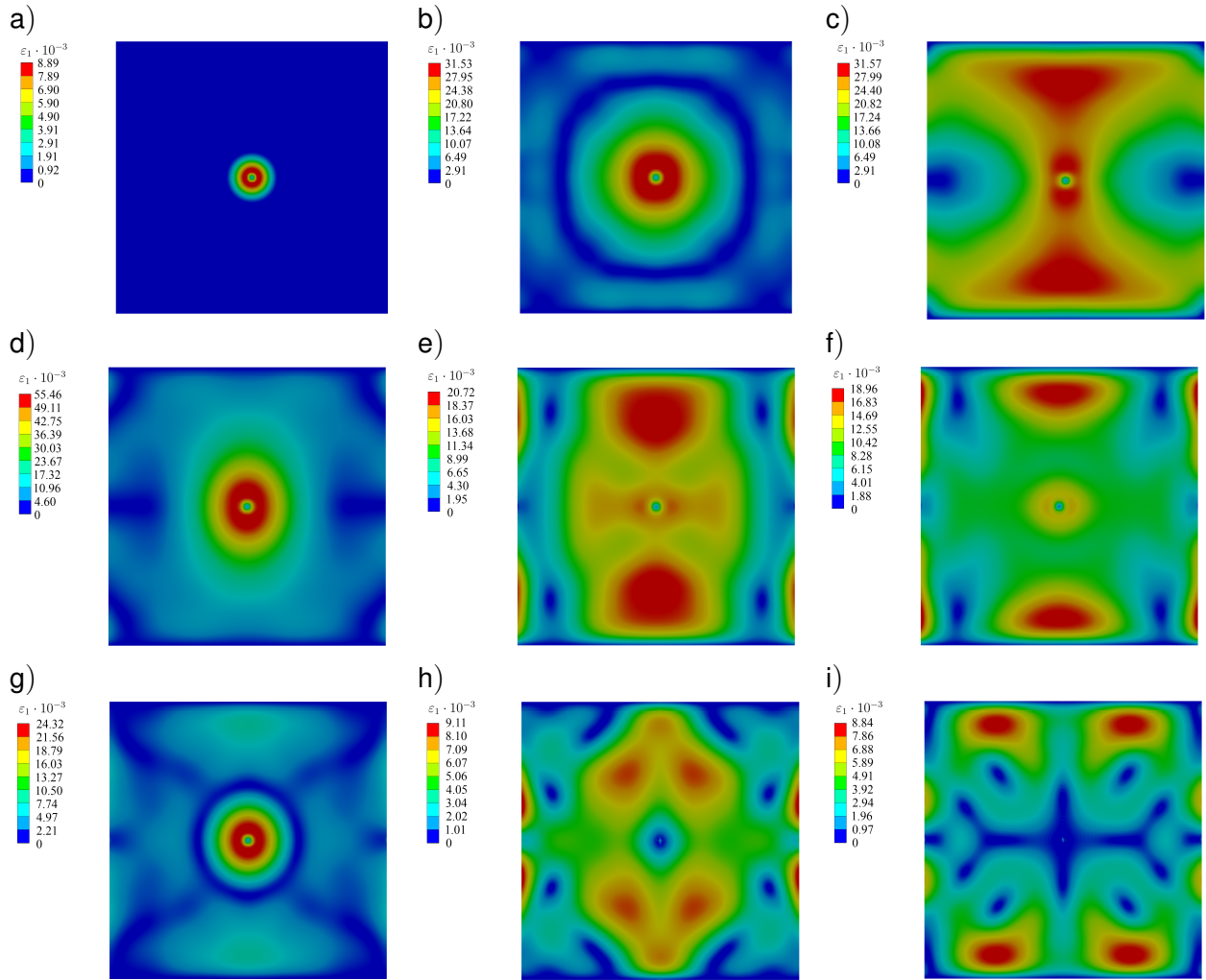


Figure 3.14: First principal strain of interlayer with 0.38 mm thickness with the ball free-fall velocity 3 m/s.

a) $t = 0.025$ ms, b) $t = 0.2$ ms, c) $t = 1.0$ ms, d) $t = 1.5$ ms, e) $t = 1.7$ ms, f) $t = 1.8$ ms, g) $t = 2.0$ ms, h) $t = 2.4$ ms, i) $t = 2.5$ ms

a radius equal to half the side length). The geometric models for the curved LG configurations are illustrated in Figure 3.15. The geometrical parameters of the LG and the ball, material properties (Table 3.2), boundary conditions, and task settings remain consistent with those described in the previous section. The laminate's two bottom sides were clamped to refine the curved LG's boundary conditions. The PVB interlayer thickness was chosen 1.52 mm, while the velocity of the impacting ball was varied to examine its influence on the laminate's dynamic response. As discussed previously, the FE mesh size was chosen as 2 mm.

Table 3.6 shows how the curvature parameter and the ball velocity influence the dynamic response. The results of the maximum magnitude of the displacement vector ($|u_{max}|$), first principal stress (σ_1), and first principal strain (ϵ_1) in the middle bottom center point at critical points in time were derived. These points correspond to the time of maximum value of LG displacement (t_1) and the time of maximum stress/strain experienced over the entire impact (t_2).

The increase in curvature leads to lower displacements under impact. From the flat LG to curved $c = 76.25$ mm, it is visible that the u_{max} reduces by approximately 45% for different velocities.

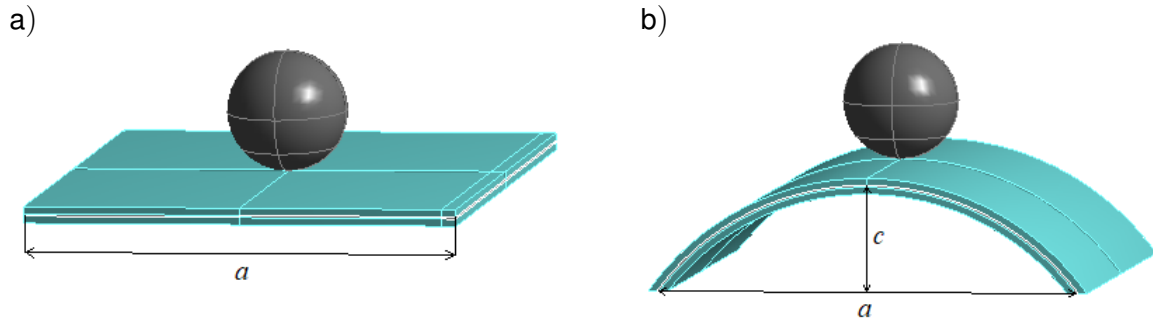


Figure 3.15: LG with different curvatures.

a) straight LG, b) curved LG

Then, the displacements are increasing by approximately 5%. The sharp reduction in u_{max} from flat LG to moderate curvature ($c = 76.25$ mm) highlights the benefits of curvature in improving structural stiffness and reducing deformation. However, at higher curvatures ($c = 152.5$ mm), localized deformation effects begin to counteract the benefits of curvature, leading to a modest increase in displacements. The reduction in displacement from flat to moderately curved LG is strongly connected to energy distribution across the structure. The slight increase at higher curvatures is due to localized energy concentration near the impact zone. Optimizing the curvature ensures effective energy absorption and redistribution, balancing structural rigidity with impact resistance. At all curvatures, the displacement increases with higher ball velocities. Curved configurations reduce the effects of high velocities. This demonstrates the effectiveness of curvature in reducing deformation under high-energy impacts.

The distribution of σ_1 reveals that the maximum stress values are concentrated at the center of the plate. As the elastic wave propagates, stress magnitudes spread outward from the impact area. For curvature parameters from 0 till 40 mm, the stresses increase by approximately 30%. After this point, the curvature significantly affects the propagation of elastic waves, altering the stress distribution patterns. The stresses decrease till $c = 152.5$ mm by approximately 30%. The interaction of the propagating elastic wave with the curved geometry leads to a redistribution of stresses. This reduction can be attributed to the dispersion of wave energy over the larger curved surface, which mitigates the concentration of stresses in any single region. The stress increases with higher ball velocities at all curvatures. As the ball velocity increases, the dynamic forces acting on the LG intensify, leading to higher stress concentrations at the point of impact and in the surrounding areas. Curved configurations reduce the effects of high velocities. As curvature increases, the stress concentration at the impact zone is distributed more effectively over the surface. This dispersion reduces the intensity of localized stress peaks, making the LG less susceptible to damage under high-velocity impacts.

Additional calculations were done with different mesh sizes (1.5 mm, 2 mm, 2.5 mm) for a velocity of 3 m/s of the ball fall. A fitting analysis of the data was performed to analyze the dependence of the displacements and first principal stresses on the curvature parameter.

The maximum displacement is approximated by an exponential function

$$u_{max} = y_0 + S_0 \exp(R_0 c), \quad (3.11)$$

where y_0 is the offset, S_0 is the initial value and R_0 is the rate.

Table 3.6: Dependence of the results on interlayer size and ball velocity

c (mm)	v_b (m/s)	u_{max} (mm)	σ_1 (MPa) in t_1	σ_1 (MPa) in t_2	$\varepsilon_1 \cdot 10^{-3}$ in t_1	$\varepsilon_1 \cdot 10^{-3}$ in t_2
0 (straight)	3	1.88	214.28	240.17	3.77	4.22
	4.85	2.98	360.96	398.85	6.34	7.01
	5.3	3.24	395.51	438.48	6.95	7.71
	6	3.64	449.52	500.01	7.9	8.79
19.06 ($a/16$)	3	1.29	299.98	305.72	5.27	5.37
	4.85	2.08	494.5	502.58	8.69	8.83
	5.3	2.28	539.55	550.38	9.48	9.67
	6	2.59	608.72	623.92	10.7	10.96
23.8 ($a/13$)	3	1.22	301.43	312.5	5.3	5.49
	4.85	1.96	496.13	510.01	8.72	8.96
	5.3	2.16	541.49	557.25	9.52	9.79
	6	2.45	615.9	635.95	10.82	11.18
28.6 ($3a/32$)	3	1.18	309.31	317.98	5.44	5.59
	4.85	1.9	498.78	520.05	8.76	9.14
	5.3	2.08	559.38	570.12	9.83	10.02
	6	2.36	626.09	650.24	11.01	11.43
38.13 ($a/8$)	3	1.1	290.82	294.53	5.11	5.18
	4.85	1.77	480.99	481.33	8.45	8.46
	5.3	1.93	528.41	528.41	9.29	9.29
	6	2.2	601.07	601.07	10.56	10.56
57.2 ($3a/16$)	3	1.03	280.5	294.28	4.93	5.17
	4.85	1.65	451.96	485.63	7.94	8.53
	5.3	1.83	496.73	532.87	8.73	9.36
	6	2.08	559.7	601.42	9.84	10.57
76.25 ($a/4$)	3	0.99	286.54	303.66	5.04	5.34
	4.85	1.63	451.57	494.92	7.94	8.7
	5.3	1.78	494.41	542.8	8.69	9.54
	6	2.03	561.57	616.37	9.87	10.83
114.4 ($3a/8$)	3	1.02	210.43	262.25	3.7	4.61
	4.85	1.65	352.15	420.84	6.19	7.4
	5.3	1.81	366.22	461.93	6.44	8.12
	6	2.06	418.07	525.45	7.35	9.23
152.5 ($a/2$)	3	1.06	150.04	212.59	2.64	3.74
	4.85	1.71	239.75	349.89	4.21	6.15
	5.3	1.87	258.59	383.46	4.54	6.74
	6	2.12	294.76	434.61	5.18	7.64

The first principal stress data were approximated by a cubic polynomial function

$$\sigma_1 = A_0 + A_1 c + A_2 c^2 + A_3 c^3, \quad (3.12)$$

where A_0 is the offset, and A_1 , A_2 , A_3 are coefficients.

The values of the regression parameters are shown in Table 3.7.

Table 3.7: Regression parameters

y_0 (mm)	S (mm)	R_0 (1/mm)	A_0 (MPa)	A_1 (MPa/mm)	A_2 (MPa/mm ²)	A_3 (MPa/mm ³)
1.049	0.922	-0.095	245.47	3.223	-0.045	$1.435 \cdot 10^{-4}$

The maximum displacements decrease with increasing the curvature parameter, but it can increase slightly with a high curvature parameter (Figure 3.16). The maximum stresses increase with increasing the curvature parameter till 30 mm, and then it decreases (Figure 3.17).

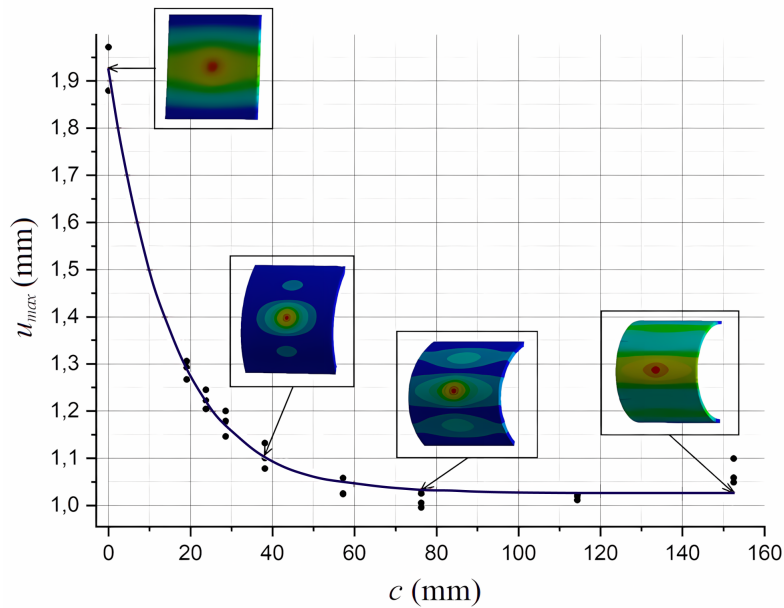


Figure 3.16: Dependence of maximum displacement on the curvature parameter with the ball velocity 3 m/s

The distribution of equivalent strain (ε_{eq} is defined as the largest of the absolute values of $|\varepsilon_1 - \varepsilon_2|$, $|\varepsilon_2 - \varepsilon_3|$, $|\varepsilon_3 - \varepsilon_1|$), particularly within the PVB interlayer, provides insights into LG deformation behavior under impact loading. The strain localization and propagation are heavily influenced by both the impact force and the curvature parameter of the LG. Figure 3.18 visually demonstrates strain distribution patterns, emphasizing how curvature modifies strain propagation in LG systems under impact loading.

The maximum equivalent strain values are observed in the impact zone, where the applied force from the ball results in significant deformation. The edges of the LG model, where constraints or supports are applied, exhibit the lowest strain values. The presence of the PVB interlayer ensures strain localization in the impact zone while increasing curvature promotes strain redistribution. These findings suggest that curved laminated glass configurations can enhance impact resistance by reducing strain localization and promoting better energy absorption.

The analysis of impact loading on LG with varying curvatures reveals significant dependencies on geometry. The displacement, stress and strain distributions emphasize the role of curvature

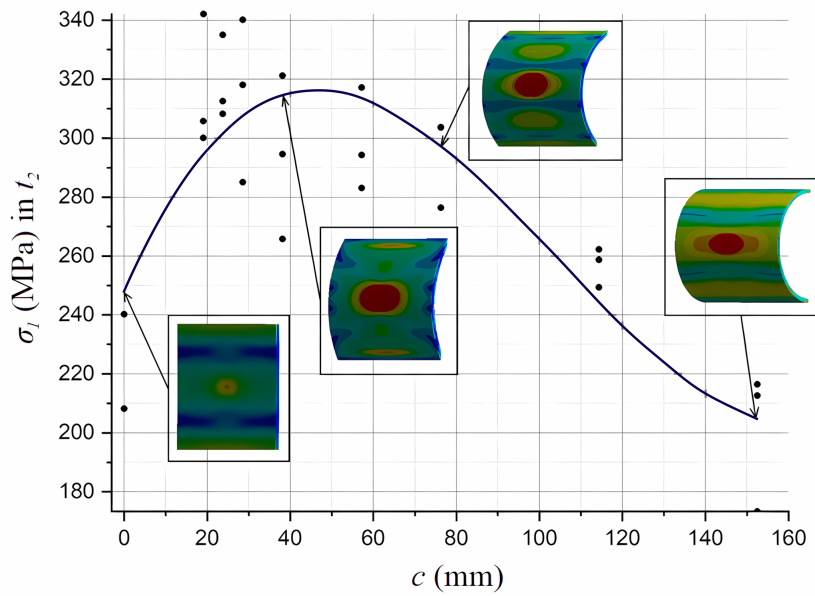


Figure 3.17: Dependence of first principal stress on the curvature parameter with the ball velocity 3 m/s

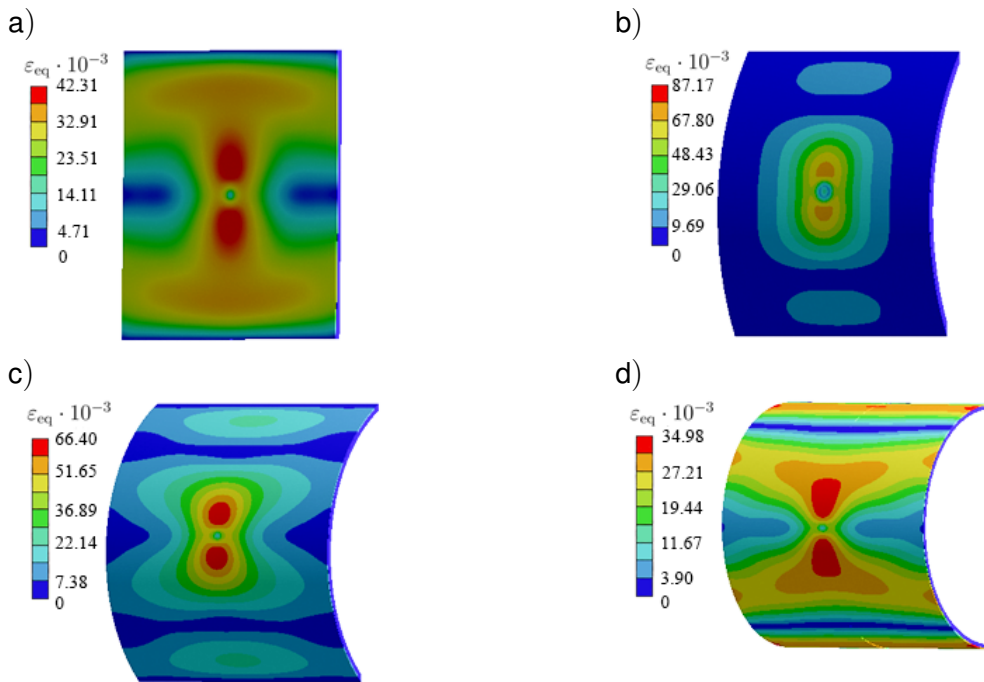


Figure 3.18: Equivalent strain in PVB interlayer with the ball velocity 3 m/s.
a) $c = 0$ mm, b) $c = 38$ mm, c) $c = 76$ mm, d) $c = 152.5$ mm

in modifying the structural response. The results provide valuable insights for designing curved laminated glass structures in applications with critical impact resistance. This analysis highlights the importance of selecting the correct curvature for specific design applications, balancing energy absorption, deformation control, and structural rigidity.

3.3 Linear dynamic properties in curved laminated glasses

Building on the previous analysis of the dynamic response of LG with varying curvatures under impact loading, this section shifts focus to the linear dynamics of LG composites. The goal is to evaluate the linear characteristics of LG by investigating its natural frequencies and normal modes. These characteristics are critical for understanding how elastic waves propagate through the structure in a linear state, providing insights into its dynamic stability and vibrational behavior.

The task is to conduct a series of theoretical studies examining curvature's effect on LG's natural frequencies and vibration modes. This includes identifying how changes in the curvature parameter influence the vibrational behavior and elastic wave distribution across the composite structure.

The laminate stays as a combination of two skin glass layers and one interlayer. However, the model parameters are changed. We take a glass of thickness 3 mm each with a PVB interlayer of 0.38 mm thicknesses. The width and length of the plate are 500 mm each. The curvature parameter has been varying from 0 mm to 250 mm (from flat LG up to the curved as a cylindrical shell with a radius equal to half the side length).

The material properties of the glass and interlayers are taken from Table 3.2. The behavior of laminated glass samples with PVB interlayer was modeled by modal analysis in 3D modeling and a FEM. Hexagonal FE with 8 nodes with 3 degrees of freedom in each was used [101]. As boundary conditions, laminate was fixed on two opposite sides. The geometric models with FE mesh are shown in Figure 3.19.

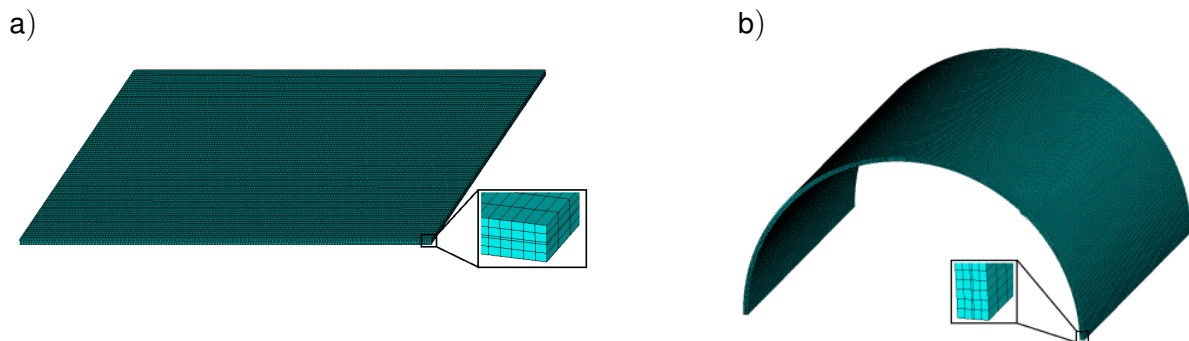


Figure 3.19: LG with different curvatures.
a) straight LG, b) curved LG

To further investigate the linear dynamics of laminated glass with varying curvatures, the FE model developed earlier is now used for mode-frequency analysis. This step involves examining the natural vibration characteristics of the LG composite with different curvatures, including its natural frequencies and corresponding mode shapes. These dynamic properties are important for understanding how the structure responds to vibrational excitations in its linear state and how curvature influences its vibrational behavior.

To achieve this, the analysis requires solving the eigenvalue and eigenvector problem, which determines the natural frequencies (eigenvalues) and the associated vibration modes (eigenvectors) of the system. This problem is fundamental in structural dynamics as it reveals the inherent vibrational characteristics of the laminated composite.

For the analyzed flat LG, FE meshes with varying element sizes were generated to evaluate the computational accuracy. Frequency calculations were performed for each mesh size to deter-

mine the associated computational error. Ultimately, a mesh size of 2 mm was selected for the analysis. The error between frequency values obtained with 2 mm and 1 mm meshes was found to be less than 2%, indicating that the 2 mm mesh provides sufficient accuracy while maintaining computational efficiency.

Table 3.8: Dependence of laminated glass mode frequency on curvature

c (mm)	p_1	p_2	p_3	p_4	p_5	p_6 (Hz)	p_7	p_8	p_9	p_{10}
0	139.6	165.6	279.3	369.3	404.4	523.5	527.8	691.7	727.9	750.4
31.25	387.8	506.2	577.1	599.7	727.5	738.5	886.9	904.5	917.9	979.6
39.06	372.7	530.8	600.9	629.9	791.5	823.8	994.9	1005.6	1048.8	1059.8
46.88	361	560.4	602.3	633.7	857.12	869.9	1085	1117	1125.2	1145.7
62.5	338.3	584.5	616.4	621.4	928.8	967.1	1029.1	1135.2	1286	1291.4
93.75	295.9	534.3	562.6	698.2	934.3	1039.2	1065.6	1153	1288.9	1312.1
125	249.9	467.5	490.9	680.6	818.3	1084.6	1113.6	1155.6	1176.3	1191
187.5	165.8	334.1	347.4	535.1	593.5	863.6	879.1	1100.8	1108.2	1112.9
250	109.7	235.6	240.7	397.8	426.5	635.6	647.3	861.2	892.1	1079.6

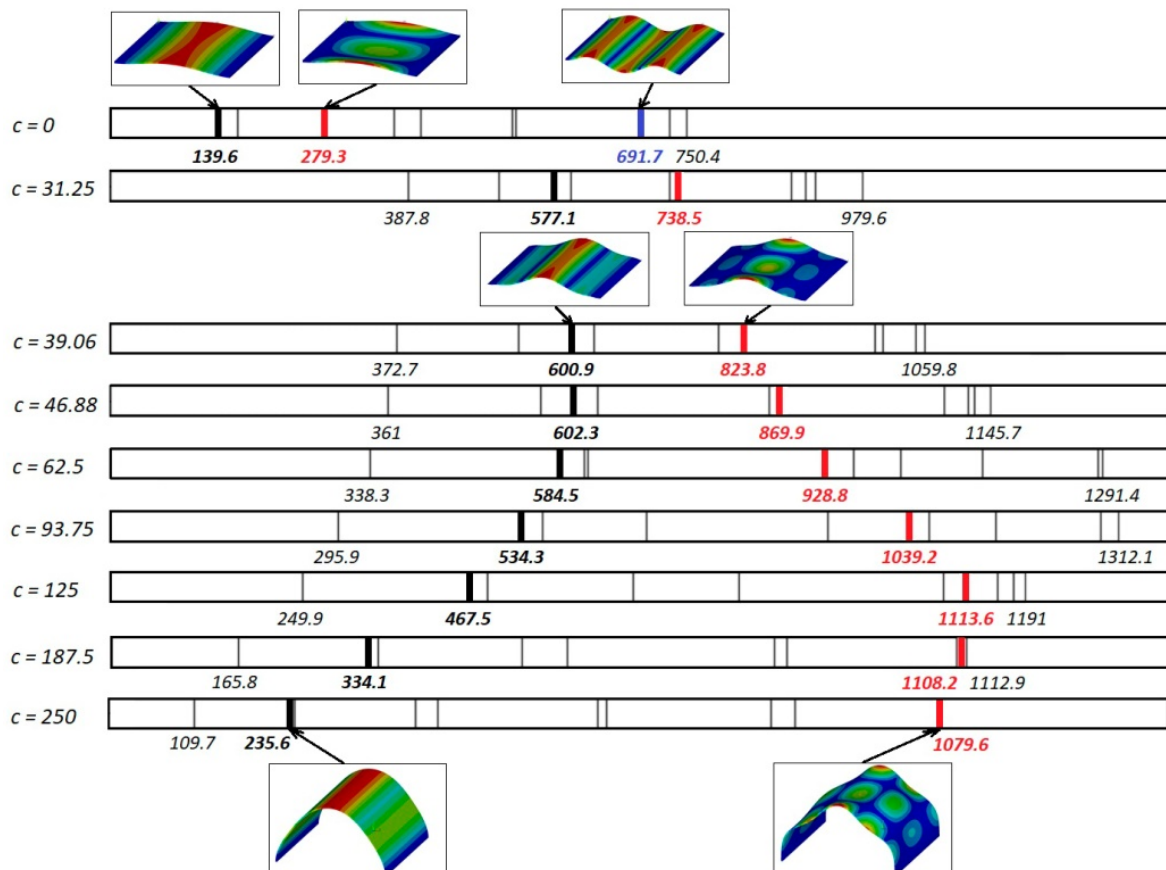


Figure 3.20: Laminated glass mode frequency

Modal analysis was carried out for laminated glasses with different curvatures. The eigenfrequencies ($p_1 - p_{10}$) (Table 3.8) and vibration modes of the composites were obtained.

Figure 3.20 illustrates the natural vibration modes that may occur during dynamic analysis.

As the curvature of the LG increases to a value of 46.88 mm, the first eigen frequency rises significantly from 139.6 Hz to 602.3 Hz. However, beyond this point, the first eigen frequency decreases to 235.6 Hz as curvature increases (as highlighted in black). This behavior demonstrates how the structural stiffness of the laminated glass initially increases with curvature, enhancing its vibrational properties, but eventually declines as the curvature reaches higher values. The distribution of the corresponding wave across the plate can be observed in Figure 3.20, where the deformation patterns illustrate the interaction of the elastic wave with the composite structure.

Similarly, the second eigen frequency of the flat LG begins at 279.3 Hz and increases steadily to 1113.6 Hz as the curvature reaches 125 mm (highlighted in red). This trend reflects the continued stiffening effect of curvature on the higher-order vibrational modes. The elastic wave associated with this frequency is distributed across the laminated glass, and its distinct mode shape is also visualized in Figure 3.20.

These results highlight the complex influence of curvature on the vibrational characteristics of laminated glass, where the natural frequencies and corresponding elastic wave distributions are strongly affected by the structural geometry. The findings provide valuable insights into optimizing curvature for specific vibrational and dynamic performance requirements.

3.4 Deformation of laminated composite panels with different glass curvatures under impact loading

The dynamic response of laminated multilayer glass composites with varying levels of curvature arising from the impact of a steel ball is performed with different boundary conditions to examine the dependence of dynamic deformation levels in the composite on the impact conditions.

The composite consists of two glass plates, each 3 mm thick, with a PVB interlayer of 0.38 mm thickness in between. The plate has length and width $a = 500$ mm, with curvature parameter $c = 0 \dots 250$ mm. A curved composite was analyzed and subjected to impact loading through contact with a smooth steel ball with a diameter of 63.5 mm (1 kg) at a velocity of 8 m/s. The geometric models of composites with varying levels of curvature are presented in Figure 3.21. The flat laminate is a special curved glass case with a zero curvature parameter ($c = 0$ mm), as shown in Figure 3.21 a). An example of a curved laminate ($c = 125$ mm) is shown in Figure 3.21 b).

The material properties of the glass, interlayers, and ball stays and shown in Table 3.2. The impact behavior of LG with a PVB interlayer was modeled using transient analysis within the framework of 3D modeling and an explicit dynamic approach based on the FEM. A hexahedral finite element with 8 nodes and 3 degrees of freedom per node was used.

As boundary conditions, the laminate was fixed on two opposite sides along the curvature, and the ball impact was modeled at the center of the plate, as shown in Figure 3.22. The composite was modeled using a physically linear elastic formulation in a three-dimensional framework. The interaction between the ball and the composite was handled within the framework of a one-sided contact problem using the "surface-to-surface" algorithm. The resistance provided by air during the impact was neglected.

For the analyzed flat model, FE meshes with elements of varying sizes were created. For each mesh size, maximum displacements were calculated to determine the computational error. The

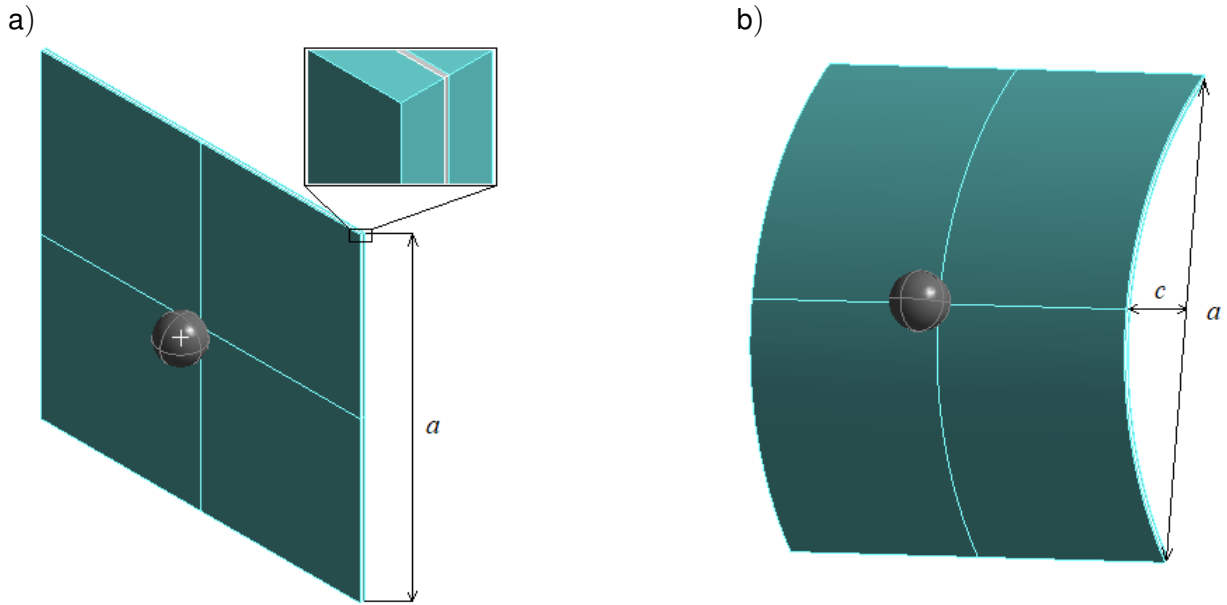


Figure 3.21: LG with different curvatures.
a) straight LG, b) curved LG

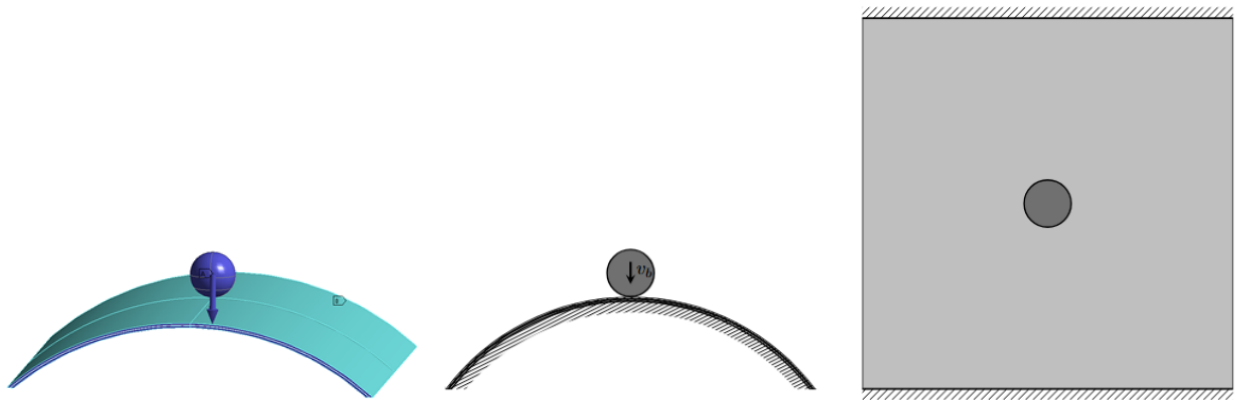


Figure 3.22: LG boundary conditions

optimal mesh size of 2 mm was determined.

This analysis focused on understanding how curvature and boundary conditions influence the mechanical response of laminated glass, particularly in terms of its deformation under dynamic loading conditions. Key results included the evaluation of maximum displacements (u_{max}), providing insights into the relationship between curvature and the structural flexibility or stiffness of the composite. The computed values of maximum displacements were obtained for different curvature parameters and summarized in Table 3.9. Figure 3.23 shows the displacement that arises in LG with different curvatures under the impact loading.

Increasing the curvature of laminated glass significantly reduces maximum displacement. This suggests that adding curvature improves the stiffness and impact resistance of the laminate. The lowest displacement value is observed at $c = 250$ mm; this represents a 48.9% reduction compared to the flat laminated glass, demonstrating the stiffening effect of higher curvature. The graph of Table 3.9 is shown in Figure 3.24. In comparison with previous results, where the plates

Table 3.9: Calculation results

c (mm)	u_{max} (mm)
0	6.53
31.25	4.94
39.06	4.73
46.88	4.42
62.5	4.06
93.75	3.65
125	3.55
187.5	3.37
250	3.34

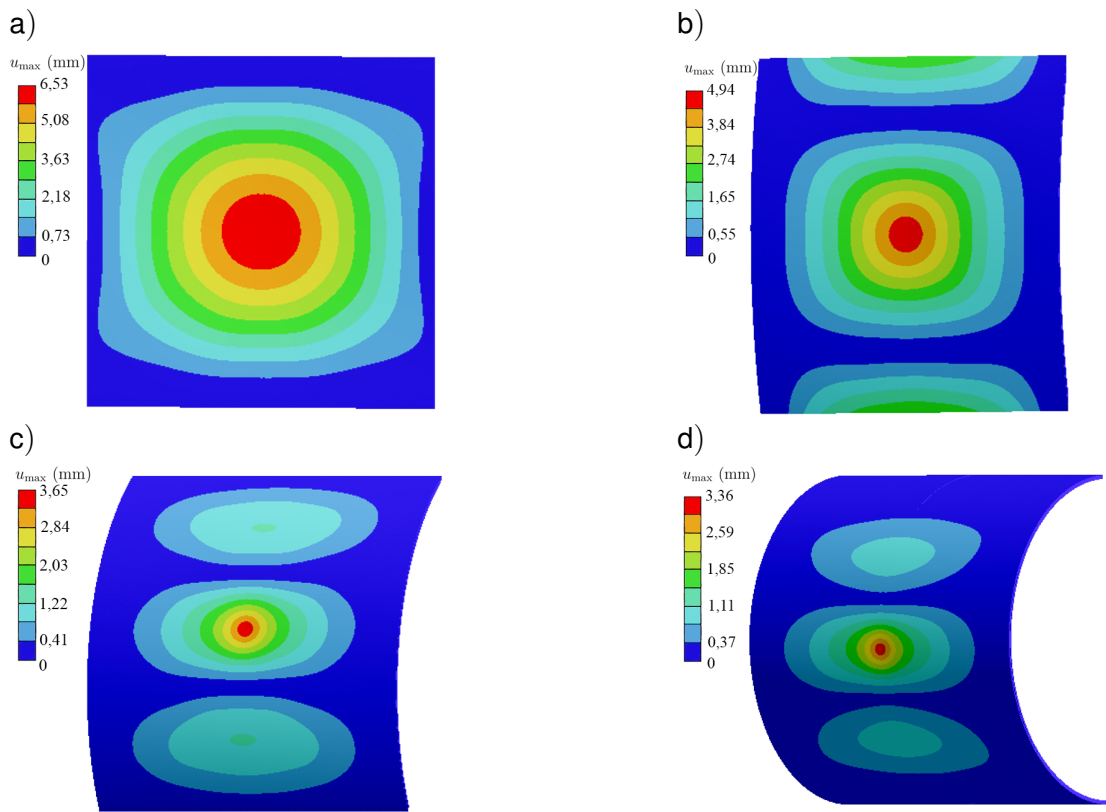


Figure 3.23: Magnitude of the displacement vector in LG with the ball velocity 8 m/s.

a) $c = 0$ mm, b) $c = 31$ mm, c) $c = 94$ mm, d) $c = 250$ mm

were fixed differently and smaller, displacement was observed after a certain angle. Still, in this case, no increase in displacement was observed.

The maximum magnitude of the displacement vector is observed in the center of the impact zone, and the minimum displacement is at the edges of the model. A distribution of the elastic wave has been considered. With a curvature parameter increasing, the distribution of the maximum magnitude of the displacement vector is traced along the LG.

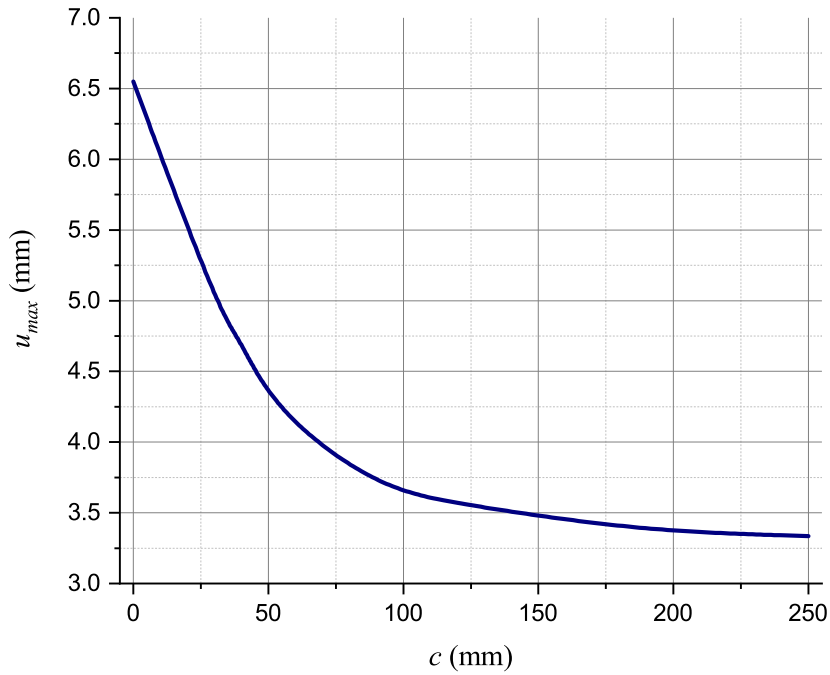


Figure 3.24: Dependence of maximum displacements in LG on the curvature parameter

3.5 Influence of interlayer elasticity on laminated glass dynamics

This section investigates the influence of PVB interlayer on LG dynamic behavior. A hit on a composite plate with a solid steel ball of mass 1 kg with an initial velocity of 8 m/s is considered. The square plate of size 500 mm consisted of two layers of glass with a thickness of 3 mm and one interlayer with a thickness of 0.36 mm. The impact of the ball was simulated in the center of the plate. As boundary conditions, the glass is supported on all sides.

The steel and glass material properties are pointed out in Table 3.2. The interlayer material properties with density $\rho = 960 \text{ kg/m}^3$, and Poisson ratio $\nu = 0.45$ were used. The elasticity modulus varies between 7 MPa and 70000 MPa.

The impact of the ball on the glass plate is analyzed using the explicit approach in the framework of three-dimensional modeling by FEM. Linear FE with 8 nodes and 3 degrees of freedom are used. The surface-to-surface algorithm considers the ball and plate interaction a one-way contact. The resistance caused by air during impact is neglected. The time step size is $3 \cdot 10^{-5} \text{ s}$. The FE mesh with a 2 mm element size is selected for the simulation model. The mesh is presented in Fig. 3.25.

To realistically simulate free support in the model, a frame with a dimension of 10 mm was created along the perimeter edges of the plate's bottom surface. The nodes on the frame were selected and constrained in their displacements within the y -plane.

Transient analysis was performed to study the impact of a steel ball on the composite plate. A nonlinear formulation was applied to capture the behavior of the system accurately. The analysis

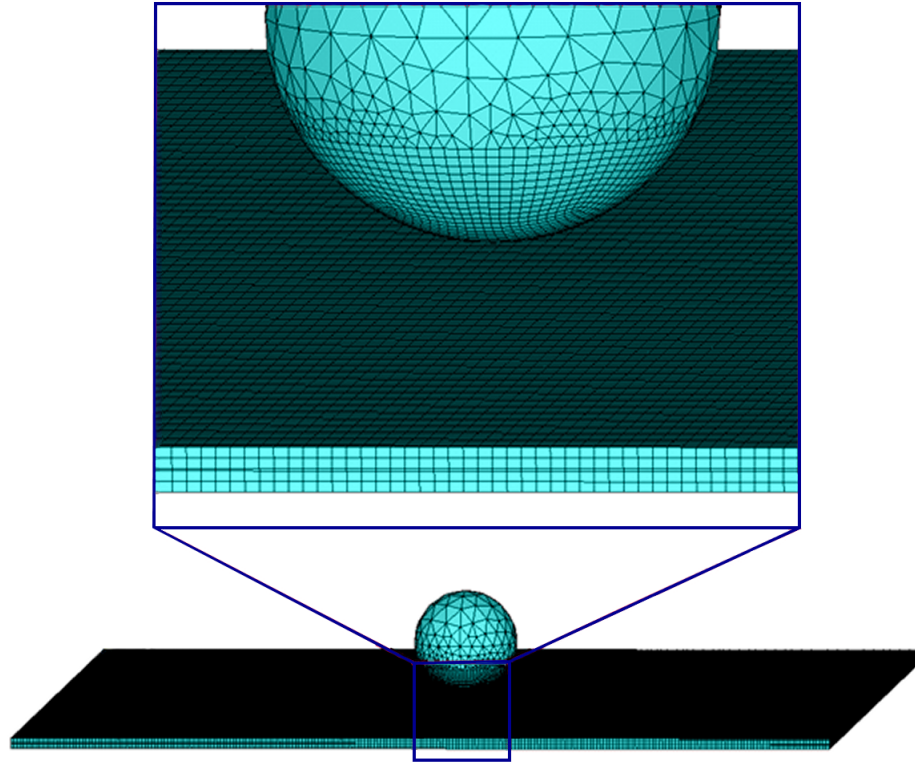


Figure 3.25: FE mesh of the model

provided results for the maximum displacement (u_{max}) of the ball, the plate, and the first principal stress (σ_1) in the plate.

Figures 3.26 and 3.27 illustrate u_{max} of the ball's bottom node and the plate's top center node, as well as the time-dependent variation of the plate's σ_1 at the bottom center node, for an interlayer $E = 7$ MPa. During the first interaction between the ball and the plate, from the initial moment to approximately $t = 0.002$ s, the first stress peak occurs, reaching around 300 MPa. Following this, the ball temporarily separates from the plate. During the second interaction, between $t = 0.003$ s and $t = 0.0045$ s, the second stress peak is observed, reaching a value of approximately 475 MPa.

Figure 3.28 illustrates the relation between the maximum displacement at the bottom center node of the plate and Young's modulus of the interlayer. The results show that as the modulus increases, the maximum displacement decreases, indicating greater stiffness in the interlayer. Figure 3.29 shows the dependence of the first and second peaks of the plate's maximum first principal stresses at the bottom center node on the interlayer Young's modulus. The results indicate that as the modulus increases, the stress peaks also increase but eventually stabilize, reflecting the interplay between material stiffness and stress distribution in the plate.

Table 3.10 provides a detailed summary of the displacements, first principal stresses, and strains at various time points during the interaction between the steel ball and the laminated composite plate. The data highlights the dynamic behavior of the composite as elastic waves propagate through its structure.

The maximum displacements occur at the center of the plate, where the ball impacts the composite. This is expected as the central area directly absorbs the impact energy, causing localized deformation. As time progresses, the displacement values decrease as the elastic waves spread

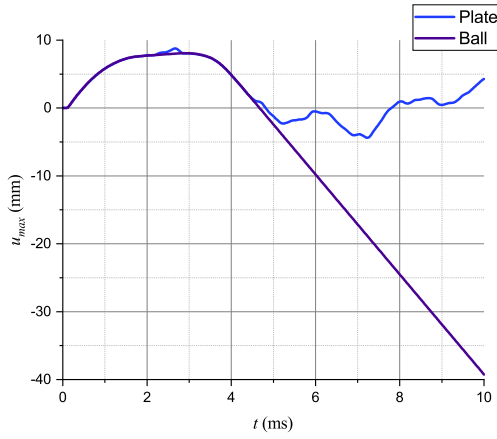


Figure 3.26: Dependence of u_{max} of ball bottom and plate top center node on time

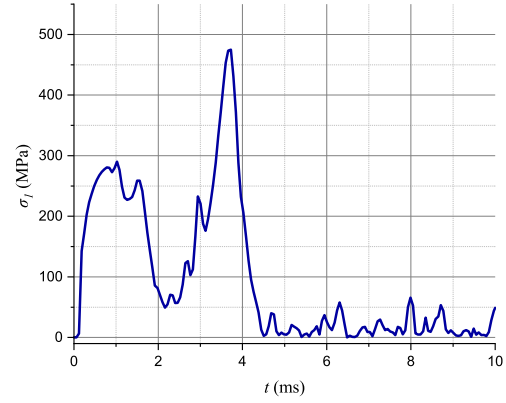


Figure 3.27: Dependence of σ_1 of plate bottom center node on time

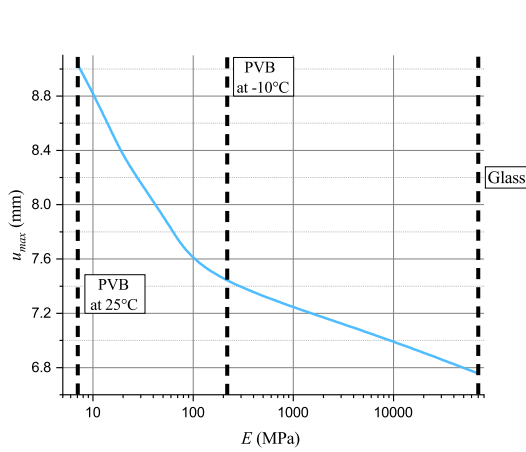


Figure 3.28: Dependence of u_{max} of plate bottom center node on Young's modulus of interlayer

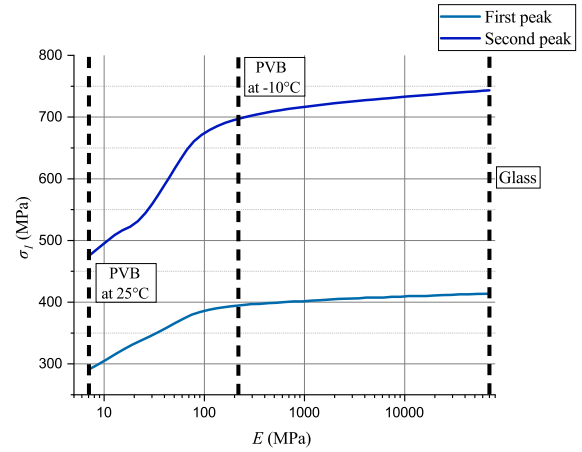


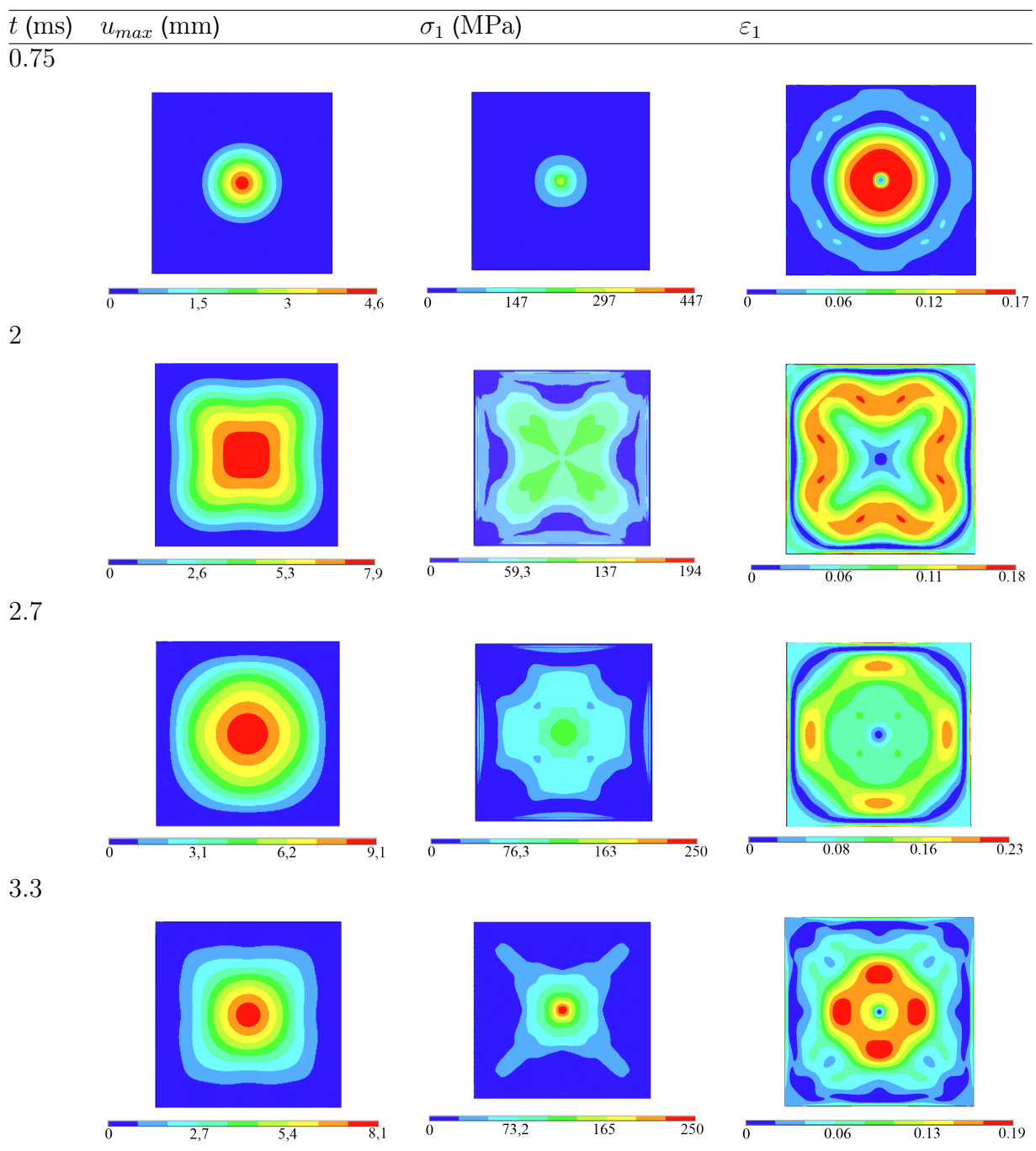
Figure 3.29: Dependence of first and second peak of σ_1 of plate bottom center node on Young's modulus of interlayer

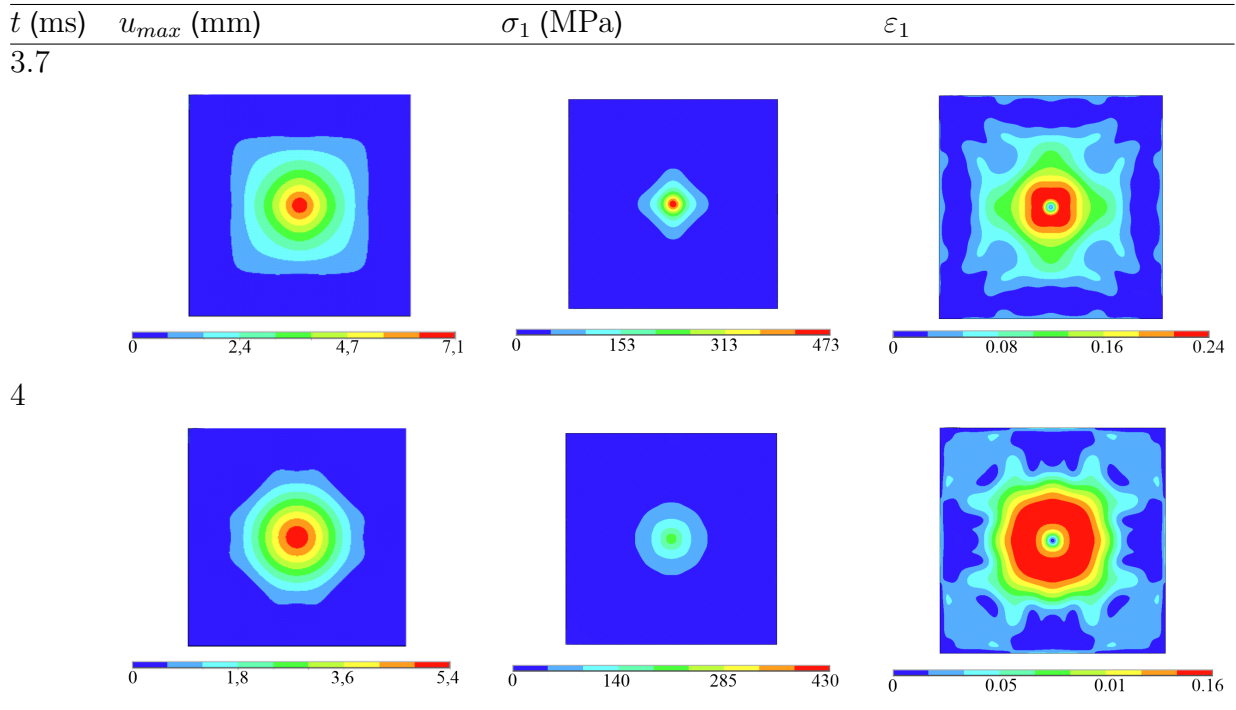
outward from the impact zone, redistributing the power across the plate.

The first principal stresses are evaluated at the bottom layer of the plate. The stress patterns form cruciform shapes, radiating outward from the impact point. These stress patterns reflect the directional distribution of forces across the plate. The bottom layer experiences significant stress concentrations due to its proximity to the impact zone and the rigid boundary conditions.

The strains are evaluated within the interlayer (PVB), which plays a critical role in the overall dynamic behavior of the laminate. The interlayer is energy-absorbing, accommodating the shear and tensile forces generated during the impact. The maximum strains are observed along the edges of the plate when the ball is in contact with the laminate. This occurs because the edges experience higher deformation due to the boundary conditions, causing the interlayer to stretch and deform to redistribute the impact forces.

Table 3.10: Displacement, first principal stress, and first principal strain at different time points





The interlayer's properties enable it to mitigate the effects of the impact, ensuring that the deformation remains controlled and localized.

The results also demonstrate how elastic waves travel through the composite structure. The waves originate at the center and spread through the plate upon impact. The combination of displacements, stresses, and strains creates a complex interaction within the laminate, highlighting the importance of each layer's mechanical properties in determining the overall dynamic response.

Figures 3.30 and 3.31 show the dependences of displacements and 1st principal stresses of the bottom center plate node on time with different Young's modulus of the interlayer.

The results show that as Young's modulus of the interlayer increases, the maximum displacement at the bottom center node systematically decreases. With each incremental increase in the modulus, the displacement peaks reduce by approximately 10%. This reduction in displacement indicates that a stiffer interlayer enhances the structural rigidity of the composite, thereby restricting deformation. At the same time, the duration of contact between the ball and the plate is reduced as the interlayer becomes stiffer. This behavior reflects the ability of the interlayer to resist deformation more effectively, absorbing and redistributing impact energy more efficiently, which causes the ball to rebound more quickly.

In contrast, the first principal stresses at the bottom center node exhibit the opposite trend, increasing with each step increase in the interlayer's Young's modulus. The stress peaks rise by approximately 10% with each increment in stiffness, indicating that stiffer interlayers transfer more stress to the outer layers of the laminate as they resist deformation. Additionally, the contact duration for stress peaks decreases as the modulus increases, highlighting the reduced time over which the plate experiences significant stress as it recovers more rapidly after impact.

These results reveal a clear trade-off between displacements and stresses in the laminate. Softer interlayers with lower Young's modulus redistribute more impact energy, resulting in higher displacements but lower stress levels as the power is dissipated through more significant deformation within the interlayer. Conversely, stiffer interlayers with higher Young's modulus reduce deformation but transfer greater stress concentrations to the laminate's outer layers.

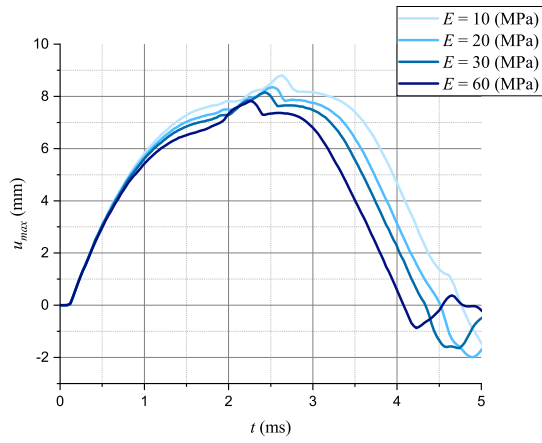


Figure 3.30: Maximum displacement at the bottom central point of the plate vs time for different values of Young's modulus of the interlayer

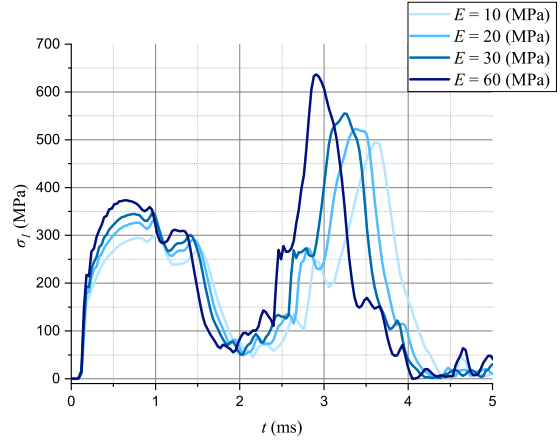


Figure 3.31: First principal stress at the bottom central point of the plate vs time for different values of Young's modulus of the interlayer

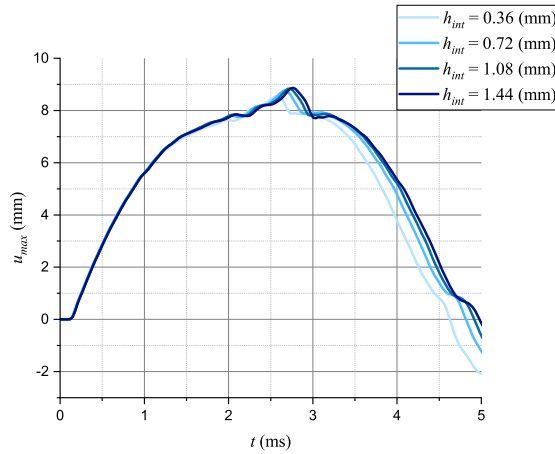


Figure 3.32: Maximum displacement at the bottom central point of the plate vs time for different interlayer thickness values

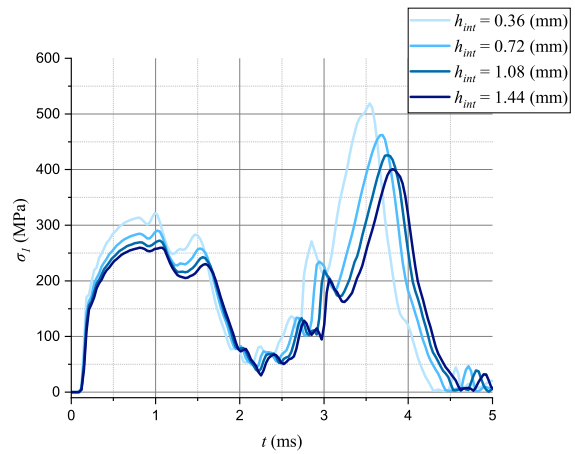


Figure 3.33: First principal stress at the bottom central point of the plate vs time for different interlayer thickness values

The next step was to set $E = 15$ MPa. To investigate the influence of interlayer thickness on the dynamic behavior of the laminated glass composite, interlayers with varying thicknesses of 0.36 mm, 0.72 mm, 1.08 mm and 1.44 mm were used.

Figures 3.32 and 3.33 illustrate the time-dependent behavior of u and σ_1 at the bottom center node of the plate for interlayers with varying thicknesses. The analysis reveals that as the thickness of the interlayer increases, the maximum displacements at the bottom center node also increase slightly. A longer contact duration between the ball and the plate accompanies this. Thicker interlayers absorb and dissipate more impact energy due to their greater flexibility, allowing for more pronounced deformation and prolonging the interaction time between the ball and the plate. In contrast, the first principal stress peaks decrease as the interlayer thickness

increases. The results show that with each step increase in thickness, the stress peaks are reduced by approximately 15%. Thicker interlayers distribute the impact forces more effectively across the composite, reducing the plate's stress concentrations. This ability to lower stress peaks highlights the role of thicker interlayers in mitigating localized damage and protecting the structural integrity of the laminated composite.

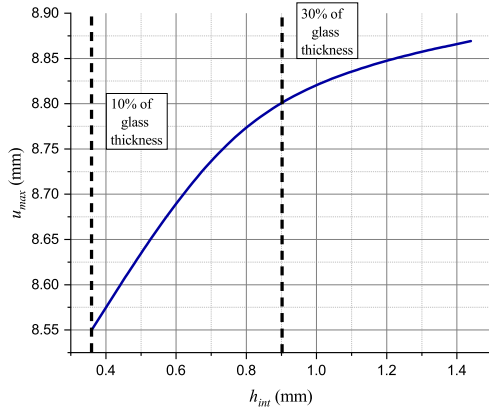


Figure 3.34: Dependence of u_{max} of plate bottom center node on the thickness of interlayer

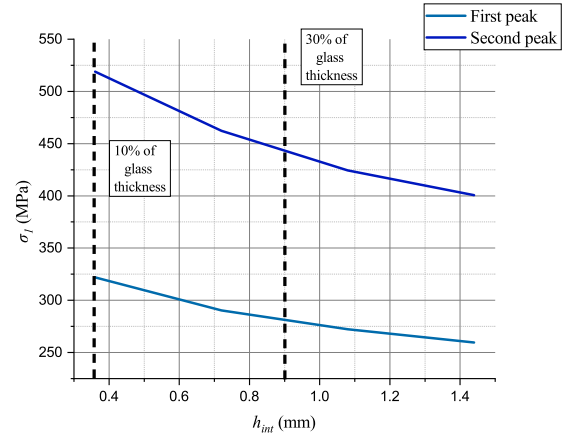


Figure 3.35: Dependence of first and second peak of σ_1 of plate bottom center node on the thickness of interlayer

Figure 3.34 demonstrates the relation between the maximum displacements at the bottom middle node of the plate and the thickness of the interlayer. Figure 3.35 shows the dependence of the first and second peaks of the maximum first principal stresses at the bottom middle node of the plate on the interlayer thickness.

The displacement data reveals that as the interlayer thickness increases, the displacement peaks rise incrementally by approximately 5% with each step. This trend can be attributed to the increased flexibility provided by thicker interlayers, which allow for greater deformation under impact loading. Thicker interlayers accommodate the kinetic energy of the impact by enabling larger displacements, effectively acting that absorbs and dissipates the force.

The maximum first principal stress results clearly show that as the interlayer thickness increases, the stress peaks decrease consistently. This reduction in stress is due to the ability of thicker interlayers to better distribute the impact forces across the plate, mitigating stress concentrations and protecting the structural integrity of the laminate. By providing enhanced energy absorption, thicker interlayers reduce the transfer of concentrated stresses to the outer layers of the laminated glass.

Figures 3.36 and 3.37 illustrate the maximum displacement u_{max} of the bottom node of the ball, the top center node of the plate, and the contact pressure F at the top center node of the plate over time. These plots provide insights into the interaction dynamics between the ball and the plate during impact.

The displacement of the ball and plate show the dynamic response of the system. As the ball impacts the plate, its displacement corresponds to the deformation of the plate's surface, particularly at the bottom middle node. The contact pressure is present only during the moments when the ball and the plate are in contact. During these intervals, the impact force generates significant contact pressure at the interface, which correlates with the deformation behavior of both the ball and the plate. The contact pressure peaks during the initial impact as the ball transfers its kinetic energy to the plate, causing localized stress and deformation. Conversely, during the

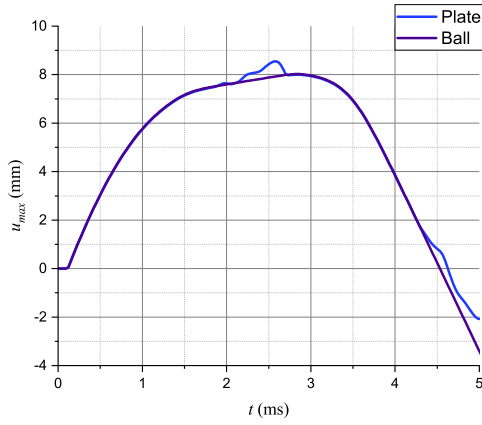


Figure 3.36: Dependence of u_{max} of ball bottom and plate top center node on time

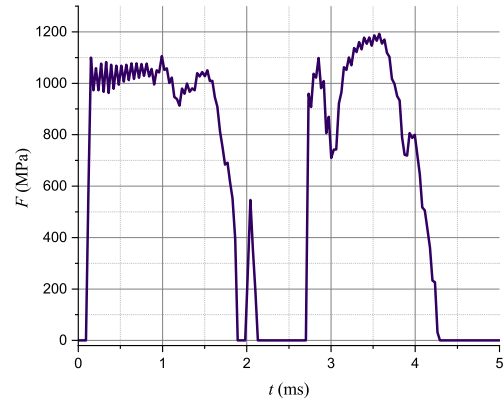


Figure 3.37: Dependence of F of plate top center node on time

periods when the ball and the plate are not in contact, the contact pressure drops to zero. These non-contact intervals occur as the ball rebounds away from the plate, illustrating the transient nature of the interaction. The alternating presence and absence of contact pressure reflect the oscillatory interaction, governed by the elastic properties of both the ball and the laminated glass plate.

4 Peridynamic modeling of glass plates

4.1 Discretization and boundary conditions

This chapter describes the use of PD theory to simulate and analyze the behavior of soda-lime glass plates under mechanical loading. Here, the focus is to describe PD model peculiarities and present a verification study compared to CCM solutions. The double ring-bending test was modeled and analyzed in this part of the work. It is a standard experimental setup for studying glass plate deformation and fracture characteristics. It involves applying loading and support rings to a squared plate's centered top and bottom. This configuration allows for observing displacement distribution, elastic deformation, and the subsequent fracture patterns that develop under increasing loads. Accurate modeling of such a test requires precise discretization, boundary conditions, and a force-interaction model to represent the contact mechanics between the load and support rings and the glass plate.

The primary objective of this section is to develop a computational framework using peridynamic theory to simulate the behavior of glass plates during the ring-bending test. A detailed methodology for discretizing the glass plate and the associated loading and support structures, ensuring high accuracy in modeling the physical behavior of the system, is introduced. The peridynamic discretization is shown in Figure 4.1.

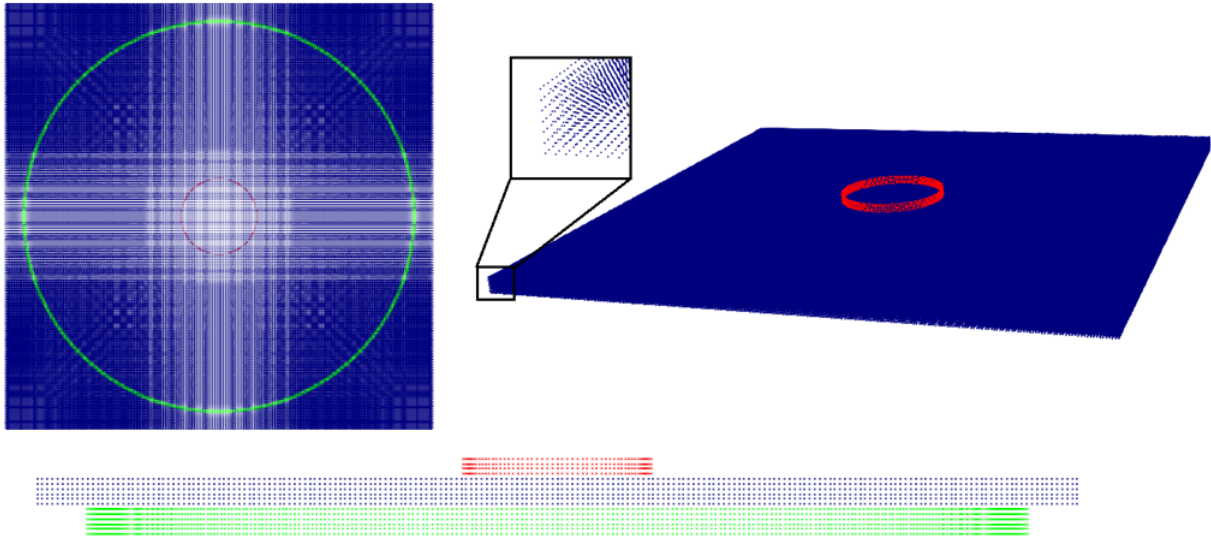


Figure 4.1: Peridynamic model

The primary subject of analysis is a square glass plate with dimensions of 100 mm in length and 2.9 mm in thickness. The plate was discretized using a regular lattice of nodes. The plate includes a total number of 254616 nodes with a nodal volume of 0.14 mm^3 and nodal size 0.483 mm, distributed as 206 nodes along the length and width and 6 nodes along the thickness. The plate volume is $2.9 \cdot 10^4 \text{ mm}^3$. The model presented in Figure 4.1 corresponds to the coaxial ring test, used in many studies to determine the flexural strength of glass. In this work, the

geometrical parameters and loading are used according to [53].

The load ring, defined by a radius of 9 mm, with a total number of 116 nodes and a total volume of 12.86 mm^3 , was represented. To ensure accurate modeling of force application, the model of 4 points along the thickness and 1.11 mm^3 nodal volume was chosen for the model for applying the force. Three layers, the size of the horizon, and one extra layer were used in alignment with the peculiarities of peridynamic theory, ensuring the proper incorporation of non-local interactions between material points. The top nodes of the load ring were subjected to a time-dependent body force applied at a constant rate of $8.5 \cdot 10^8 \text{ N/m}^3 \text{ s}$. An additional layer was strategically added to facilitate the smooth transition of forces from the load ring to the plate. This extra layer accounts for the peridynamic behavior near the interface, enabling a more realistic and stable simulation of force transfer.

Similarly, the support ring, with a radius of 45 mm, is represented by 584 nodes and 65.7 mm^3 volume, including 6 nodes along the thickness and 1.125 mm^3 nodal volume. The modeling of support is primarily to constrain the plate's displacements in the direction perpendicular to its surface. To achieve this, boundary conditions are applied to limit the motion of the three bottommost layers of nodes, which align with the horizon size in the peridynamic framework. These constrained layers form the foundation of the support ring's interaction with the plate. Additionally, three auxiliary layers are included above the constrained layers to facilitate a smooth transition of forces between the support ring and the plate.

4.2 The influence of node lattice type and density

The ring bending of a plate can be described analytically through the CCM approach with the Kirchhoff plate theory. These results are a proper benchmark solution for PD model verification and testing. Closed-form solutions for displacement, bending moments, strain and stress states can be derived from a simply supported circular plate subjected to the ring force [88]. For the circular plate model shown in Figure 4.2, the solution for the displacement function $u_z(r)$ can be presented as follows [53]

$$\frac{8\pi D}{F_{\text{res}}} u_z(r) = \begin{cases} f_1(r, r_{lr}) - f_1(r, r_{sr}) - \alpha, & \text{for } 0 \leq r \leq r_{lr}, \\ f_2(r, r_{lr}) - f_1(r, r_{sr}) - \alpha, & \text{for } r_{lr} < r \leq r_{sr}, \\ f_2(r, r_{lr}) - f_2(r, r_{sr}) - \alpha, & \text{for } r_{sr} < r \leq R \end{cases} \quad (4.1)$$

where

$$\begin{aligned} f_1(r, r_L) &= (R^2 - r_L^2) \frac{(3+v)R^2 - (1-v)r^2}{2(1+v)R^2} + (r_L^2 + r^2) \ln \frac{r_L}{R}, \\ f_2(r, r_L) &= (R^2 - r^2) \left(1 + \frac{1}{2} \frac{1-v}{1+v} \frac{R^2 - r_L^2}{R^2} \right) + (r_L^2 + r^2) \ln \frac{r}{R}, \\ \alpha &= f_2(r_{sr}, r_{lr}) - f_1(r_{sr}, r_{sr}) \end{aligned} \quad (4.2)$$

In Equation (4.1), $F_{\text{res}} = 2\pi r_{lr} f$ is the resultant force, f is the line force, r_{sr} is the radius of the support ring, r_{lr} is the radius of the load ring, and $R = 55 \text{ mm}$ is the radius of the plate. Analytical expressions for the bending moments as functions of the radial coordinate can also be derived based on this formulation [53]. The maximum displacement, $u_{\text{max}} = u(0)$, calculated using Equation (4.1), was compared to the PD simulation data for the elastic bending regime of

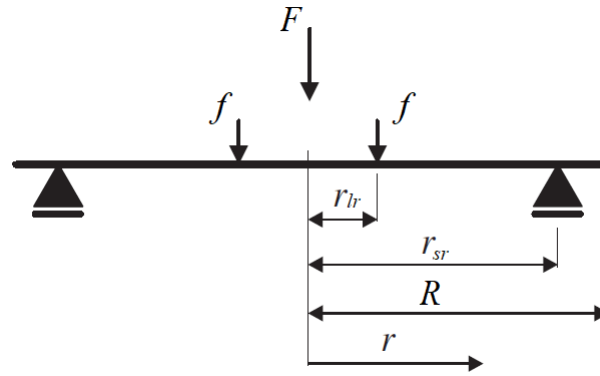


Figure 4.2: Geometry of circular plate and loading for the ring bending test

the plate, specifically before the initiation of any damage.

Figure 4.3 compares displacement values, u_z , as a function of the radial coordinate, r , obtained from the CCM and PD solutions. The close alignment of the curves indicates a strong agreement between the two methods. The results demonstrate that the Peridynamic model accurately captures the elastic deformation behavior predicted by the CCM.

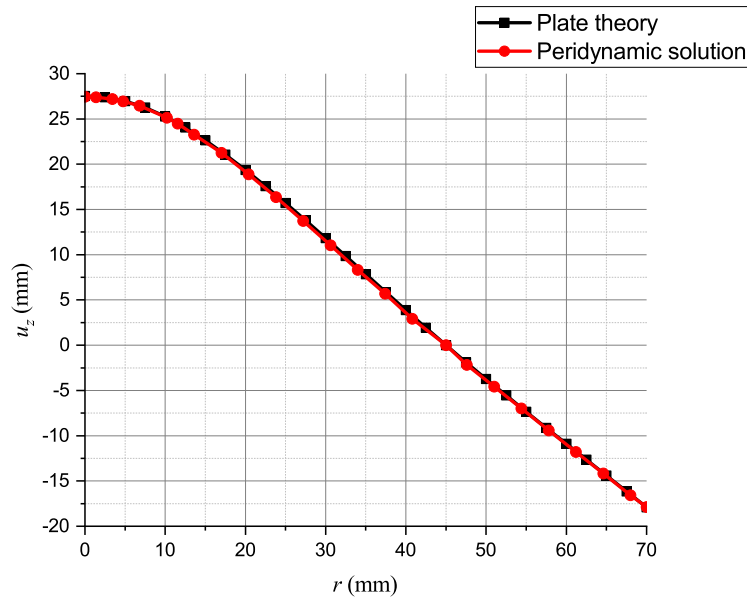


Figure 4.3: Comparison of solutions of displacements via radial coordinate

The difference in the maximum displacement at the midpoint of the plate is minimal, less than 2%, validating the precision of the PD approach in modeling the elastic bending regime before the damage initiation. This close agreement confirms the reliability of the PD model in reproducing results consistent with established analytical solutions, under such loading conditions.

Additionally, the consistency across the entire radial domain reinforces the robustness of the Peridynamic method for capturing displacement patterns, offering a solid foundation for its application in more advanced scenarios involving non-linear behavior or damage evolution.

A key aspect of the accuracy and reliability of PD simulations lies in the discretization of the material domain into a lattice of nodes. The node lattice type (e.g., regular, irregular, or random)

and the density of nodes directly influence the quality of the results, computational cost, and numerical stability and convergence behavior of the analysis.

Irregular lattices can lead to instability or inaccuracies in capturing non-local interactions, particularly in regions with high-stress gradients, such as around crack tips or boundaries. A regular square lattice is straightforward to construct and implement in numerical simulations. This simplicity reduces the risk of errors during the discretization process and ensures consistency in modeling. Regular grids allow for systematic and predictable connectivity between nodes, making it easier to compute non-local interactions. This reduces the computational overhead of searching for interacting nodes (neighbors). In this study, the regular Cartesian lattice was chosen.

Higher node densities increase computational demands, including memory usage and simulation time. Conversely, lower node densities can compromise the resolution of critical features, such as crack propagation paths or localized deformation zones. Investigating the impact of node density makes it possible to develop strategies for adaptive meshing or hybrid approaches that optimize computational resources while maintaining accuracy.

Comparative studies on the effects of lattice type and density will provide benchmarks for validating PD models against experimental data and analytical solutions. Understanding these influences will help establish best practices for peridynamic modeling, ensuring that simulations are reliable and reproducible across various applications.

The choice of lattice density plays an important role in ensuring the accuracy and stability of peridynamic simulations, as it determines the spatial resolution of the model and directly affects the ability to capture fine details of deformation and stress distribution. However, more than the lattice density is required to define the peridynamic model's behavior fully. Equally important is the horizon size, which governs the range of non-local interactions between material points.

While lattice density controls the discretization of the domain, the horizon size defines the extent of influence each node has over its neighbors, linking the discretized model to the physical scale of material interactions. The relationship between these two parameters, particularly the ratio of horizon size to node spacing ($\delta/\Delta x$), is critical for balancing numerical stability, computational efficiency, and physical accuracy. Understanding this interplay is essential for optimizing peridynamic simulations, especially when modeling complex phenomena such as crack initiation and propagation in brittle materials.

An adequately chosen horizon size ensures that the material's mechanical response reflects the underlying physics. It defines the scale at which interactions occur and influences the material's stiffness, fracture toughness, and deformation behavior. For brittle materials like glass, which exhibit complex crack patterns, the horizon size determines how well the PD model can replicate stress fields and capture crack initiation and propagation.

The horizon size significantly impacts the accuracy and convergence of PD simulations. A horizon size that is too small may need to be more significant to capture the non-local effects adequately, leading to inaccurate stress and displacement distributions. Conversely, a big horizon size can smooth out localized phenomena, such as sharp crack tips, reducing the fidelity of the simulation. Horizon size must be carefully chosen to balance these effects, ensuring accurate results converging to the proper solution as the node density increases.

This section focuses primarily on the displacement analysis of the glass plate model described earlier. The goal is to investigate how variations in lattice density and horizon size influence the accuracy and behavior of the PD solution, particularly in comparison with the analytical solution. Specifically, lattices with 6, 7, and 8 nodes through the plate thickness were considered. Additionally, the horizon size was varied. The horizon sizes considered were 1.81 mm, 1.55 mm, 1.36 mm. Figures 4.4, 4.5, and 4.6 show the displacement of the glass plate bottom middle node as a function of time for various lattice configurations and horizon sizes in the PD model,

compared to the reference solution.

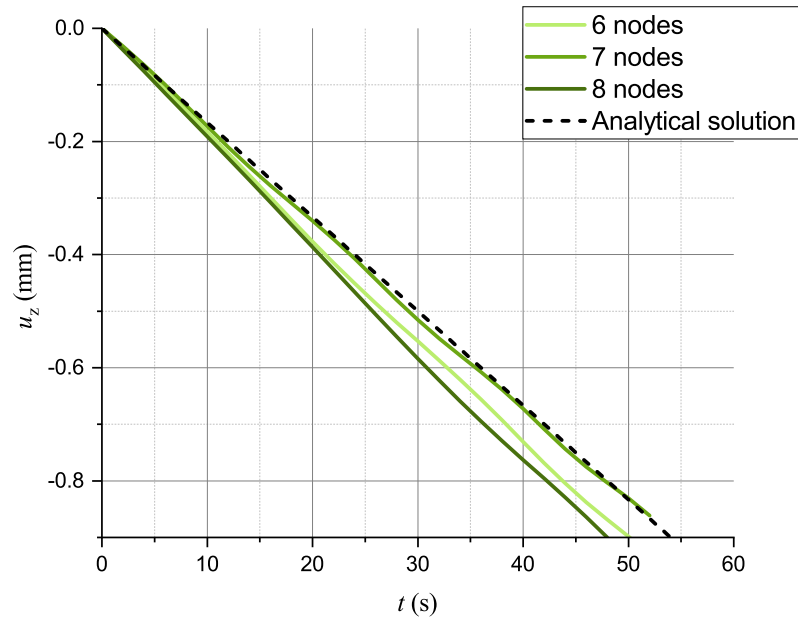


Figure 4.4: Dependence of bottom middle node displacement on time with $\delta = 1.36$ mm and different number of nodes

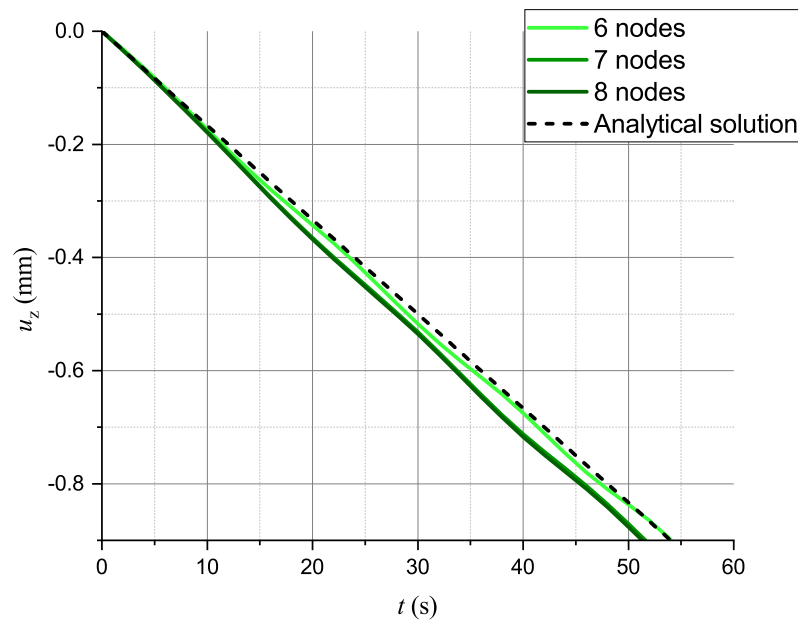


Figure 4.5: Dependence of bottom middle node displacement on time with $\delta = 1.55$ mm and different number of nodes

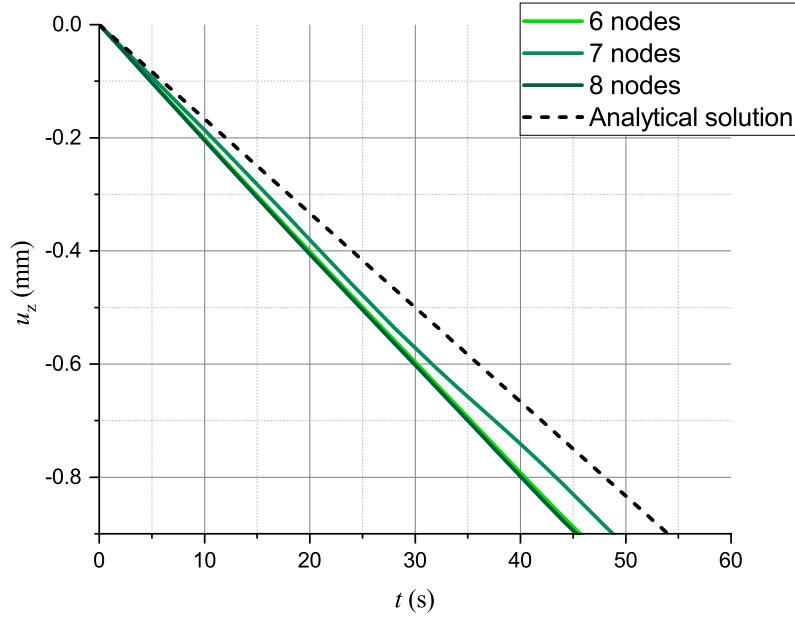


Figure 4.6: Dependence of bottom middle node displacement on time with $\delta = 1.81$ mm and different number of nodes

All curves display a linear decrease in displacement over time, consistent with the quasi-static loading applied to the glass plate. This indicates that the elastic behavior of the material is being accurately captured across all configurations. The analytical solution shows a continuous, smooth trend, with the PD solutions following it closely but exhibiting slight variations depending on the number of nodes through the thickness and horizon sizes.

Considering the results for a horizon size of 1.36 mm, the configuration with 7 nodes through the plate thickness demonstrates the closest match to the analytical solution. In contrast, the configuration with 6 nodes deviates slightly, and the 8 node configuration exhibits the most significant error. For the horizon size of 1.55 mm, the results align more closely with the analytical solution across all lattice densities, particularly for the configuration with 6 nodes, which achieves notable accuracy. Regarding the largest horizon size 1.81 mm, the displacement curves for the 6 node and 8 node configurations diverge more significantly from the analytical solution. In contrast, the 7 node configuration provides comparatively better alignment but is less accurate than the results obtained with smaller horizon sizes.

When examining the influence of lattice density across different horizon sizes, for 6 nodes, the results are closest to the analytical solution when the horizon size is 1.55 mm, for 7 nodes, the results align best with the analytical solution for a horizon size of 1.36 mm, for 8 nodes, the closest match to the analytical solution is achieved with a horizon size of 1.55 mm.

Higher lattice densities generally improve accuracy and stability, providing better resolution of the displacement field and reducing the likelihood of numerical errors. However, this comes at the cost of increased computational demands. Smaller horizon sizes enhance accuracy and stability for coarser lattices by reducing the range of non-local interactions, making simulations less computationally intensive and more numerically stable.

While higher lattice densities (e.g., more than 8 nodes) would likely yield more accurate results, computational limitations prevented their evaluation in this study. These limitations highlight the

importance of balancing lattice density, horizon size, and available computational resources.

The horizon size and lattice density significantly influence simulation results. Deviations from the analytical solution could arise due to numerical errors, inadequate lattice refinement, or an unsuitable horizon-to-lattice spacing ratio. The observed variations underscore the necessity of carefully tuning the lattice density and horizon size according to the specific model geometry and loading conditions to achieve optimal accuracy and stability.

It is important to acknowledge that the density of the glass was artificially increased in this study, which could introduce numerical errors into the simulation results. These errors have an impact on the computed displacements, highlighting the need for further refinement of the model. In future work, we plan to address this issue by reducing the glass density and implementing an alternative approach to mitigate the numerical inaccuracies. This improved methodology will be detailed in the next chapter, providing a more robust framework for peridynamic simulations and enhancing the accuracy of the results.

4.3 Comparative study based on peridynamic and finite element analysis

This section focuses on analyzing the elastic behavior of the previously described model using two computational approaches: the PD and FEM. The aim is to compare these methods in modeling the same scenario: a soda-lime glass plate subjected to quasi-static ring loading and a ring supported. The glass plate is modeled with the same geometric and loading parameters across both methods to ensure consistency and comparability.

The quasi-static ring loading configuration provides an ideal scenario for evaluating the elastic deformation. This analysis restricts the scope to the elastic regime, where the material remains undamaged and the stress-strain response is linear. By eliminating considerations of fracture or damage evolution, the focus is placed on evaluating the accuracy, computational efficiency, and fundamental differences in how PD and FEM capture the elastic deformation of the glass plate under the given loading conditions. In FEM, the glass plate is modeled as a continuum, with discretization into finite elements providing local stress-strain relationships. In contrast, PD models the plate using a non-local framework, where each material point interacts with its neighbors within a defined horizon.

Building on the detailed description of the peridynamic modeling framework, we now focus on its application in analyzing the elastic response of the glass plate under the quasi-static ring loading setup. To highlight the capabilities of the peridynamic method, we begin by discussing its implementation and results, emphasizing how it handles the elastic deformation of the plate and the interactions at the contact surfaces.

The horizon size, a key parameter in PD modeling, was set to 1.81 mm corresponding to interaction through three nodes of family nodes. The plate and the rings were modeled using a linear peridynamic solid (LPS) model, which accurately represents elastic behavior. The interactions at the contact surfaces between the rings and the plate were governed by a short-range force model with a spring constant of $5 \cdot 10^{22}$ and a search and contact radius of 0.387 mm, as outlined in [43].

The material properties of the glass model with Young's modulus $E = 70$ GPa, Poisson ratio $\nu = 0.22$ were used. To reduce computational costs during the quasi-static analysis, the material density was artificially increased to $\rho = 2500 \cdot 10^8$ kg/m³ to allow for a larger critical time step in the explicit time-stepping method. The quasi-static step analyzes the plate's primary stage of elastic deformation. The implicit time integration (details are presented in [43]) with the absolute

tolerance of 1.0 and 10 maximum solver iterations is applied for the solution. The analysis is performed with Peridigm, an open-source computational peridynamics code.

FEM was performed using ANSYS to provide a comparative benchmark. The plate was meshed with 20-node SOLID186 elements, known for their high precision in modeling three-dimensional elastic deformation. The free mesh was modeled. The plate includes a total number of 875120 nodes, with 6 nodes through the plate thickness, that utilized a peridynamic lattice. All the components of the model are deformable. The plate was modeled in a 3D staging as part of a physical linear-elastic setting. The interaction of the load, support rings, and the plate was carried out within the framework of achieving the objective of one-way contact according to the «surface to surface» algorithm. The air resistance during the impact was ignored. The material properties were set the same as in PD model. The nodal force 2 kN was applied to the load ring nodes. The 10 timesteps were used.

The PD lattice was created from FEM mesh taking the coordinates of the element centers. The PD and FEM meshes are shown in Figure 4.7.

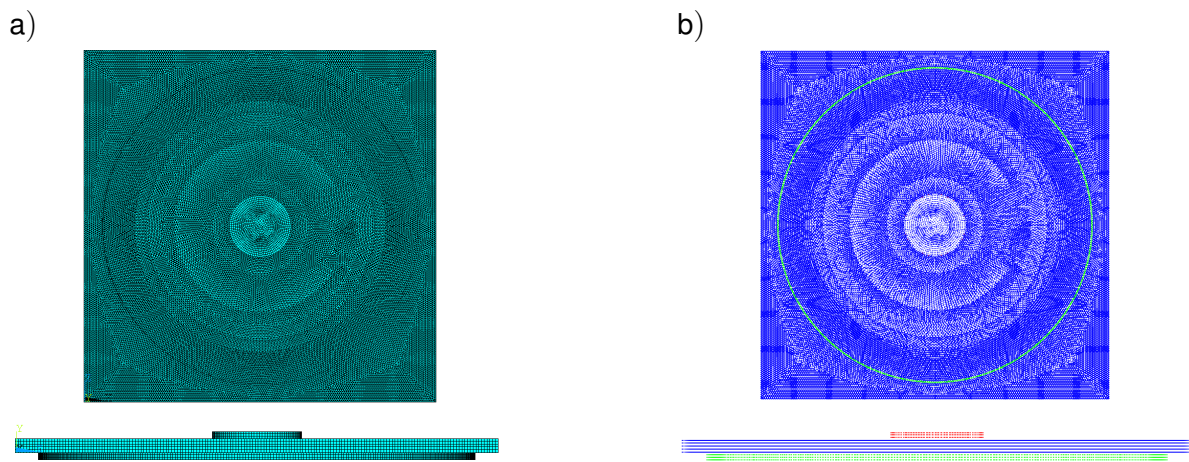


Figure 4.7: Discretisation of the simulation model.

a) FEM mesh, b) PD lattice

The comparison of displacements obtained using different methods is presented in Figure 4.8.

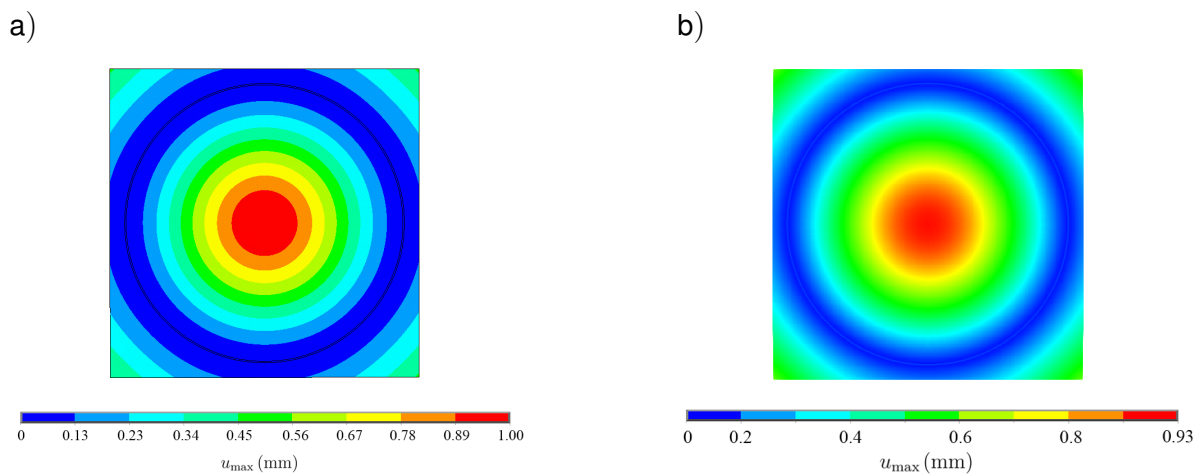


Figure 4.8: Distribution of displacement over the bottom side.

a) FEM solution, b) PD solution

The results demonstrate good agreement between the FEM and PD approaches, highlighting the consistency of these models in capturing the elastic response of the plate under quasi-static ring loading.

The maximum displacement values predicted by the two methods differ by less than 7%. This close correspondence indicates that the peridynamic model, despite its inherently non-local nature, is capable of producing results comparable to those obtained using FEM. The displacement distributions across the plate also exhibit similar patterns for both methods, confirming that the loading and boundary conditions are correctly implemented in both simulations. The PD model's slightly lower maximum displacement could be attributed to the discretization choices, including the horizon size, nodal arrangement, or the specific non-local interactions considered in peridynamic theory.

This comparison underscores the reliability of PD in replicating FEM results for elastic analysis while also showcasing the potential of peridynamics to extend into scenarios where FEM might face limitations, such as modeling fracture or discontinuities. The agreement between the methods builds confidence in the peridynamic model's accuracy and highlights its applicability for complex material and structural simulations.

5 Analysis of damage and crack patterns

5.1 Influence of critical bond stretch parameter under quasi-static loading

This section focuses on the detailed analysis of the ring-bending model introduced earlier, particularly emphasizing the initiation and evolution of damage patterns. Using peridynamic theory, which is well-suited for modeling fracture and failure processes in brittle materials, we investigate damage type, location, and propagation under the applied quasi-static loading conditions.

The critical bond stretch, s_c , is a fundamental material parameter in the PD damage model that governs the initiation and evolution of bond failure [96]. Accurate determination of s_c is essential for reliable PD simulations, as it directly affects the predicted damage initiation and fracture propagation patterns. The value of s_c is typically determined based on experimental data, particularly by correlating it with the critical force required to induce fracture.

Two primary approaches are commonly used to define the critical bond stretch s_c , depending on the assumptions made about the material's surface condition [53].

The first approach assumes a perfect, defect-free material with an idealized surface condition. The critical bond stretch s_c is derived assuming that the material's strength is governed solely by its intrinsic properties, without the influence of surface imperfections or micro-cracks.

In the second approach, the material is assumed to have pre-existing flaws, micro-cracks, or imperfections inherent in real-world materials. The critical bond stretch s_c is determined based on these flaws, accounting for their influence on the material's strength and fracture behavior.

In this section, we will consider the first approach. This approach for determining the critical bond stretch, s_c , assumes a flawless material model, focusing on damage initiation based on results from the co-axial ring-bending test. In this methodology, s_c is derived directly from the strain state within the plate before damage initiation, during the elastic loading stage.

Before damage initiation, the strain state within the plate, particularly inside the radius of the load ring, remains homogeneous. In this elastic regime, the bond stretch s for any bond ξ in the plane of the plate is directly related to the linear strain tensor ε through the following expression

$$s = \frac{\xi \cdot \varepsilon \cdot \xi}{|\xi|^2}, \quad \varepsilon = \varepsilon_0(\mathbf{I} - \mathbf{n} \otimes \mathbf{n}) \quad (5.1)$$

where \mathbf{I} is the second-rank unit tensor, \mathbf{n} is the unit normal to the plate face, and ε_0 represents the strain state at the tensile surface of the plate.

The strain ε_0 is computed from the tensile strain state, characterized by the radial strain component ε_r and the circumferential strain component ε_φ . These components are given by [53]

$$\varepsilon_0 = \varepsilon_r = \varepsilon_\varphi = \frac{3F}{4\pi h^2 E} \left[(1 - \nu)^2 \frac{r_{sr}^2 - r_{lr}^2}{R^2} + 2(1 - \nu^2) \ln \frac{r_{sr}}{r_{lr}} \right] \quad (5.2)$$

This equation provides the strain state as a function of the applied force F , material properties,

and geometric parameters of the ring-bending test. The critical bond stretch s_c is directly estimated from the critical force value F_c , corresponding to the force at which damage initiation occurs. Substituting F_c into the strain expression

$$s_c \approx \varepsilon_{0c} = \frac{3F_c}{4\pi h^2 E} \left[(1 - \nu)^2 \frac{r_{sr}^2 - r_{lr}^2}{R^2} + 2(1 - \nu^2) \ln \frac{r_{sr}}{r_{lr}} \right] \quad (5.3)$$

For the mean critical force value, Equation (5.3) gives $s_c = 2.0 \cdot 10^{-3}$.

In this section, the ring-bending model that was described previously is taken into consideration. The model with 6 nodes along the plate thickness is used. Damage patterns for the type and the location of the damage initiation are analyzed. The critical stretch damage model with $s_c = 2.0 \cdot 10^{-3}$ was calculated. The horizon size was set to 1.81 mm. The plate and the rings were modeled using a LPS model. The interactions at the contact surfaces between the rings and the plate were governed by a short-range force model with a spring constant of $5 \cdot 10^{22}$ and a search and contact radius of 0.387 mm. The material properties of the glass model with Young's modulus $E = 70$ GPa, Poisson ratio $\nu = 0.22$ were used. The material density was set to $\rho = 2500 \cdot 10^3$ kg/m³ to allow for a larger critical time step in the explicit time-stepping method. The analysis was divided into two load steps to reduce computational costs. The first step focused on a quasi-static analysis to examine the plate's initial stage of elastic deformation. This phase utilized implicit time integration, as detailed in [43], with an absolute tolerance of 1.0 and a maximum of five solver iterations to ensure accurate convergence.

The second step addressed the transient dynamic phase, aimed at analyzing damage evolution and the dynamic phenomena associated with the formation and progression of damage patterns. In this phase, time integration was performed using an explicit time-stepping method based on the central difference scheme, which effectively approximates the second time derivative of the displacement vector. The methodology and critical time step estimation for this approach are thoroughly explained in [82], [43]. This two-step strategy balances computational efficiency and the accurate modeling of elastic deformation and complex damage dynamics.

The analysis is performed with Peridigm, an open-source computational peridynamics code.

Figure 5.1 presents the damage distribution on the bottom surface of the plate for a constant critical bond stretch value of $s_c = 2.0 \cdot 10^{-3}$.

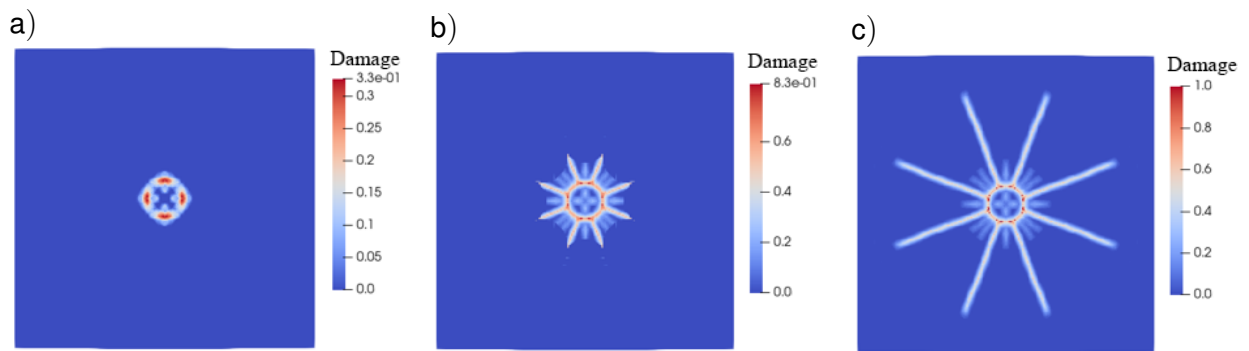


Figure 5.1: Damage distribution on the bottom side of a plate.

a) $t = 51.7253$ s, b) $t = 51.7253$ s + 0.5 ms, c) $t = 51.7253$ s + 4.4 ms

The damage pattern is visualized at multiple time points during the simulation, illustrating the progression of damage initiation and propagation.

In this scenario, the plate is initially assumed to be homogeneous. As the simulation progresses,

a ring-shaped damage zone can be observed inside the radius of the applied load. Figure 5.1 a) shows 33% damage that occurred. This ring damage zone is the first to form due to the stress concentration induced by the loading configuration. Subsequently, a series of radial cracks emanates from the ring-shaped damage zone, radiating outward towards the edges of the plate with 83% damage (Figure 5.1 b)) and 100% damage (Figure 5.1 c)). These radial cracks are a characteristic failure mode for brittle materials under such loading conditions, driven by the tensile stresses exceeding the material's critical bond stretch. According to the results, the damage initiation occurs on 51.7253 s and propagates fast during 4.4 ms.

This figure underscores the capability of the peridynamic model to accurately capture the complex damage behavior in brittle materials, including the interaction between ring-shaped damage zones and the initiation of radial cracks. Such patterns are consistent with experimental observations of fracture in similar setups, validating the peridynamic approach for predicting fracture dynamics in glass plates.

Building on the previous analysis of damage progression in the plate with a fixed critical bond stretch, we now investigate how variations in the critical bond stretch parameter influence damage behavior. By exploring different values of s_c , we can examine its impact on the rate of damage progression, the patterns of crack propagation, and the overall failure mechanisms of the plate.

Figure 5.2 illustrates the influence of different critical bond stretch values on the damage evolution in a glass plate. The damage evolution and patterns are visualized for three different values $s_c = 1.0 \cdot 10^{-3}$, $s_c = 0.75 \cdot 10^{-3}$ and $s_c = 0.5 \cdot 10^{-3}$.

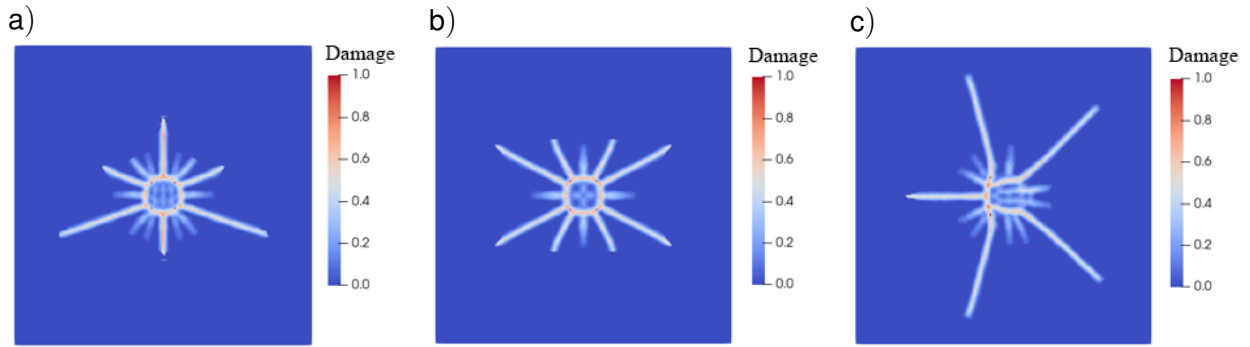


Figure 5.2: Damage distribution on the bottom side of a plate with different critical stretch value.
a) $s_c = 1.0 \cdot 10^{-3}$ at $t = 25.5$ s, b) $s_c = 0.75 \cdot 10^{-3}$ at $t = 19.1$ s, c) $s_c = 0.5 \cdot 10^{-3}$ at $t = 12.7$ s

When comparing the results for $s_c = 2.0 \cdot 10^{-3}$ and $s_c = 1.0 \cdot 10^{-3}$, the damage time decreases significantly, approximately by half. For $s_c = 1.0 \cdot 10^{-3}$, the plate becomes fully damaged at $t = 25.5$ s. The damage pattern begins with forming a well-defined ring-shaped damage zone inside the load ring radius. This is followed by the development of radial cracks that extend outward from the ring. These radial cracks exhibit a symmetrical and evenly distributed pattern, directly resulting from the uniform material properties and loading conditions. The reduction in s_c leads to a lower tolerance for deformation before bond failure occurs, meaning the material is more susceptible to damage under the same loading conditions.

When s_c is reduced to $0.75 \cdot 10^{-3}$, the plate becomes fully damaged at $t = 19.1$ s, a noticeable decrease in destruction time compared to higher s_c values. Similar to the previous case, a central ring-shaped damage zone forms within the load ring radius, followed by the development of radial cracks, and radial cracks maintain a symmetrical and evenly distributed pattern. The reduction in s_c lowers the material's tolerance for deformation, causing bonds to fail at more minor strains.

This results in faster damage progression and a shorter overall time to destruction. The crack formation and propagation acceleration illustrate the material's increased fragility under reduced s_c values.

When setting $s_c = 0.5 \cdot 10^{-3}$, damage develops rapidly, with the plate reaching full damage at $t = 12.7$ s. This represents the shortest destruction time observed in the series of simulations, highlighting the profound impact of a lower s_c on the damage evolution process. As in the previous cases, radial cracks initiate within the load ring radius and propagate outward. However, unlike the earlier scenarios, the radial cracks do not maintain a symmetrical or evenly distributed pattern. This deviation from symmetry suggests the emergence of numerical instability within the model, likely worsened by the significantly reduced s_c . The lower s_c value causes bonds to fail under minimal deformation, amplifying the sensitivity of the simulation to local variations in deformation. The reduced s_c drastically decreases the material's resistance to bond failure, leading to a rapid and less predictable damage progression. The asymmetrical damage pattern could also indicate that the system is more susceptible to localized instabilities, which may dominate the failure process when s_c is small.

Lower s_c values result in faster damage propagation and more pronounced crack formation, highlighting the sensitivity of the peridynamic damage model to this parameter. These results highlight the critical role of s_c in influencing the rate of damage progression and the stability and predictability of fracture patterns in the peridynamic model. This analysis demonstrates the vital role of s_c in determining the rate and pattern of damage evolution in brittle materials. By adjusting s_c , the peridynamic model can accurately replicate different fracture dynamics.

In the following example, the influence of a layer-dependent critical bond stretch (s_c) on the damage progression in the plate under the same loading conditions. The simulation employs a lattice with 6 nodes through the plate thickness and a horizon size of 1.81 mm. The critical bond stretch is set to $1.5 \cdot 10^{-3}$ for the surface nodes of the bottom layer, while it is $2.0 \cdot 10^{-3}$ elsewhere within the plate. The simulation results are shown in Figure 5.3.

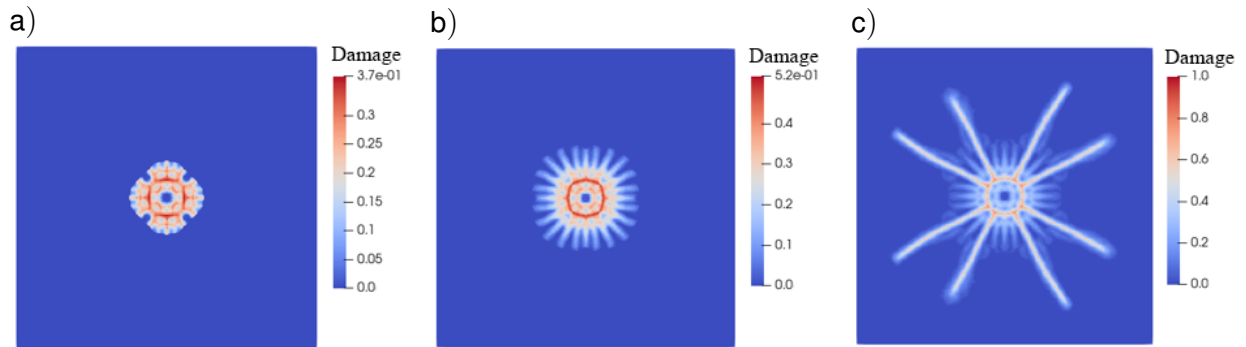


Figure 5.3: Damage distribution on the bottom side of a plate with $s_c = 1.5 \cdot 10^{-3}$ at the surface nodes of bottom layer.

a) $t = 38.601$ s, b) $t = 38.601$ s + 1.6 ms, c) $t = 38.601$ s + 10 ms

The damage initiation accrues around $t = 38.6$ s. At this early stage, damage is localized and confined to the area inside the load ring radius, as it happened before. The damage distribution forms a circular pattern due to the stress concentration induced by the loading configuration. As the simulation progresses, the damage zone expands, and a well-defined ring-shaped damage area becomes prominent. Radial cracks emerge from the ring damage zone, extending symmetrically toward the plate edges. Within 10 ms, the plate is fully damaged. The damage pattern includes a complete central ring damage zone surrounded by fully developed radial cracks. As in previous cases, the cracks exhibit a symmetrical and evenly distributed pattern on the bottom

surface layer. Compared to the plate with $s_c = 2.0 \cdot 10^{-3}$, the damage initiation time decreases on 25%. The damage propagation takes more time till the damage reaches 100%. This highlights the sensitivity of surface layers to lower s_c , leading to the rapid progression of damage outward from the bottom layer.

In the next calculation, the critical bond stretch is set to $1.0 \cdot 10^{-3}$ for the surface nodes of the bottom layer, while it is $2.0 \cdot 10^{-3}$ elsewhere within the plate. The simulation results are shown in Figure 5.4.

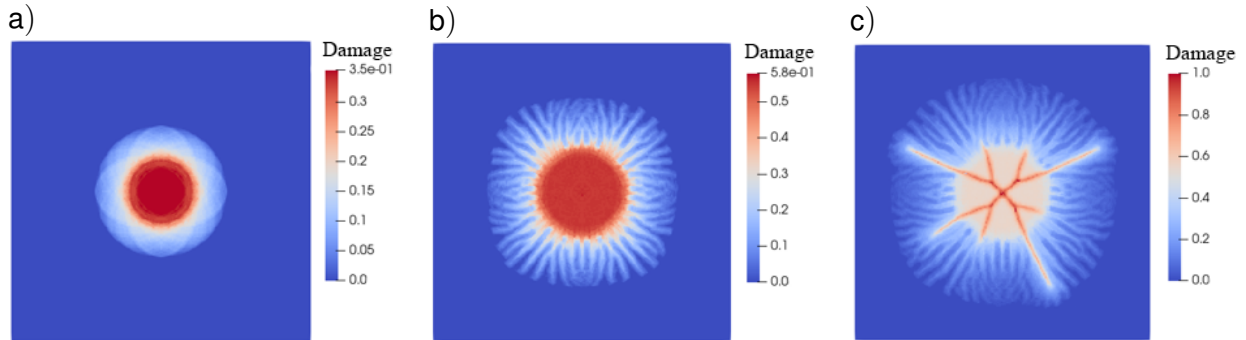


Figure 5.4: Damage distribution on the bottom side of a plate with $s_c = 1.0 \cdot 10^{-3}$ at the surface nodes of bottom layer.

a) $t = 35.12$ s, b) $t = 35.12$ s + 7.9 ms, c) $t = 35.12$ s + 9.6 ms

At the initial stage, damage localizes within the bottom surface nodes. The damage distribution forms a circular zone around the load ring radius, corresponding to the area of maximum stress concentration caused by the applied loading conditions. The contrast between the surface nodes with lower s_c and the material with higher s_c is evident, as damage predominantly initiates and grows within the surface layer. Over the next 7.9 ms, the damage zone expands significantly, with the circular zone widening and intensifying. The ring-shaped damage zone becomes more prominent on the bottom surface. This stage highlights the accelerated damage progression driven by the weaker surface nodes, which act as initiation points for further damage propagation. The plate is fully damaged in 9.6 ms. At this stage, the damage pattern transforms into a well-defined system of radial cracks, extending symmetrically outward from the load ring to the edges of the plate. Unlike the previous case with $s_c = 1.5 \cdot 10^{-3}$ for the bottom surface nodes, this final stage has no clearly defined central ring-shaped damage zone. Compared to that case, the time is 9% less when the damage reaches 100%. The lower s_c in the surface nodes results in faster damage initiation and propagation, demonstrating how even small changes in critical bond stretch can significantly influence the overall failure dynamics.

In the subsequent simulation, the critical bond stretch is assigned a value of $0.75 \cdot 10^{-3}$ for the surface nodes of the bottom layer, while it remains $2.0 \cdot 10^{-3}$ throughout the rest of the plate. The corresponding simulation results are presented in Figure 5.5.

The damage initiation occurs approximately $t = 27.2$ s within the bottom surface nodes. Similar to previous cases, the damage distribution initially forms a circular zone around the load ring radius. However, the propagation time for damage progression is noticeably different in this case. To reach 100% damage, the simulation shows a total time of approximately 6.81 s following initiation. This represents a much longer propagation phase than earlier cases where the damage progression to completion occurred in milliseconds. A well-defined ring-shaped damaged area becomes prominent, with radial cracks emerging from the ring damage zone, extending symmetrically toward the plate edges at the last stage of damage development. At the final stage of damage development, the radial cracks dominate the pattern, reflecting the stress redistribution

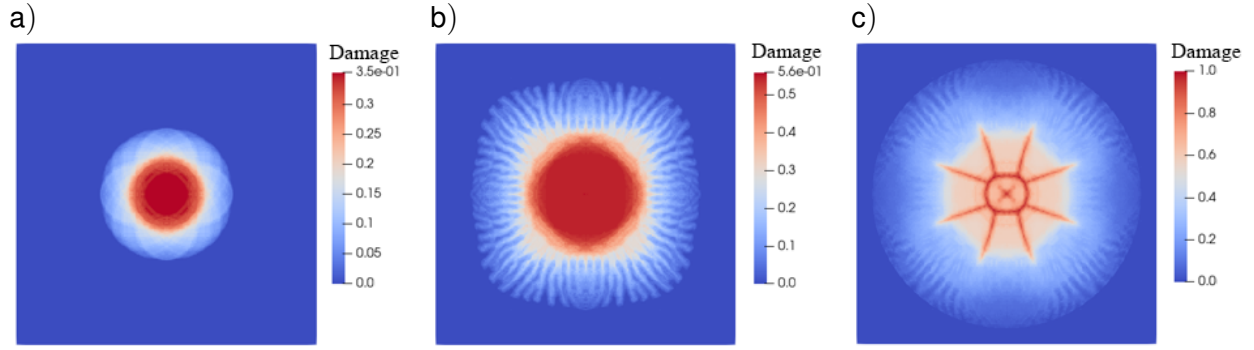


Figure 5.5: Damage distribution on the bottom side of a plate with $s_c = 0.75 \cdot 10^{-3}$ at the surface nodes of bottom layer.

a) $t = 27.2$ s, b) $t = 34.0074$ s, c) $t = 34.0109$ s

across the plate. Notable differences are observed compared to the previous case, where the bottom surface nodes had $s_c = 0.75 \cdot 10^{-3}$. The damage initiation time is reduced by approximately 22.5%. The time required for the plate to reach 100% damage is roughly 3% shorter than in the previous case. This reduction demonstrates that the lower s_c expedites the overall failure process, though the delay caused by the higher s_c in the material limits the extent of this acceleration.

The last in this series of calculations is shown in Figure 5.6. The critical bond stretch is set to $0.5 \cdot 10^{-3}$ for the surface nodes of the bottom layer, while it remains $2.0 \cdot 10^{-3}$ throughout the rest of the plate.

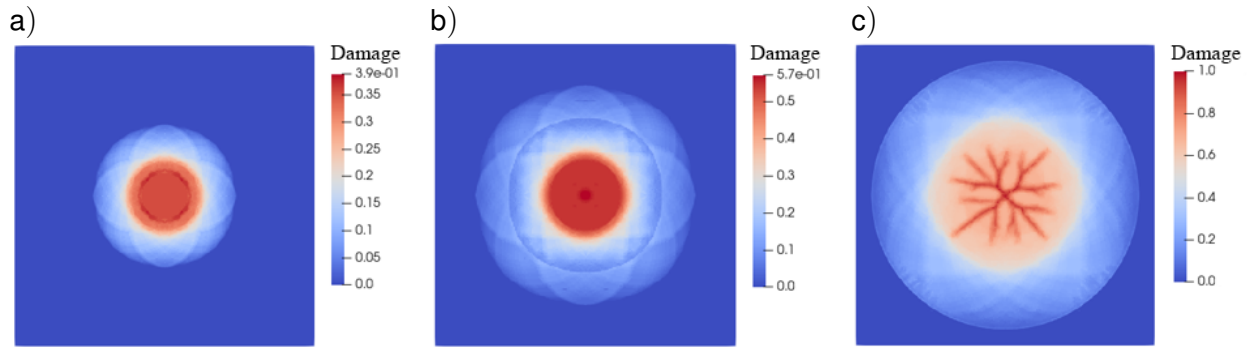


Figure 5.6: Damage distribution on the bottom side of a plate with $s_c = 0.5 \cdot 10^{-3}$ at the surface nodes of bottom layer.

a) $t = 19.8$ s, b) $t = 33.001$ s, c) $t = 33.0082$ s

It can be seen that the damage initiation occurs approximately $t = 19.8$ s within the bottom surface nodes. The damage distribution initially forms a circular zone around the load ring radius. Then, the damage pattern transforms into a well-defined system of radial cracks, extending symmetrically outward from the load ring to the edges of the plate. A key observation in this case is the significantly longer propagation time for damage progression. The propagation time for damage progression takes around 13.2 s, which is even double longer than in the case with $s_c = 0.75 \cdot 10^{-3}$. The damage initiation time is reduced by approximately 27.2%. The time required for the plate to reach 100% damage is around 3% shorter than in the previous case.

Table 5.1 summarizes the results of damage simulations for various configurations of s_c in a plate subjected to quasi-static loading. The table evaluates the effects of different s_c values on

damage initiation time, percentage of damage at critical times, and the time to achieve 100% damage (critical time). The results are presented for plates with 6 or 7 nodes along the plate thickness and varying s_c values for the entire plate or specifically for the bottom layer.

Table 5.1: The results of s_c and model lattice influence on the damage.

Nodes along the plate thickness	s_c of the whole plate	s_c of the bottom layer	Initiation Time, s	Damage %	Critical Time, s	Damage %
6	0.002	0.002	51.7253	33	51.726	100
7	0.002	0.002	55.8005	50	55.8016	100
6	0.002	0.0015	38.601	37	38.611	100
7	0.002	0.0015	41.5005	52	41.503	100
6	0.001	0.001	25.5104	56	25.511	100
6	0.002	0.001	28.096	0.68	35.1296	100
6	0.00075	0.00075	19.10057	57	19.101	100
6	0.002	0.00075	20.4	0.68	34.0088	100
7	0.002	0.00075	24.0	0.24	40.0074	100
6	0.0005	0.0005	12.7379	54	12.74	100
6	0.002	0.0005	19.8	39	33.0082	100
6	0.002	0.004	85.0	35	85.0018	100
6	0.004	0.002	57.6	0.68	72.009	100

Assigning a lower s_c to the bottom surface layer accelerates damage initiation, as weaker bonds fail earlier under stress concentration. Uniform higher s_c values throughout the plate delay initiation and progression, reflecting the material's resistance to bond failure. Increasing the number of nodes along the thickness improves resolution and delays initiation and propagation, providing greater accuracy but requiring more computational time. Extremely low s_c values in the bottom layer drastically shorten the initiation and critical damage times, demonstrating the importance of s_c calibration for realistic fracture modeling.

The simulations underscore the complex interplay between surface and bulk properties in determining the fracture behavior of brittle plates. The lower s_c in the surface nodes leads to earlier damage initiation, while the higher s_c delays the final failure. The significantly longer propagation time for damage progression highlights the importance of material properties in controlling the overall fracture dynamics, even when the surface layer is the primary site of damage initiation.

The results also emphasize the importance of carefully choosing s_c values for surface and main layers in peridynamic models. These findings provide valuable insights into layered brittle materials' mechanics and critical bond stretch's role in controlling failure mechanisms under complex loading conditions.

5.2 Influence of critical bond stretch parameter under impact loading

This section presents an analysis of the glass plate under impact loading, focusing on the initiation and progression of damage patterns. The subject of the analysis is the same square glass plate with dimensions of 100 mm in length and 2.9 mm, including 6 nodes along the thickness. The same support ring, with a radius of 45 mm with 6 nodes along the thickness, is represented

to constrain the plate's displacements in the direction perpendicular to its surface. The material properties of the glass model with Young's modulus $E = 70$ GPa, Poisson ratio $\nu = 0.22$ and $\rho = 2500$ kg/m³ were used. To perform the impact on the model, the steel ball with a radius of 6.5 mm (9 g) is introduced. Only a representative segment of the ball in direct contact with the plate is modeled to reduce the computational expense. The methodology involves meshing a hemispherical segment of a ball using a structured grid and computing its volume distribution. Using a spherical coordinate system, the modeling process generates discrete points within a hemispherical volume. The material properties of the ball are defined as $E = 200$ GPa, $\nu = 0.3$. The density parameter was increased to $\rho = 90534$ kg/m³ according to the whole ball value.

Figure 5.7 illustrates the computational model used to evaluate the flexural strength of the glass plate.

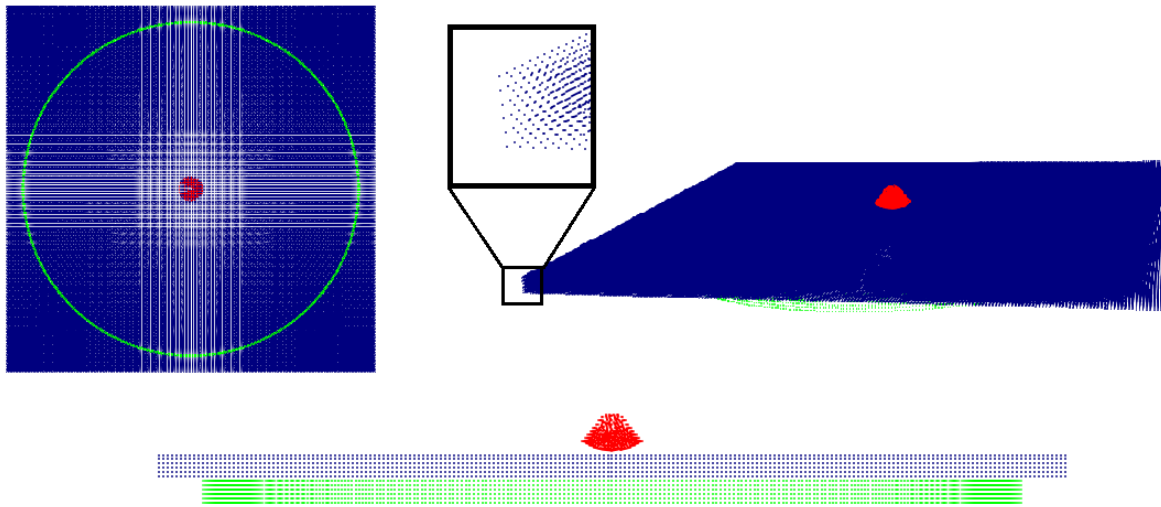


Figure 5.7: Peridynamic impact model

The critical stretch damage model was calculated with $s_c = 2.0 \cdot 10^{-3}$. The horizon size was set to 1.81 mm. A linear peridynamic solid (LPS) model was used to model the plate, support ring, and ball. The interactions at the contact surfaces between the ball, support ring, and the plate were governed by a short-range force model with a spring constant of $5 \cdot 10^{22}$ and a search and contact radius of 0.387 mm.

The time step addressed the transient dynamic phase, aimed at analyzing damage evolution and the dynamic phenomena associated with the formation and progression of damage patterns. Time integration was performed using an explicit time-stepping method based on the central difference scheme, which effectively approximates the second time derivative of the displacement vector.

Different initial velocities of the ball were applied (6, 9, 12, 15, 30 m/s). Figure 5.8 presents the damage distribution that reaches 100% on the bottom surface of the plate for a constant critical bond stretch value of $s_c = 2.0 \cdot 10^{-3}$.

Analyzing the obtained results, it can be seen that the critical time decreases as the initial velocity of the ball increases. Specifically, for an increase from $v = 6$ m/s to $v = 9$ m/s, the damage time is reduced by approximately 30%. A further increase from $v = 9$ m/s to $v = 12$ m/s, results in a significant reduction of approximately 85%. When the velocity increases from $v = 12$ m/s to $v = 15$ m/s, the time decreases by around 55%. The transition from $v = 15$ m/s and $v = 30$ m/s leads to an even more pronounced reduction of approximately 90%. These results indicate

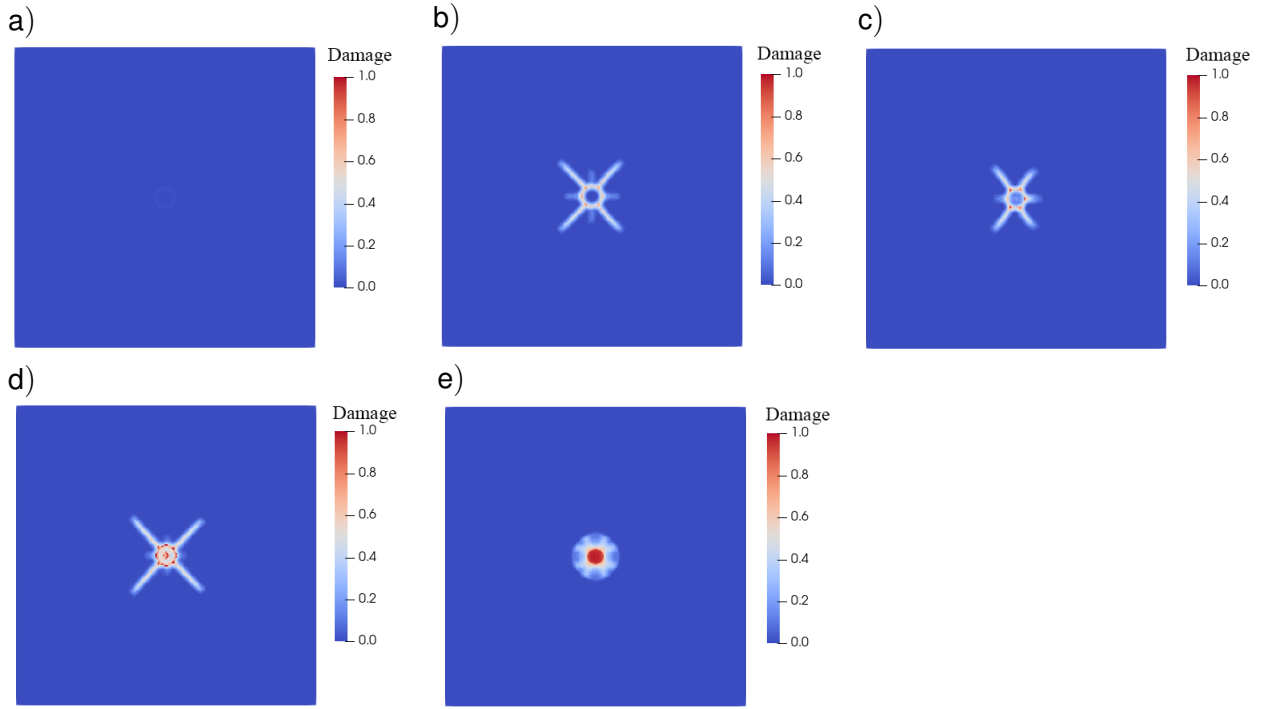


Figure 5.8: Damage distribution on the bottom side of a plate with different initial velocities of the ball.

a) $v = 6$ m/s at $t = 0.668$ ms, b) $v = 9$ m/s at $t = 0.476$ ms, c) $v = 12$ m/s at $t = 0.073$ ms, d) $v = 15$ m/s at $t = 0.034$ ms, e) $v = 30$ m/s at $t = 0.004$ ms

a nonlinear relationship between impact velocity and damage duration, suggesting that higher impact velocities lead to more abrupt structural failure.

Furthermore, examining the damage patterns reveals distinct fracture characteristics depending on the impact velocity. At the velocity 6 m/s, the damage circle occurs on the upper side of the plate at the area of impact of the ball with the plate, and a slightly visible circle pattern is formed in the lower part of the plate. As the velocity increases to 9 m/s and 12 m/s, the damage becomes more pronounced on the bottom side of the plate, forming a well-defined circular fracture from which symmetrical radial cracks propagate outward. At the velocity 15 m/s, the damage is localized in the center of the plate, forming a circle from which symmetrical radial cracks spread. The most extreme case, corresponding to 30 m/s, demonstrates that the damage is predominantly concentrated at the center of the bottom surface of the plate.

These observations indicate that as the impact velocity increases, the failure mode transitions from surface indentation and minor cracking to extensive radial fracture and, eventually, localized damage.

Expanding on the previous analysis of damage progression in the plate under impact loading with a fixed critical bond stretch, we now explore how varying the critical bond stretch parameter affects damage behavior for different velocities. By considering different values of s_c , we can assess its influence on the rate of damage evolution, the characteristics of crack propagation, and the overall failure mechanisms of the plate. The simulation employs a discretization with 6 nodes through the plate thickness and a horizon size of 1.81 mm.

In the following example, we examine the influence of a layer-dependent critical bond stretch (s_c) on the damage evolution in the plate under the initial ball velocity 6 m/s. The critical bond stretch is set to $1.0 \cdot 10^{-3}$ for the surface nodes of the bottom layer, while it is $2.0 \cdot 10^{-3}$ elsewhere within

the plate. The simulation results are shown in Figure 5.9.

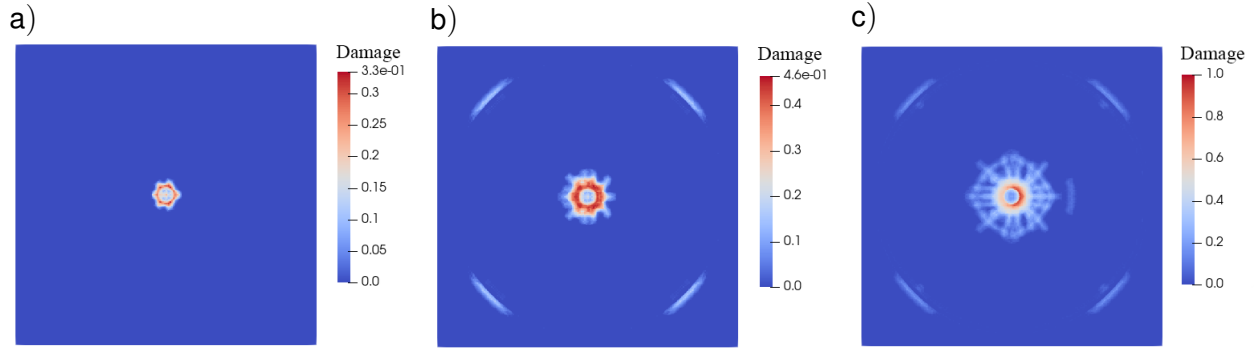


Figure 5.9: Damage distribution on the bottom side of a plate with $v = 6 \text{ m/s}$ and $s_c = 1.0 \cdot 10^{-3}$ at the surface nodes of bottom layer.

a) $t = 0.009 \text{ ms}$, b) $t = 0.156 \text{ ms}$, c) $t = 1.153 \text{ ms}$

The simulation results reveal that damage initiation occurs around $t = 0.009 \text{ ms}$. At this initial stage, the damage remains confined to the immediate vicinity of the impact site, forming a circular pattern that reflects the distribution of stress concentrations induced by the collision. As the damage propagates over time, till the damage reaches 100% at $t = 1.153 \text{ ms}$, radial cracks begin to emerge from the initially formed damage ring, extending outward in a symmetric manner. Concurrently, additional damage accumulates within the region enclosed by the support ring, suggesting the influence of boundary constraints on the fracture dynamics.

Compared to the model with $s_c = 2.0 \cdot 10^{-3}$ for the whole plate, the model with a lower s_c value at the bottom surface facilitates early damage initiation and forming of damage pattern over the bottom area. However, despite the earlier damage initiation, the critical time increases in this case. This effect can be attributed to the relatively moderate impact loading conditions, which do not induce an immediate catastrophic failure but allow for a more gradual damage progression. The spatial variation in s_c thus introduces competition between early-stage fracture initiation and the overall rate of damage propagation, ultimately influencing the plate's structural response and failure characteristics.

In the following calculation, the initial ball velocity is set to 9 m/s with the critical bond stretch $1.0 \cdot 10^{-3}$ for the surface nodes of the bottom layer, while it is $2.0 \cdot 10^{-3}$ elsewhere within the plate. The simulation results are shown in Figure 5.10.

In this case, the damage initiation occurs around $t = 0.005 \text{ ms}$. At this initial stage, the damage is a bit more localized in the center of the plate, as in the previous case, forming a circular pattern. As the damage propagates over time, the damage reaches 100% at $t = 0.389 \text{ ms}$, much faster than under 6 m/s . More radial cracks are observed that emerge from the initially formed damage ring, extending outward in a symmetric manner. Additionally, more pronounced damage accumulates within the region enclosed by the support ring, suggesting that faster velocity and boundary constraints influence fracture dynamics.

Compared to the model with $s_c = 2.0 \cdot 10^{-3}$ for the whole plate, the model with a lower s_c value at the bottom surface has early damage initiation and propagation of damage pattern over the bottom area. Under the current velocity conditions, this modification reduces the critical time by approximately 20%. This suggests that initial velocity and localized variations in the bond stretch parameter significantly influence the rate of damage progression, potentially altering the overall failure dynamics of the plate.

In the following examples, the effects of the initial ball velocities 12 m/s , 15 m/s and 30 m/s on the damage progression within the plate are examined (Figure 5.11). The critical bond stretch

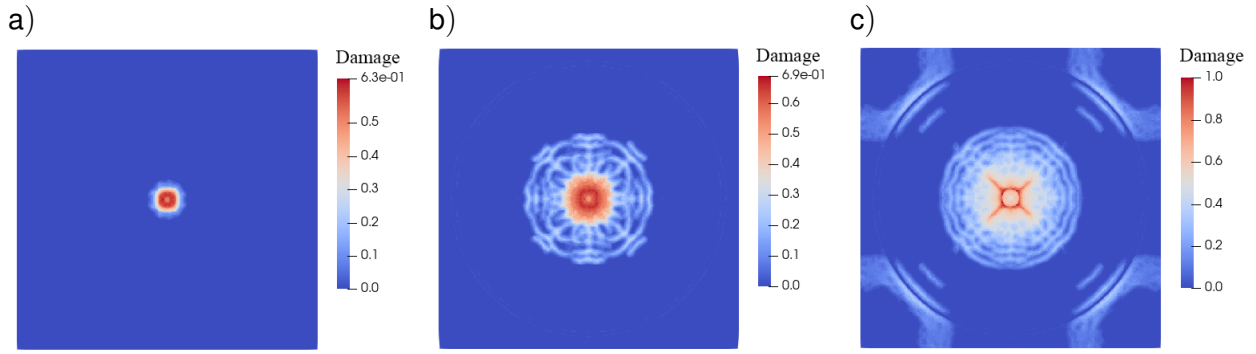


Figure 5.10: Damage distribution on the bottom side of a plate with $v = 9 \text{ m/s}$ and $s_c = 1.0 \cdot 10^{-3}$ at the surface nodes of bottom layer.

a) $t = 0.005 \text{ ms}$, b) $t = 0.142 \text{ ms}$, c) $t = 0.389 \text{ ms}$

stays $1.0 \cdot 10^{-3}$ for the surface nodes of the bottom layer, while it is $2.0 \cdot 10^{-3}$ elsewhere within the plate.

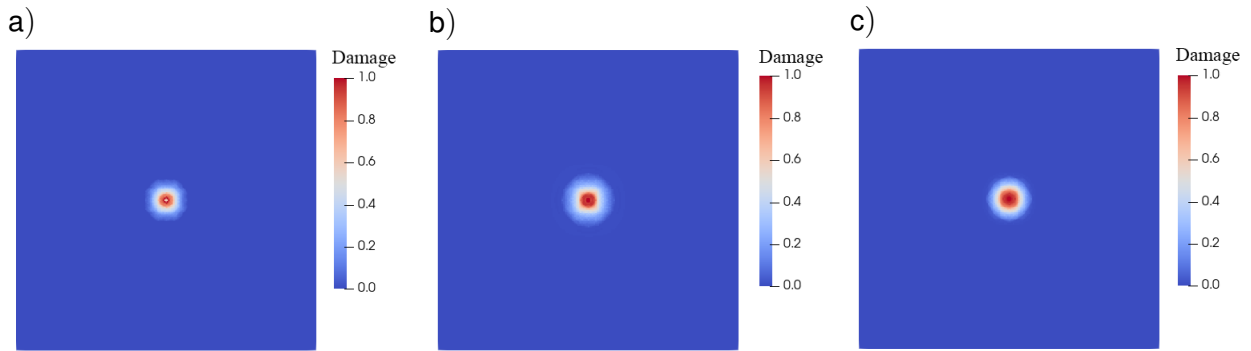


Figure 5.11: Damage distribution on the bottom side of a plate with different initial velocities of the ball.

a) $v = 12 \text{ m/s}$ at $t = 0.004 \text{ ms}$, b) $v = 15 \text{ m/s}$ at $t = 0.004 \text{ ms}$, c) $v = 30 \text{ m/s}$ at $t = 0.002 \text{ ms}$

The simulation results indicate that with this reduced critical bond stretch parameter at the bottom surface, damage accumulation progresses rapidly under high-velocity impact conditions. Notably, for the investigated high-velocity cases, the damage occurs localized at the bottom under the impact area and reaches 100% within a very short time frame, suggesting that the critical time remains approximately constant across these conditions. This observation implies that, beyond a certain velocity threshold, the structural integrity of the plate is compromised almost instantaneously, leading to a similar failure response regardless of further increases in impact velocity.

Further, we will consider the cases with the effects of varying initial ball velocities with lowered critical bond stretch $0.5 \cdot 10^{-3}$ for the surface nodes of the bottom layer, while it is $2.0 \cdot 10^{-3}$ elsewhere within the plate.

The first initial velocity is set to 6 m/s , and the results are shown in Figure 5.12.

The simulation results show that damage initiation occurs around $t = 0.009 \text{ ms}$, as in the previous case with lowered critical stretch. The damage is more localized in the impact area at this initial stage. As the damage propagates over time, till the damage reaches 100% at $t = 2.3 \text{ ms}$, the damage pattern spreads through the whole bottom layer area. In the model with the lowest

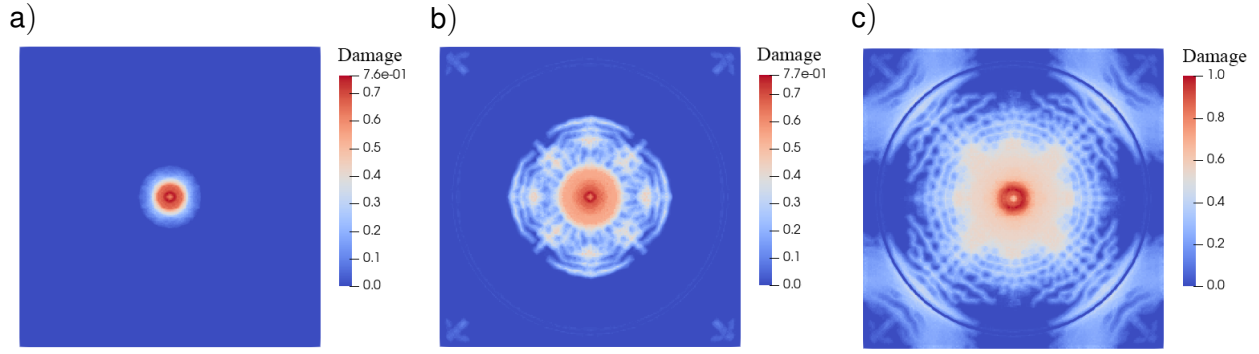


Figure 5.12: Damage distribution on the bottom side of a plate with $v = 6 \text{ m/s}$ and $s_c = 0.5 \cdot 10^{-3}$ at the surface nodes of bottom layer.

a) $t = 0.009 \text{ ms}$, b) $t = 0.1 \text{ ms}$, c) $t = 2.3 \text{ ms}$

s_c value, the critical time increases even more in this specific case than in previous cases. The second initial velocity is set to 9 m/s , and the results are shown in Figure 5.13.

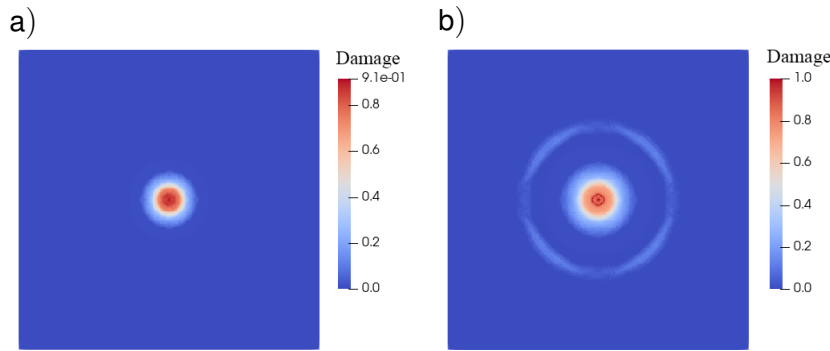


Figure 5.13: Damage distribution on the bottom side of a plate with $v = 9 \text{ m/s}$ and $s_c = 0.5 \cdot 10^{-3}$ at the surface nodes of bottom layer.

a) $t = 0.005 \text{ ms}$, b) $t = 0.009 \text{ ms}$

In this case, the damage initiation is localized in the center of the plate bottom area and occurs around $t = 0.005 \text{ ms}$, as well as in the previous case with lowered critical stretch. The damage reaches 100% very fast, and the damage pattern is concentrated primarily close to the impact zone.

In the following cases, the influence of varying initial ball velocities 12 m/s , 15 m/s and 30 m/s on the damage evolution within the plate is systematically examined. As anticipated, the simulation results demonstrate that under high-velocity impact conditions, damage accumulation progresses rapidly when a reduced critical bond stretch parameter is applied to the bottom surface. This behavior is consistent with previous findings involving a lowered critical bond stretch, reinforcing that localized reductions in material fracture resistance significantly accelerate failure initiation and propagation.

Furthermore, a comparative analysis reveals that the critical time for complete failure exhibits a slight reduction relative to the scenario in which the critical bond stretch was uniformly lowered to $1.0 \cdot 10^{-3}$ for the surface nodes of the bottom layer. This decrease in critical time suggests that while the primary fracture characteristics remain consistent, subtle variations in the spatial distribution of the critical bond stretch parameter can influence the temporal dynamics of damage progression. These findings highlight the sensitivity of structural failure to variations in material

properties and emphasize the importance of considering spatially dependent fracture criteria when modeling impact-induced damage in brittle materials.

The summarized data is shown in Figure 5.14.

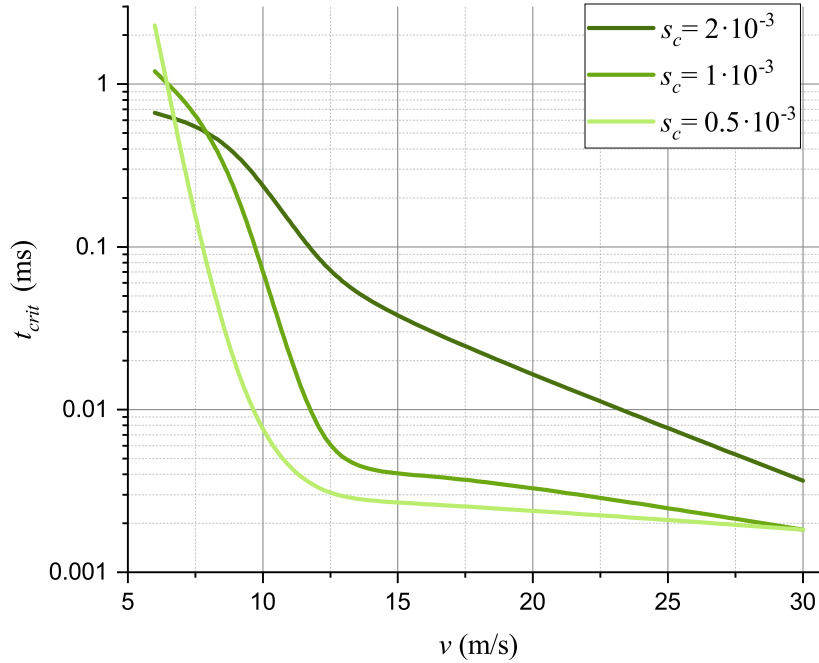


Figure 5.14: Dependence of critical time on the initial velocity if the ball with different s_c values

The results indicate that materials with lower critical bond stretch values fail more rapidly under impact loading, with the difference being most pronounced at lower velocities. However, at higher impact velocities, failure occurs almost instantaneously for all cases, suggesting a velocity threshold beyond which material properties play a diminished role in determining failure time.

Additionally, we test the influence of the low initial ball velocity 3 m/s on the damage progression within the plate. The analysis uses a layer-dependent critical bond stretch, considering different values of s_c to evaluate its influence on fracture initiation and propagation. The corresponding simulation results are presented in Figure 5.15.

The results indicate that the structural response depends on the critical bond stretch distribution at such a low impact velocity. For $2.0 \cdot 10^{-3}$, uniformly applied to the entire plate, no damage is observed, indicating that an initial velocity of 3 m/s is insufficient to initiate fracture. For $s_c = 1.0 \cdot 10^{-3}$, applied to the surface nodes of the bottom layer, crack initiation is detected at the lower surface of the plate within the impact zone. However, damage evolution is limited, reaching a maximum of 33% by 1.0 ms. The absence of further propagation suggests that the energy dissipation mechanisms at this velocity prevent the formation of a fully developed fracture network. For $s_c = 0.5 \cdot 10^{-3}$, applied to the surface nodes of the bottom layer, a more pronounced damage evolution is observed. Initial damage appears in the impact zone and subsequently spreads along the lower surface of the plate. The damage reaches 70% by 3.4 ms, at which point it ceases to progress further. This suggests that while material weakening facilitates increased crack propagation, impact velocity remains a governing factor in determining whether a complete structural failure occurs.

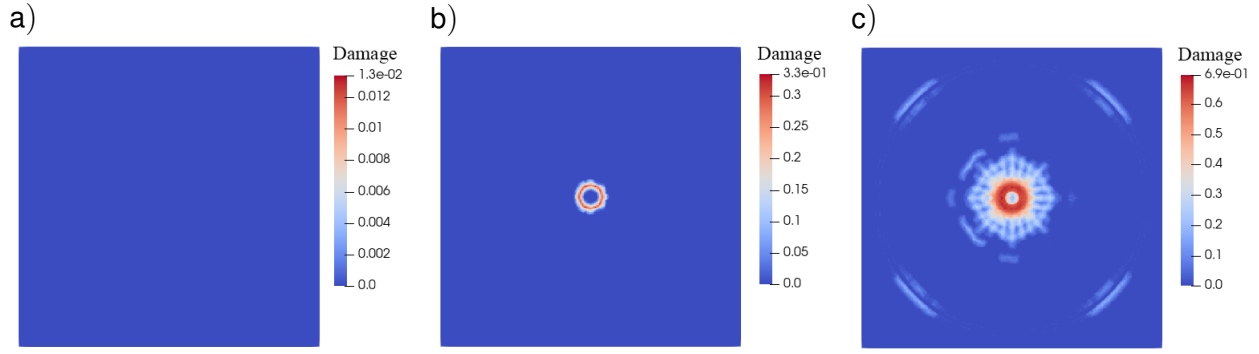


Figure 5.15: Damage distribution on the bottom side of a plate with $v = 3$ m/s and different critical stretch values.

a) $s_c = 2.0 \cdot 10^{-3}$ at $t = 3.5$ ms, b) $s_c = 1.0 \cdot 10^{-3}$ for the surface nodes of the bottom layer at $t = 1.0$ ms, c) $s_c = 0.5 \cdot 10^{-3}$ for the surface nodes of the bottom layer at $t = 3.4$ ms

In all cases where damage initiation occurred, fracture progression halted at a certain percentage, indicating that energy dissipation mechanisms dominate under low-velocity impacts, preventing complete failure. This contrasts with high-velocity scenarios where damage rapidly reaches 100% due to overwhelming impact forces.

These results highlight the importance of considering both material properties and loading conditions when assessing the fracture behavior of brittle structures. These findings highlight the importance of considering impact velocity and critical bond stretch when considering structures' fracture resistance subjected to dynamic loading conditions.

5.3 Influence of initial defects (flaws) on fracture force, damage and crack patterns

At the beginning of this chapter, the two approaches for defining critical bond stretch were introduced. In the current section, the second approach will be described, returning to the model with quasi-static loading. This approach considers s_c for the initially micro-cracked model (flaws, etc.). In numerous studies on PD fracture analysis, such as [35, 45], the following formula for s_c is commonly recommended

$$s_c = \sqrt{\frac{G_c}{\{3G + (3/4)^4[K - (5G/3)]\} \delta}}, \quad (5.4)$$

where G_c is the Griffith critical energy release rate, K is fracture toughness.

To derive Equation 5.4, the work required to create a new unit surface by eliminating bond interactions is calculated and equated to G_c . This approach provides a direct relationship between the energy release rate and the critical bond stretch, enabling the determination of the critical value of work on a bond [84] and, subsequently, the critical bond stretch. In fracture mechanics, G_c is typically computed from the fracture toughness value K_{Ic} , which is experimentally obtained from laboratory crack-tip opening tests conducted on homogeneous specimens containing relatively long macroscopic cracks. For float glass, the mean fracture toughness is reported as $K_{Ic} = 0.76$ MPa $m^{1/2}$ [38]. Using this value and applying the plane stress assumption, the critical energy re-

lease rate for float glass is estimated as $G_c = 8.25 \text{ Jm}^2$. To calculate the critical bond stretch s_c , additional material properties are incorporated, including Young's modulus $E = 70 \text{ GPa}$, Poisson ratio $\nu = 0.22$. Substituting these values into Equation 5.4, s_c is expressed as a function of the horizon size δ , reflecting the non-local interaction range in peridynamic theory. For $\delta = 1 \text{ mm}$, the critical bond stretch is calculated as $s_c = 3.12 \cdot 10^{-4}$. For a smaller horizon size of $\delta = 0.1 \text{ mm}$, s_c increases to $s_c = 9.8 \cdot 10^{-4}$ [53]. This demonstrates that s_c is inversely proportional to the horizon size, as a smaller δ results in fewer bonds contributing to the critical energy release, necessitating a higher s_c to match the fracture energy. These calculations illustrate the sensitivity of the critical bond stretch to the chosen horizon size and highlight the importance of accurately choosing s_c within the peridynamic framework to ensure consistency with experimental observations and material behavior. By linking s_c to fundamental material properties such as G_c and K_{Ic} , this derivation provides a basis for determining the critical bond stretch, enabling the peridynamic model to effectively capture fracture initiation and propagation in brittle materials like a float glass.

Based on the previous discussions on the influence of critical bond stretch and its effect on damage initiation and propagation, we would like to focus on modeling initial defects (flaws) in the glass plate using peridynamic theory. In real-world scenarios, float glass and similar brittle materials often contain microscopic imperfections introduced during manufacturing. These imperfections, referred to as defects, weaken the material's localized regions and influence damage initiation and evolution. To effectively capture these phenomena in the peridynamic framework, initial defects are modeled by reducing the critical bond stretch value at specific peridynamic nodes. The primary objective of this section is to analyze how initial flaws influence the fracture behavior of a float glass plate under quasi-static loading conditions. By introducing defects via reduced s_c , we aim to study the impact of defect size and distribution on crack initiation and propagation, understand how localized weakening affects the overall damage patterns and failure times, compare the behavior of flawed materials to that of defect-free models to highlight the critical role of imperfections.

Figure 5.16 illustrates the concept of incorporating initial flaws into the peridynamic model by reducing s_c of individual or groups of nodes.

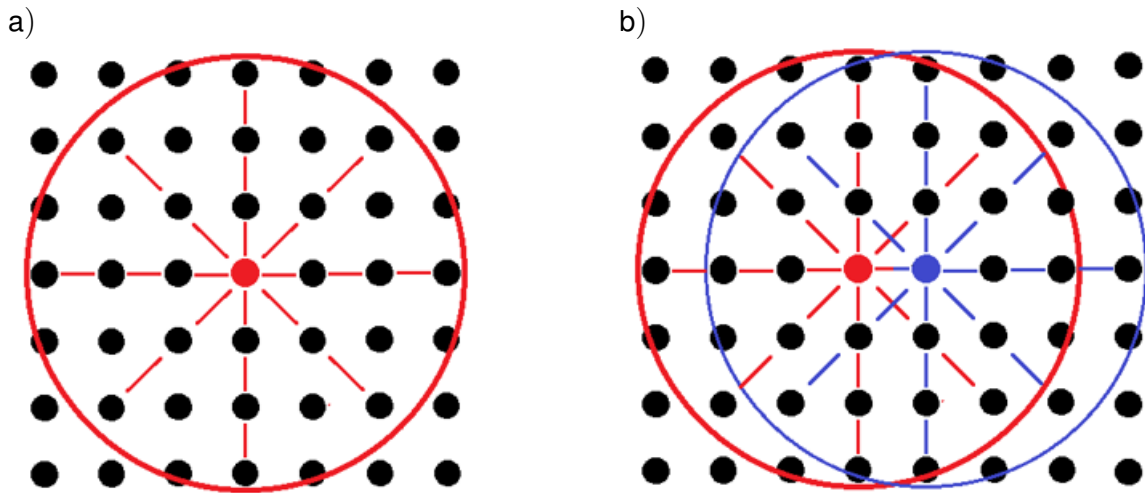


Figure 5.16: Modeling of initial defects with Peridynamics.

a) 1 node, b) 2 nodes

In peridynamics, each node interacts with its neighbors within a defined horizon radius. This allows for seamless modeling of discontinuities, such as cracks or defects, without additional

criteria. By reducing s_c in specific nodes, we introduce localized weakening, consistent with the effects of imperfections in authentic materials. The number of nodes with reduced s_c determines the size and extent of the defect, allowing for the simulation of minor flaws or more extensive regions of weakness. Weakening bonds within a defect's horizon reflect the stress amplification and failure mechanisms that arise from imperfections under loading.

Figure 5.16 a) shows a single peridynamic node is assigned a reduced s_c value to simulate the presence of an initial defect. The red circle denotes the horizon radius of the weakened node, which defines the family of neighboring nodes that interact with the central defect node through peridynamic bonds. The weakening of s_c at this node results in all bonds within its horizon being weakened proportionally, as the reduced s_c applies to all the associated bonds. This simulates a localized flaw, where the bonds are more prone to failure under applied stress. In Figure 5.16 b), multiple nodes are designated with reduced s_c values, representing a cluster of initial defects or a more significant flaw. Each node, represented in red or blue, has its horizon radius, illustrated by overlapping circles. When the critical bond stretch is reduced at multiple nodes, all bonds within their respective horizons are weakened. This creates a broader weakened region, modeling the material's more significant imperfection or defect cluster.

We now examine the influence of a single imperfection node on the fracture behavior of a glass plate. Figure 5.17 illustrates the simulation results for a plate with a single defect node positioned in the bottom layer under the load ring. The critical bond stretch for this node is set to $s_c = 1.0 \cdot 10^{-4}$, while the remaining nodes in the plate have a uniform $s_c = 2.0 \cdot 10^{-3}$.

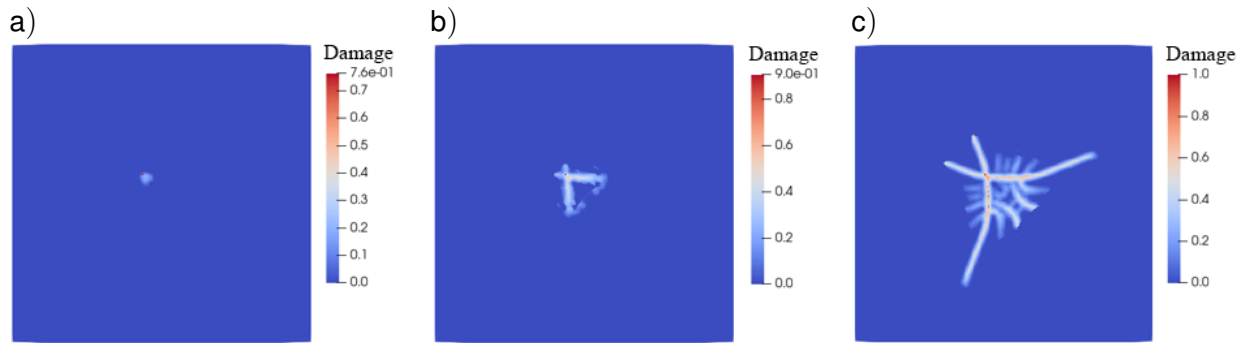


Figure 5.17: Damage distribution on the bottom side of a plate with 1 defect node under the load ring.

a) $t = 51.9504$ s, b) $t = 51.9504$ s + 0.1 ms, c) $t = 51.9504$ s + 0.7 ms

The damage initiates at the imperfection node with reduced s_c , which is the focus point for failure. The localized reduction in s_c at the imperfection node leads to early damage initiation. The defect acts as a stress concentrator, amplifying the local stress and causing bonds in its horizon to fail before any other region of the plate at the initial stage of loading. The damage, starts from 51.9504 s point, quickly spreads from this node to the surrounding area, forming a localized damage zone under the load ring. The weakening of bonds in the defect's horizon accelerates this initial phase of damage propagation. The damage expands significantly, reaching the region directly under the load ring. Radial cracks spread symmetrically through the plate, emanating from the load ring radius area and extending toward the edges of the plate, reflecting the stress redistribution as more bonds fail within the defect's influence radius. The damage progresses to full failure within 0.7 ms reaching 100% damage. This underscores the importance of even a single defect in influencing the overall failure time and pattern.

In the next case simulation (Figure 5.18), two neighboring imperfection nodes are introduced in the bottom layer under the load ring. The s_c for these nodes is set to $1.0 \cdot 10^{-4}$, while the rest

of the plate retains $s_c = 2.0 \cdot 10^{-3}$. This adjustment creates a slightly larger defective region, allowing us to observe the impact of multiple initial flaws on damage progression and failure dynamics.

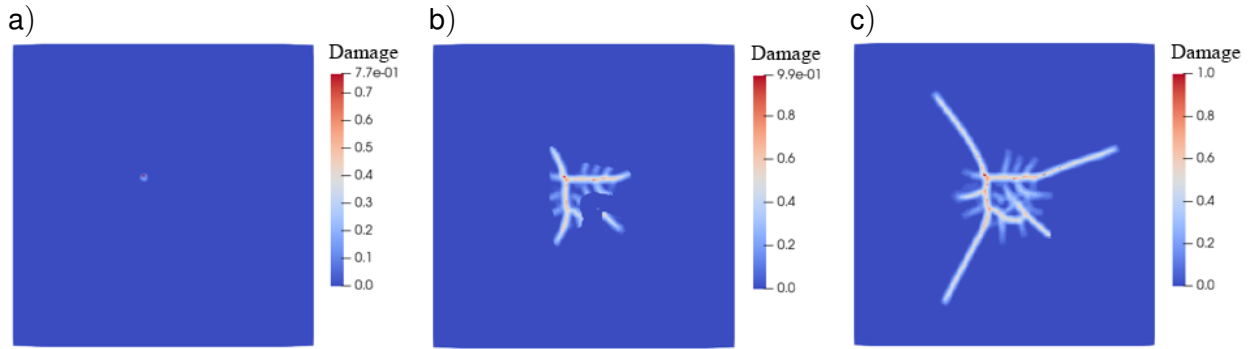


Figure 5.18: Damage distribution on the bottom side of a plate with 2 defect nodes under the load ring.

a) $t = 51.0916$ s, b) $t = 51.0916$ s + 0.3 ms, c) $t = 51.0916$ s + 1.5 ms

Like the single-node case, the damage starts in the imperfection nodes, forming a localized zone under the load ring. The damage then grows outward, eventually spreading to the load ring radius and generating radial cracks that extend through the plate. In this case, the total time to reach 100% damage takes 1.5 ms. The critical time for this case is 2.65% shorter than in the single-node scenario, reflecting the faster damage initiation due to the larger defective region. The two imperfection nodes act as dual stress concentrators, amplifying local damage initiation and propagation.

The next case describes four imperfection nodes introduced in the bottom layer under the load ring (Figure 5.19). These nodes are arranged in a square configuration (two side-by-side and two directly under them). As in previous cases, the critical bond stretch for these defect nodes is set to $1.0 \cdot 10^{-4}$, while the remaining plate maintains $s_c = 2.0 \cdot 10^{-3}$.

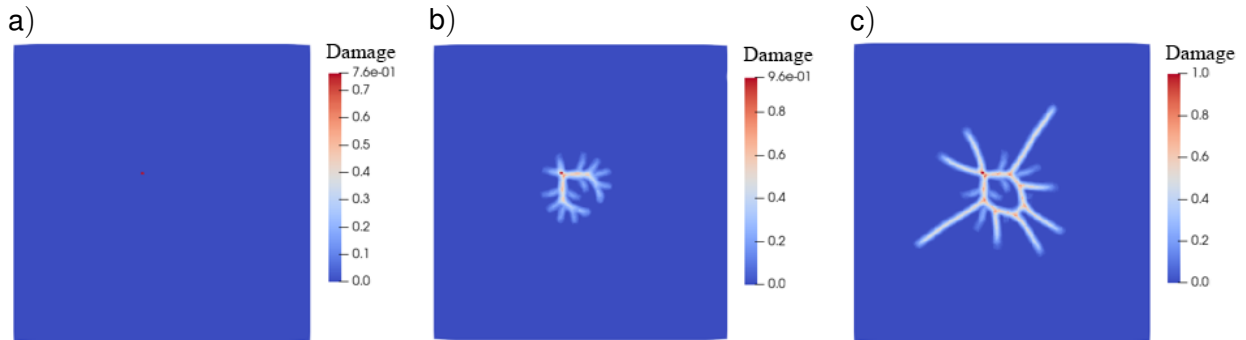


Figure 5.19: Damage distribution on the bottom side of a plate with 4 defect nodes under the load ring.

a) $t = 48.0097$ s, b) $t = 48.0097$ s + 0.3 ms, c) $t = 48.0097$ s + 1.2 ms

Similar to the previous cases, the damage starts in the defect nodes. However, the initial damage zone is larger and more concentrated with four imperfection nodes, leading to faster stress redistribution. Damage initiates within the defect nodes, forming a localized circle-shaped damage zone under the load ring, and propagates outward, forming radial cracks that extend through the

plate in a symmetrical pattern. The symmetry of the cracks reflects the uniform material properties outside the defect region. The time required for the plate to reach 100% damage is 1.5 ms. The critical time is reduced by 6% compared to the two-node case. This reduction highlights the influence of a larger defective region on accelerating damage initiation.

Now, we investigate the effects of defect location and size on the fracture behavior of the plate. The calculations consider defects placed in three distinct locations in the bottom layer of the plate:

- Center of the plate;
- Under the load ring;
- Out of the load ring region.

The analysis includes configurations with one, two, and four damaged nodes (nodes with reduced s_c). The results are shown for 100% damage and focus on the critical time and the corresponding critical force needed for failure.

Figure 5.20 presents a summarised dependence of critical time and critical force on the number of nodes (n^*) with reduced critical bond stretch ($s_c = 1.0 \cdot 10^{-4}$) placed at different locations in the bottom layer of the plate. The rest of the nodes in the plate retain a uniform critical bond stretch of $2.0 \cdot 10^{-3}$.

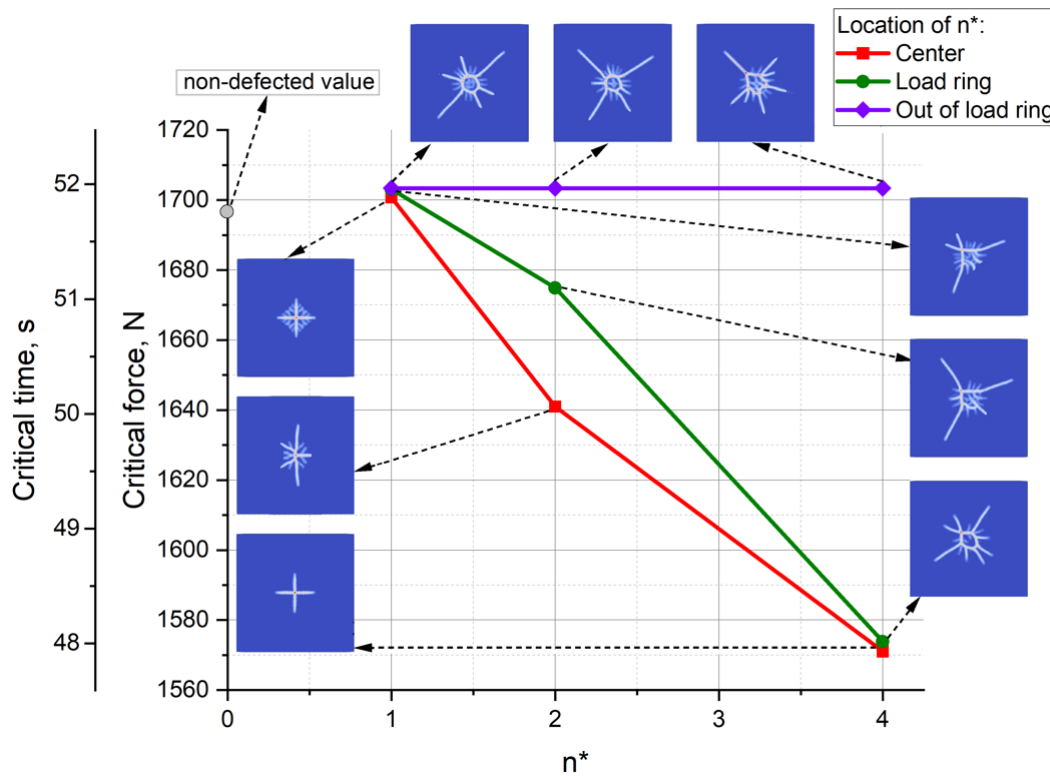


Figure 5.20: Dependence of critical time/force on the number of nodes with attached low critical stretch bonds

The red curve corresponds to defects located at the center bottom layer of the plate. As the number of defect nodes increases from 1 to 4, the critical time/force decreases significantly. From a single damaged node to two nodes, the critical time is approximately 3.5% less, and from two to four damaged nodes is around 4.3%. The resulting damage patterns are influenced by the initial imperfections, with varying degrees of symmetry and crack propagation behavior. In the case of

a single node located precisely at the center of the plate, damage initiation occurs at this node and radiates symmetrically outward. The stress concentration at the central defect node triggers bond failures within its horizon radius, forming a cross-like damage pattern. The symmetry of the crack development is preserved due to the perfect central placement of the defect, which ensures equal stress distribution in all directions. Radial cracks extend evenly outward from the center, creating a balanced and predictable damage progression. For the two-node case, one node is positioned precisely at the center of the plate, while the second node is slightly displaced. Damage initiation still starts at the center due to the higher stress concentration at this location. However, as the failure propagates, the symmetry of the pattern is disrupted. The displacement of the second node introduces an asymmetry in the stress field, causing the damage to spread unevenly. Instead of the perfectly crosswise pattern observed in the single-node case, cracks propagate preferentially toward the direction of the displaced node. This creates a skewed or unbalanced crack distribution that highlights the sensitivity of the damage pattern to the defect arrangement. In the four-node case, the defective nodes are arranged around the center, forming a square-like configuration. Damage initiation co-occurs at the defective nodes due to their equal stress concentration. From these points, the damage propagates crosswise and symmetrically outward. The resulting crack pattern is characterized by well-defined radial cracks that spread evenly in all directions. The presence of multiple nodes accelerates damage initiation and stress redistribution, leading to a broader and more uniform failure zone. The symmetrical placement of the four nodes reinforces the balance in the crack propagation paths, preserving the overall symmetry of the damage pattern.

The green curve shows the results for defects positioned under the load ring. The detailed description was already done above. Summarising the data, increasing the number of defective nodes reduces the critical time/force. Compared to the center location, the reduction is less pronounced as the stress concentration under the load ring accelerates damage initiation, minimizing the additional impact of multiple defects.

The purple curve represents defects outside the load ring (the place is $5/4$ radius of the load ring from the middle of the plate). In this case, the results show no change in the critical time/force with an increasing number of defect nodes. The location of these nodes in a lower stress region prevents them from influencing the damage progression significantly, regardless of defect size. The damage evolution for nodes placed out of the load ring exhibits distinct behaviors depending on the number of defective nodes. While these nodes are located in low-stress regions of the plate, their influence on the crack pattern changes as the defect size (number of nodes) increases. In the case of a single defective node, the damage initiation is unaffected by the weakened node. Damage initiation starts inside the load ring radius, where the stress concentration is naturally the highest. This leads to the formation of a ring-shaped damage zone inside the load ring. From this ring-shaped zone, radial cracks propagate symmetrically outward toward the edges of the plate. The weak node outside the load ring does not influence the crack propagation. It remains isolated from the primary damage zone, as the stress distribution in the out-of-load ring region is too low to trigger further failures. For the two-node case, nodes are positioned outside the load ring in relative nearness. Damage initiation still begins inside the load ring, where the stress concentration is highest, leading to the formation of the ring-shaped damage zone. As the radial cracks grow outward, one of the radial cracks intersects the position of the weakened nodes. Unlike the single-node case, the presence of two nodes influences the crack propagation path. One of the radial cracks passes directly through the defective nodes, integrating them into the overall damage progression. This interaction between the radial crack and the weakened nodes demonstrates the influence of defect size on crack path development, even in low-stress regions. When four defective nodes are placed outside the load ring, the damage initiation and propagation behavior change significantly. Unlike the previous cases, damage initiation does not start

exclusively inside the load ring. Instead, it begins at the positions of the four defective nodes. The stress redistribution caused by the weakened bonds at these nodes triggers early failure in the out-of-load ring region. From the defective nodes, damage propagates inward, creating a circular damage zone that intersects with the load ring radius. Radial cracks then extend symmetrically outward from this circular damage zone, following the stress redistribution pattern. Multiple defective nodes outside the load ring alter the standard damage progression observed in previous cases, highlighting their influence on crack initiation and the formation of the damage zone.

The value pointed as a non-defected value in Figure 5.20 represents the critical time/force value for the model without any defective nodes, corresponding to a pure glass configuration. For the non-defected value, compared to defects placed at the center of the plate, under the load ring, and out of the load ring, the results for one defective node closely aligned with the non-defected value. This similarity indicates that defects in this region do not influence the fracture behavior. The results slightly deviate from the non-defected value, and this discrepancy can be attributed to numerical error, as the location of the small defect remains largely irrelevant to damage initiation and propagation.

This analysis highlights the importance of defect size and location in determining the fracture response of float glass. Central and load ring defects pose the most significant risk, while defects in less stressed regions have a negligible effect. These findings further validate the peridynamic approach for modeling realistic flaws and provide insight into the critical role of defect placement in glass structures.

We now extend this analysis by introducing lowered critical bond stretch values for the surface nodes of the bottom layer combined with a single defective node under the load ring. This scenario evaluates the combined effects of surface weakening and localized defects on damage initiation and crack propagation.

Figure 5.21 presents the simulation results for a plate with a one-node defect located under the load ring, with $s_c = 1.0 \cdot 10^{-4}$ and lowered critical bond stretch for the surface nodes of the bottom layer, set to $s_c = 0.75 \cdot 10^{-3}$, and elsewhere in the plate uniform critical bond stretch is $s_c = 2.0 \cdot 10^{-3}$.

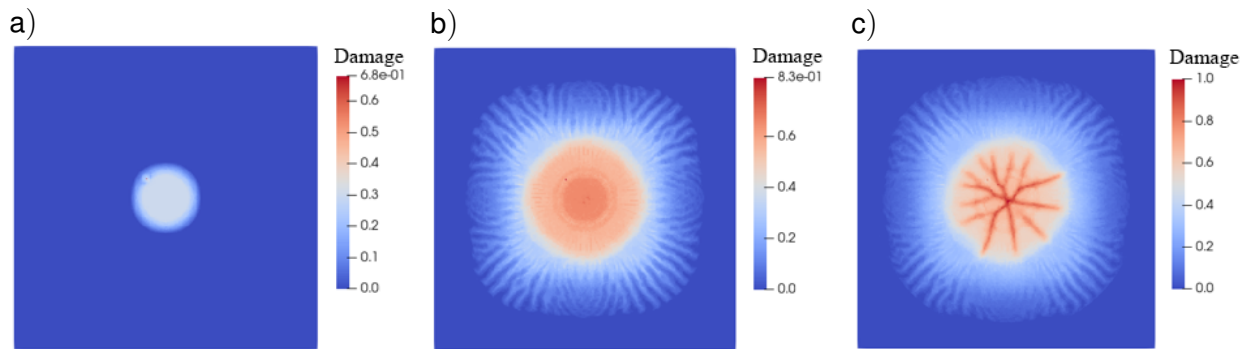


Figure 5.21: Damage distribution on the bottom side of a plate with 1 defect node under the load ring with $s_c = 0.75 \cdot 10^{-3}$ at the surface nodes of bottom layer.

a) $t = 34.0$ s, b) $t = 34.0$ s + 7.7 ms, c) $t = 34.0$ s + 8.1 ms

At the early stage, damage emerges in the damaged node. Then, the manifestation of damage appears within the region under the load ring with the highest stress concentration. A circular damage zone begins to form around the load ring radius, with no influence observed from the isolated defective node itself. The circular damage zone intensifies and expands outward symmetrically. The influence of the reduced surface nodes becomes more apparent as the weakened bonds facilitate faster crack progression. The single defective node under the load ring, while sig-

nificant for initiating damage, does not alter the propagation paths of the cracks. In contrast to the previous cases with a single defect under the load ring and no lowered surface nodes, the damage patterns here exhibit radial cracks propagating through the center of the plate to its edges when the plate reaches full damage. The defective node itself does not directly influence the crack paths or final damage pattern, as the reduced surface nodes dominate the overall behavior of the plate. In comparison to the model without lowered surface nodes, the damage initiation time is significantly reduced by 34.6%. This reduction is due to the weakened bonds in the surface nodes, which accelerate bond failure and damage initiation under the applied load. The time required for the plate to reach 100% damage has increased from 0.7 ms (in the previous single-defect node case) to 8.1 ms. This extended damage propagation time results from the reduced surface node strength, which allows cracks to develop more gradually and uniformly across the plate.

In the following case, we examine the influence of a four-node defect outside the load ring. The critical bond stretch in these nodes is set to $s_c = 1.0 \cdot 10^{-4}$, while the surface nodes of the bottom layer have a lowered bond stretch of $s_c = 0.75 \cdot 10^{-3}$, with $s_c = 2.0 \cdot 10^{-3}$ elsewhere in the plate (Figure 5.22).

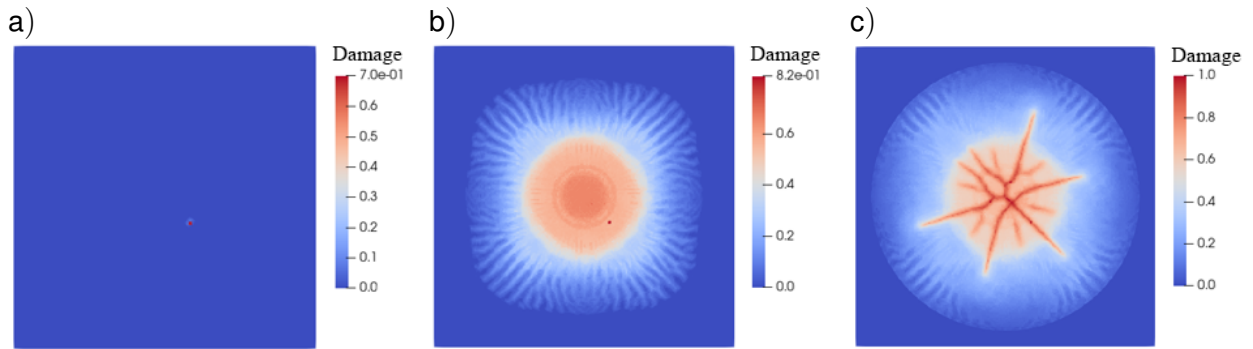


Figure 5.22: Damage distribution on the bottom side of a plate with 4 defect nodes under the load ring with $s_c = 0.75 \cdot 10^{-3}$ at the surface nodes of bottom layer.

a) $t = 27.2$ s, b) $t = 34.0$ s + 7.6 ms, c) $t = 34.0$ s + 8.5 ms

Damage initiates at the weakened nodes outside the load ring due to their significantly reduced critical bond stretch. The location of the defect serves as a stress concentrator, triggering early bond failures at the defective nodes despite their positioning in a relatively low-stress region. At this stage, damage remains localized around the defective nodes, with a small circular damage zone visible near the defect location. As the damage evolves, it propagates inward toward the load ring radius with higher stress concentration. A ring-shaped damage zone begins to form under the load ring, consistent with the typical fracture behavior observed in previous cases. Radial cracks started to form, extending from the plate center, a circular damage zone, toward the plate edges. The plate reaches full damage with a well-defined system of radial cracks. The presence of the four defective nodes influences the crack path, with one of the radial cracks passing directly through the damaged nodes, connecting the defect location to the primary crack pattern. While the defects accelerated the damage initiation process, the propagation of radial cracks largely follows the stress redistribution caused by the applied load. Compared to the model without reduced surface nodes, the damage initiation time decreases significantly by 29.2%. The reduced surface bond stretch accelerates bond failure and triggers earlier damage initiation. The time required for the plate to reach 100% damage increases from 1.2 ms (in the case without reduced surface nodes) to 8.5 ms. The extended propagation time is attributed to the interaction between the weakened surface nodes and the defect nodes, which results in a more gradual and uniform

crack development.

This analysis highlights the combined influence of localized defects and surface weakening on the damage behavior of the glass plate. The weakened surface layer accelerates damage initiation, reducing the critical time. These findings emphasize the importance of considering the placement and size of the defect and surface layer strength when evaluating the fracture behavior of brittle materials under loading conditions.

5.4 Comparison with experimental data

The aim of this section is to compare the results of numerical analysis with experimental data on ring bending tests published in [53]. A procedure to identify the critical bond stretch from experimental data will be discussed. Then, different cases of damage patterns will be analyzed, including the quasi-homogeneous plate (case 1), the plate with initial imperfection inside the load ring radius (case 2), and the plate with initial imperfection outside the load ring radius.

5.4.1 Damage initiation modeling

The key step in PD fracture analysis is to define and calibrate the damage initiation criterion. For the damage model applied in this work, the critical bond stretch s_c must be identified from experimental data. To estimate the value of s_c , let us apply the strength distribution data from ring bending tests.

Figures 5.23 a) and b) show the top and bottom sides of the plate subjected to double-ring bending. The thickness distribution of the radial displacement u_r in the region inside the load ring radius is illustrated in Fig. 5.23 c). Any element of the plate face layer on the bottom side is subjected to an equibiaxial stress state, as shown in Figure 5.23 d).

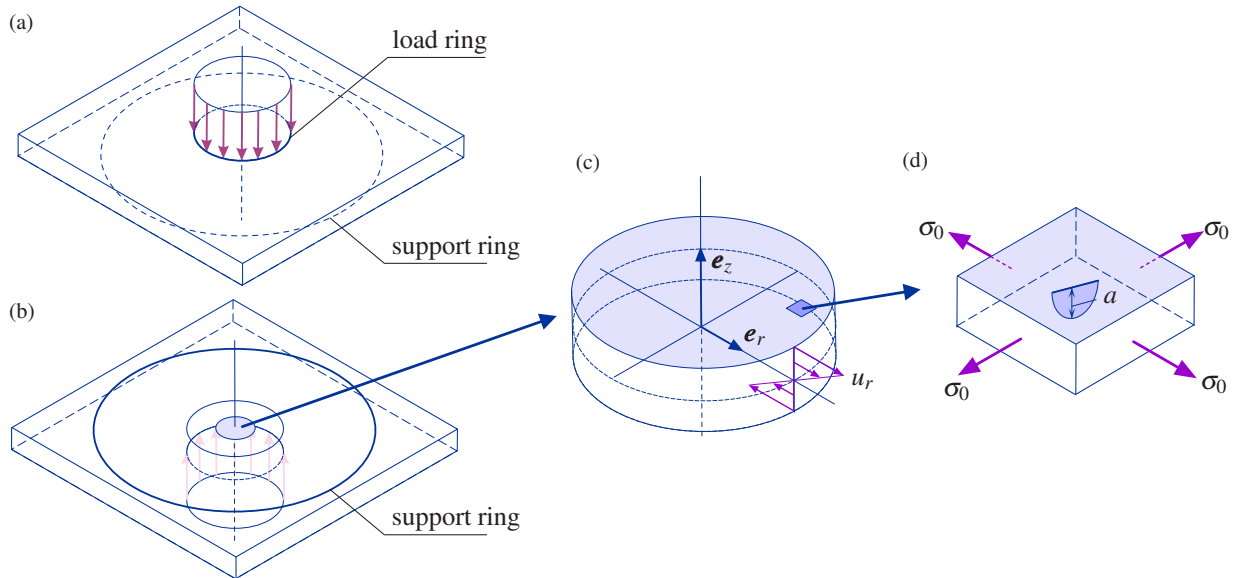


Figure 5.23: Loading configuration, strain and stress states in a plate under ring bending.

a) Top view, b) bottom view, c) region inside load ring radius, d) semi-circular surface flaw in under equibiaxial stress

To derive Equation (5.4), the work required to create a new unit surface by removing the bond interactions is computed using the linear peridynamic solid model. By equating this work to the

critical energy release rate G_c , Equation (5.4) is obtained. The critical energy release rate G_c is computed from the fracture toughness value K_{Ic} , which is obtained from laboratory crack-tip opening tests on homogeneous specimens with pre-cracks, such as single-edged pre-cracked beam [65]. Thus, Equation (5.4) can be applied to PD analysis of crack propagation.

As discussed in numerous studies, fracture in glass initiates from surface flaws with a length in the micrometer range. To roughly estimate this range, assume that a semi-circular crack with the radius a_{crack} (shown as a in Figure 5.23 d)) is located in the tensile layer of the plate inside the load ring radius. According to [94], the number of flaws detected on a glass plate surface usually ranges from 1 to 8 in the area of 1 cm^2 . Thus, it can be assumed that the flaws do not influence each other. Following [87] the stress intensity factor K_I for the configuration shown in Figure 5.23 d) is determined as follows

$$K_I = 1.14 \frac{2}{\sqrt{\pi}} \sqrt{a} \sigma_I,$$

where $\sigma_I = \sigma_r = \sigma_\varphi = \sigma_0$ is the first principal stress.

According to Kirchhoff plate theory, the part of the plate inside the load ring radius is subjected to uniform bending with the radial M_r and circumferential M_φ bending moments given by

$$M_r = M_\varphi = \frac{F_{\text{res}}}{8\pi} \left[(1 - \nu) \frac{r_{sr}^2 - r_{lr}^2}{R^2} + 2(1 + \nu) \ln \frac{r_{sr}}{r_{lr}} \right] \quad (5.5)$$

The corresponding stress state at the bottom plate face, opposed to the load ring, is equibiaxial and uniform. The maximum radial σ_r and circumferential σ_φ components of the stress tensor are

$$\sigma_{r_{\text{max}}} = \sigma_{\varphi_{\text{max}}} = \sigma_{\text{max}} = \frac{3F_{\text{res}}}{4\pi h^2} \left[(1 - \nu) \frac{r_{sr}^2 - r_{lr}^2}{R^2} + 2(1 + \nu) \ln \frac{r_{sr}}{r_{lr}} \right] \quad (5.6)$$

With $K_{Ic} = 0.76 \text{ MPa m}^{1/2}$ [38] and the lower and upper bounds of fracture stress from co-axial ring bending tests $\sigma_{I_l} = 99.7 \text{ MPa}$ and $\sigma_{I_u} = 228 \text{ MPa}$, see [53], the mode I fracture criterion

$$K_I \leq K_{Ic}$$

yields the flaw sizes of $a_{\text{min}} = 6.7 \text{ }\mu\text{m}$ and $a_{\text{max}} = 35 \text{ }\mu\text{m}$.

For the PD analysis of crack initiation in a plate, resolving such small cracks in the numerical model is not feasible, if not impossible. Furthermore, the length of surface flaws in float glass is not deterministic but follows a statistical distribution due to the stochastic nature of glass production, handling, and environmental exposure. Given the assumed distribution of flaw length, orientation, and density, fracture mechanics criteria can be applied to individual flaws, and a Monte Carlo simulation can be used to obtain strength distribution functions [37, 95]. Since numerical PD analysis is time-consuming, Monte Carlo-type simulations of damage patterns are currently not feasible.

An alternative approach is to estimate the mean critical bond stretch value from experimental data.

In the elastic loading regime, the displacement vector for the configuration shown in Fig. 5.23 c) can be expressed as a function of the radial r and the transverse z coordinates as follows

$$\mathbf{u}(r, z) = u_r(r, z)\mathbf{e}_r + u_z(r, z)\mathbf{e}_z, \quad (5.7)$$

where the unit vectors \mathbf{e}_r and \mathbf{e}_z designate the radial and the lateral directions, respectively. Following the Kirchhoff plate theory, the radial and the axial displacements are assumed as follows

$$u_r(r, z) = -\frac{\partial u_z}{\partial r}z, \quad u_z(r, z) \approx u_z(r), \quad (5.8)$$

where $u_z(r)$ is defined by Equation (4.1).

For the elastic deformation regime, the results of PD analysis closely agree with those of the plate theory. Therefore, the analytical solution for the displacement vector (5.7) can be used to evaluate the maximum bond stretch. To this end, consider a bond inside the load ring radius defined by the position vectors $\mathbf{x} = r\mathbf{e}_r + z\mathbf{e}_z$ and $\mathbf{x}' = r'\mathbf{e}_r + z\mathbf{e}_z$ for $0 \leq r \leq r_{lr}$, $0 \leq r' \leq r_{lr}$ and for any $-h/2 \leq z \leq h/2$. The bond vector in the reference state is in-plane, i.e., $\boldsymbol{\xi} = (r' - r)\mathbf{e}_r$. The corresponding bond vector in the actual configuration is

$$\mathbf{Y} = \mathbf{u}' - \mathbf{u} + \boldsymbol{\xi} \quad (5.9)$$

The bond stretch is defined as

$$s = \frac{|\mathbf{Y}|}{|\boldsymbol{\xi}|} - 1 \quad (5.10)$$

With Equations (5.7) – (5.10) and (4.1), the maximum bond stretch value can be computed. To derive the explicit relation for the maximum bond stretch, assume that $s^2 \ll s < 1$. From Equation (5.9) it follows that

$$(s + 1)^2 \approx 2s + 1 = \frac{|\mathbf{Y}|^2}{|\boldsymbol{\xi}|^2} \quad (5.11)$$

The bond stretch reaches its maximum value for bonds at the bottom surface of the plate, i.e., for $z = h/2$. Using Equations (5.7)–(5.9) and (4.1), we obtain

$$\begin{aligned} \mathbf{Y} &= (r' - r)(\alpha - 1)\mathbf{e}_r + [u_z(r') - u_z(r)]\mathbf{e}_z, \\ \alpha &= \frac{3F_{\text{res}}}{4\pi h^2 E} \left[(1 - \nu)^2 \frac{r_{sr}^2 - r_{lr}^2}{R^2} + 2(1 - \nu^2) \ln \frac{r_{sr}}{r_{lr}} \right] \end{aligned} \quad (5.12)$$

From Equation (5.11), it follows that

$$2s_{\text{max}} = \alpha^2 + 2\alpha + \alpha\beta + \beta^2, \quad \beta = \frac{u_z(r') - u_z(r)}{r' - r}$$

Since $\alpha^2 \ll \alpha < 1$ and $\beta^2 \ll \beta < 1$, we obtain

$$s_{\max} = \frac{3F_{\text{res}}(1-\nu)}{4\pi h^2 E} \left[(1-\nu) \frac{r_{sr}^2 - r_{lr}^2}{R^2} + 2(1+\nu) \ln \frac{r_{sr}}{r_{lr}} \right] \quad (5.13)$$

With Equation (5.6) we obtain

$$s_{\max} = \frac{1-\nu}{E} \sigma_{\max} \quad (5.14)$$

We observe that for the homogeneous strain (stress) state at the bottom surface of the plate, inside the load ring radius, the maximum bond stretch can be related either to the applied force via Equation (5.13) or to the maximum tensile stress via Equation (5.14).

As a result, the cumulative probability of bond breakage inside the area πr_{lr}^2 can be computed as follows

$$P = 1 - \exp \left[- \left(\frac{s_{\max}}{s_{\theta}} \right)^m \right], \quad s_{\theta} = \frac{1-\nu}{E} \sigma_{\theta} \quad (5.15)$$

The mean value of the critical bond stretch is given by

$$\bar{s}_c = s_{\theta} \Gamma \left(1 + \frac{1}{m} \right)$$

With $E = 70$ GPa, $\nu = 0.22$, $\sigma_{\theta} = 191.7$ MPa and $m = 8.27$ [53] we obtain $\bar{s}_c = 2.015 \cdot 10^{-3}$. Let us compare the mean value of the critical bond stretch obtained from experimental data on fracture strength distribution with the values predicted by Equation (5.4). According to Equation (5.4), the critical bond stretch depends on the horizon size δ .

For example

- for $\delta = 2$ mm, $s_c = 2.2 \cdot 10^{-4}$,
- for $\delta = 0.1$ mm, $s_c = 9.8 \cdot 10^{-4}$,
- For $\delta = 20$ μ m, $s_c = 2.2 \cdot 10^{-3}$

We observe that, in order to use Equation (5.4), the horizon size must be set to approximately twice the mean length of surface flaws in the micrometer range. For the horizon size of 1.8 mm used in the computation of the plate specimen, Equation (5.4) underestimates the critical bond stretch by one order of magnitude. According to Equation (5.13), this would also lead to an underestimation of the critical force by one order of magnitude.

5.4.2 Analysis of damage patterns

After validating the PD solution in the elastic regime and identifying the mean value of the critical bond stretch, the results for damage patterns can be analyzed. In [53], numerical simulations with different numbers of nodes and horizon sizes were performed. It was observed that as the number of nodes increases and the horizon size decreases, damage zones become more localized. Additionally, the time to damage initiation slightly decreases with an increase in the number of nodes.

The damage patterns remain qualitatively similar across all discretization cases. However, the results presented in [53] are limited to an initially homogeneous plate and correspond only to the case 1 damage pattern. In this study, all three cases of damage patterns are analyzed.

5.4.2.1 Quasi-homogeneous plate with mean value of critical bond stretch

Figure 5.24 illustrates the damage distribution on the bottom side of the plate, assuming a constant critical bond stretch value of $2.0 \cdot 10^{-3}$. The results are plotted for different time points. In this case of an initially homogeneous plate, the formation of a ring-shaped damage zone, followed by the initiation of a series of radial cracks, can be observed. This result closely matches the findings presented in [53] for various types of node lattices and horizon sizes. Clearly, this type of damage corresponds to case 1 damage patterns observed in experiments, as shown in Figure 5.24 f).

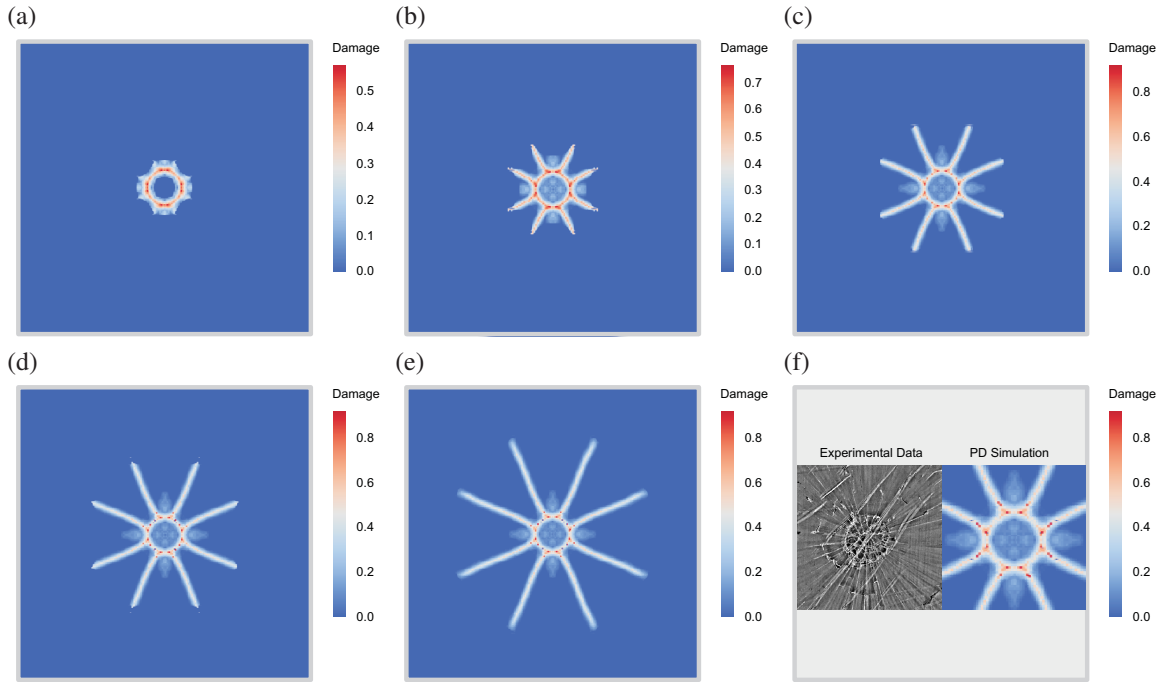


Figure 5.24: Damage distribution on the bottom side of a plate without initial imperfections (case 1).

a) $t = 51.9806$ s, b) $t = 51.9809$ s, c) $t = 51.982$ s, d) $t = 51.9826$ s, e) $t = 51.9832$ s, f) $t = 51.9856$ s, comparison with experimental damage pattern presented in [53]

5.4.2.2 Plate with initial imperfections at various locations

In the second example, a plate with an initial imperfection is considered. To model the imperfection, the bond stretch value is reduced to 10^{-4} at a node on the bottom side, located 9 mm (the load ring radius) from the midpoint of the plate. Due to this very low critical bond stretch value, damage is initiated early, and the bond family connected to that point is partially broken during the early stage of loading.

Figure 5.25 a) shows the initial damage state, featuring a narrow damage zone near the node with the reduced critical bond stretch. From that point, a non-symmetric damage pattern rapidly propagates over the bottom side of the plate within the time interval $51.9606 < t < 51.9653$ s,

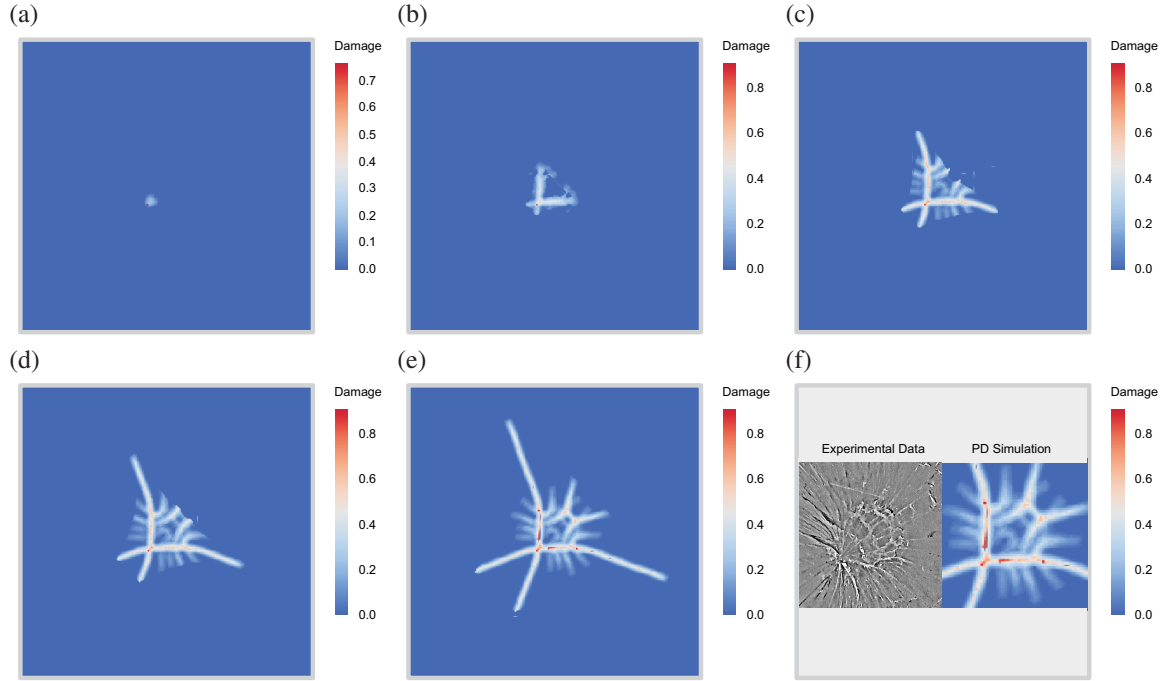


Figure 5.25: Damage distribution on the bottom side of a plate with an initial imperfection on the load ring radius at the bottom side (case 2).

a) $t = 51.9606$ s, b) $t = 51.9609$ s, c) $t = 51.9612$ s, d) $t = 51.9615$ s, e) $t = 51.9618$ s, f) $t = 51.9653$ s, comparison with experimental damage pattern presented in [53]

as shown in Fig. 5.25 b) – f). Note that, due to limitations in the applied PD damage model, crack propagation up to the final fracture state cannot be captured accurately. As a result, the simulation was terminated at $t = 51.9653$ s. Nevertheless, the final damage state, shown in Figure 5.25 f), closely resembles the case 2 damage pattern observed in experiments.

In the following case, a plate with an initial imperfection at a node on the bottom side, located 11.25 mm ($5/4$ of the load ring radius) from the central point, is analyzed. As in the previous case, the critical bond stretch at that node is set to the very low value of 10^{-4} , and damage is initiated after loading.

Figure 5.26 shows the sequence of damage states at different time points. Similar to the previous example, a non-symmetric damage pattern originating from the initial imperfection is observed. The damage state inside and near the load ring radius corresponds to the case 3 experimental data, as shown in Fig. 5.26 f).

Figure 5.27 provides a summary of the results for the three considered cases. The time to reach approximately the same damage state is shown in Fig. 5.27 a), while the corresponding force required to reach this damage state is presented in Fig. 5.27 b). The highest force value is obtained for the initially homogeneous plate (case 1), followed by the plate with an imperfection outside the load ring radius (case 3). The lowest force value is observed for Case 2, where the imperfection is located at the load ring radius. However, the difference in force values is less than 1%.

Consequently, despite the significant effect of large initial flaws on the damage pattern, they do not lead to a notable variation in mechanical strength. This result aligns with the experimental data presented in [53]. Indeed, the scatter in the experimentally obtained critical force or critical stress values cannot be attributed to different positions of damage initiation or types of damage patterns. For the three cases considered, nearly the same scatter in fracture strength was

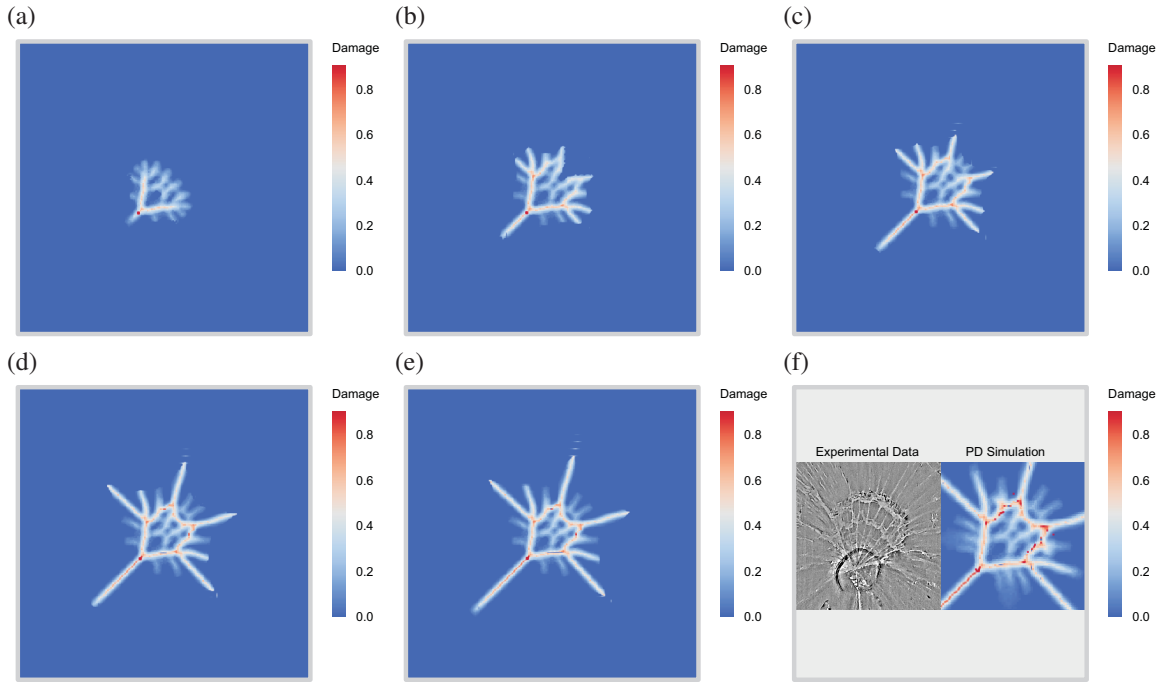


Figure 5.26: Damage distribution on the bottom side of a plate with an initial imperfection outside the load ring radius at the bottom side (case 3).

a) $t = 51.9505$ s, b) $t = 51.9507$ s, c) $t = 51.9509$ s, d) $t = 51.9513$ s, e) $t = 51.9523$ s, f) $t = 51.9653$ s, comparison with experimental damage pattern presented in [53]

observed.

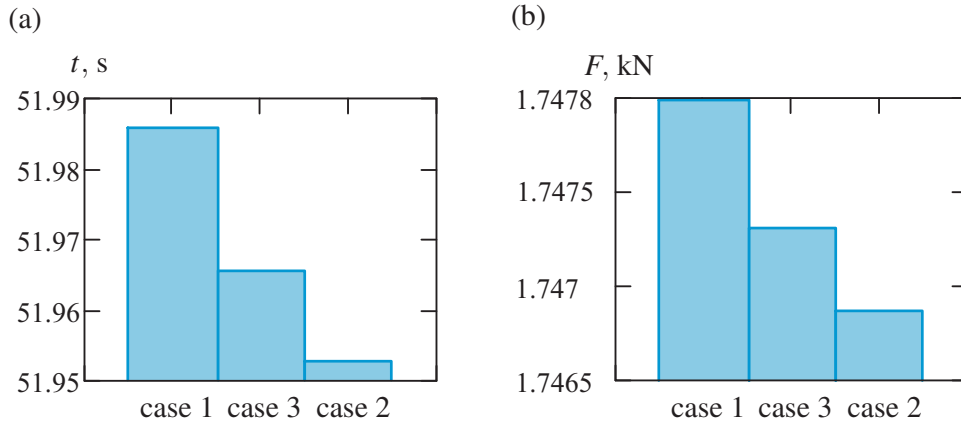


Figure 5.27: Comparison of time and force to reach final damage states for a plate without initial imperfections (case 1), with initial imperfection on the load ring radius (case 2), and with initial imperfection outside the load ring radius (case 3).

a) time to final damage state, b) force required to reach final the damage state

5.4.2.3 Plate with lower strength skin layer

For float glass plates, the strength properties of the skin layers may differ from those in the bulk. Indeed, differences in the distribution of flaws are observed between the tin and air sides [38, 39,

53, 94]. To numerically analyze the effect of the skin layer, we assume that a row of nodes on the bottom surface of the plate has a critical stretch value of $7.5 \cdot 10^{-5}$, while the remaining nodes have a value of $2 \cdot 10^{-3}$.

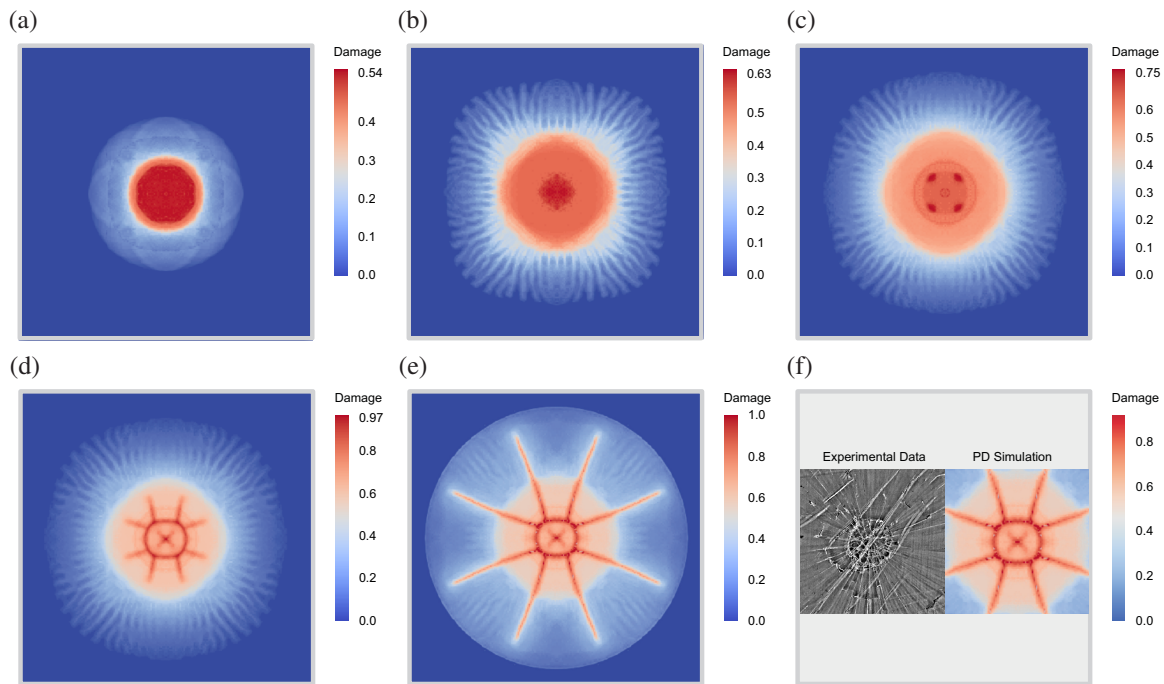


Figure 5.28: Damage distribution on the bottom side of a plate with a softer skin layer ($s_c = 7.5 \cdot 10^{-4}$) at the bottom side.

a) $t = 27.2$ s, b) $t = 34.0006$ s, c) $t = 34.0076$ s, d) $t = 34.0103$ s, e) $t = 34.0104$ s, f) $t = 34.0109$ s, comparison with experimental damage pattern presented in [53]

Figure 5.28 illustrates the damage distribution on the bottom side of a plate with a softer skin layer at different time points. In contrast to the case of a quasi-uniform plate, a circular damage zone forms, followed by finely distributed radial cracks. Once damage initiates at the bottom surface, cracks cannot propagate into the higher-strength core. Instead, as the load increases, the damage localizes in the skin layer, leading to a fine distribution of radial cracks. For this example, it can be seen that in comparison to the experiment, nearly the same fracture pattern is observed.

5.5 Influence of the random distribution of defects (flaws) on fracture force, damage and crack patterns

Previously, we investigated the influence of localized defects, single and multiple nodes, on damage initiation, propagation, and fracture patterns under quasi-static loading conditions. We also analyzed the role of surface weakening, defect position relative to the load ring, and their combined effects. To further expand the analysis, we now examine a random distribution of defects across the bottom layer of the float glass plate. This approach reflects a more realistic representation of manufacturing imperfections and their variability in size and position.

The primary goal of this section is to understand how the location, size, and distribution of defects affect the damage initiation time, crack propagation, and final fracture patterns of the glass plate. We want to consider how the presence of large and small defects inside the load ring influences damage initiation compared to defect-free regions, how the distribution of smaller flaws affects

the crack density and progression relative to larger flaws, and how the absence of defects inside the load ring affect the overall damage patterns and propagation paths.

Figure 5.29 illustrates the plate lattice with random defect placement using an exponential distribution of flaw sizes across the bottom layer of the float glass plate. The defects' normal uniform distribution through the plate's bottom side is performed. The critical stretch is set as $1.0 \cdot 10^{-4}$ for randomly distributed defect nodes, the surface nodes of the bottom layer are reduced by $s_c = 1.5 \cdot 10^{-3}$, and for all other nodes throughout the plate is $s_c = 2.0 \cdot 10^{-3}$. The plate lattice includes 6 nodes through the plate thickness with a horizon size of 1.81 mm.

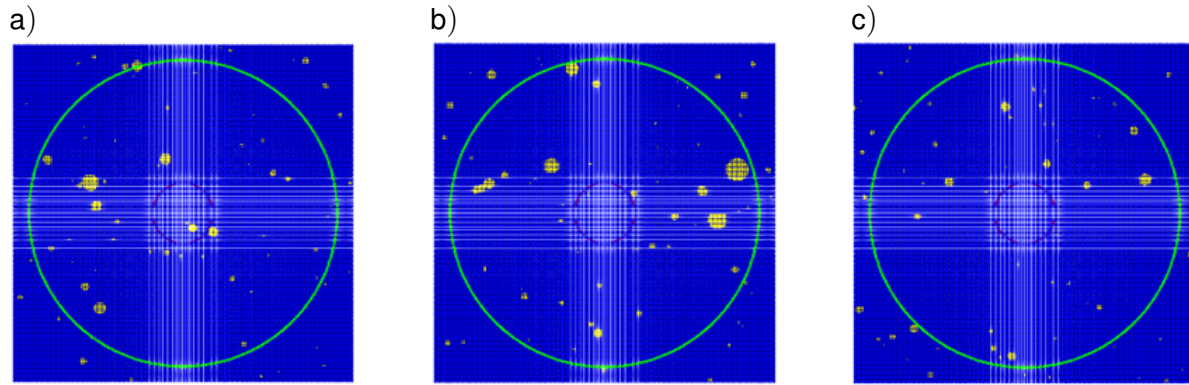


Figure 5.29: The lattice of random distribution of defects with $s_c = 1.0 \cdot 10^{-4}$ on the bottom side of a plate with $s_c = 1.5 \cdot 10^{-3}$ at the surface nodes of bottom layer.
a) first case, b) second case, c) third case

The random defects vary in size and location, which allows us to explore their influence on the damage initiation time and resulting fracture patterns.

In the first case (Figure 5.29 A), a high concentration of defects, including large and small flaws, is observed inside the load ring radius. This distribution creates a localized region of stress amplification where damage initiation is accelerated. The interaction between closely spaced defects can result in early damage initiation and more rapid crack propagation, leading to a higher density of damage patterns in the load ring area. The influence of these defects is expected to dominate the damage behavior, as they coincide with the area of maximum stress concentration under the applied load.

In the second case (Figure 5.29 B), the defects inside the load ring are predominantly small-sized flaws, with larger flaws positioned outside the load ring. While the stress concentration under the load ring still causes early damage initiation, the smaller flaws require higher localized stress to trigger bond failure. This case offers an interesting comparison to the first case, as the reduced flaw sizes may delay crack propagation compared to regions with larger defects. The damage progression and crack patterns will reflect a balance between the flaw size and stress concentration effects.

In the third case (Figure 5.29 C), no defects are present inside the load ring, and the flaws are distributed outside the load ring radius. Damage initiation is expected to follow the standard behavior observed in a plate with uniform material properties, with initiation occurring due to stress concentration under the load ring. The randomly distributed flaws outside the load ring may influence the crack propagation paths as the damage develops, but they do not alter the initiation location. This case serves as a baseline for understanding how defect-free regions within the load ring contrast with flawed regions in the earlier cases.

By comparing the three cases, we can determine the relative sensitivity of the fracture behavior to defect distribution, offering a more comprehensive understanding of real-world imperfections

in brittle materials like float glass.

Figure 5.30 illustrates the results of calculations for these three cases with damage that reached 100%.

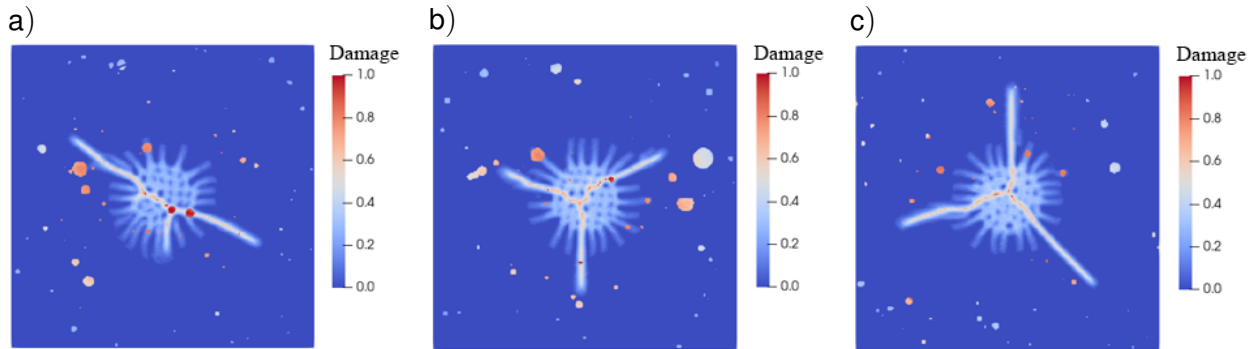


Figure 5.30: Damage distribution of random defects with $s_c = 1.0 \cdot 10^{-4}$ on the bottom side of a plate with $s_c = 1.5 \cdot 10^{-3}$ at the surface nodes of bottom layer.

a) first case $t = 34.51$ s, b) second case $t = 36.01$ s, c) third case $t = 37.01$ s

In the first case, damage begins under the load ring area and is triggered by a large defect in this area. The radial crack originates from the large flaw, passes through the defective nodes under the load ring, and propagates symmetrically outward from the load ring area. The size of the flaws plays a critical role in amplifying stress concentration. The plate reaches 100% damage at $t = 34.51$ s. Compared to the flawless model with reduced bottom surface nodes, the reduction is approximately 10.6%. The presence of a large defect near the stress concentration zone significantly accelerates damage initiation and propagation.

In the second case, damage initiates under the load ring, but the crack originates from a medium-sized defect located slightly next to the load ring radius. The crack propagates through the defective nodes under the load ring and spreads outward in a radial pattern. The proximity of the flaw to the stress concentration area influences the crack growth. The plate reaches 100% damage at $t = 36.01$ s. Compared to the flawless model with reduced bottom surface nodes, the reduction is approximately 6.7%. While the damage initiation time is shorter than in the flawless case, the reduction is less pronounced than in the first case. This highlights that smaller flaws are less effective in initiating rapid crack propagation.

In the third case, no flaws are present inside the load ring. Damage initiates under the load ring due to the stress concentration caused by the applied load. The radial cracks originate from the center of the load ring and propagate outward. The plate reaches 100% damage at $t = 37.01$ s. Compared to the flawless model with reduced bottom surface nodes, the reduction is approximately 4.1%. Unlike previous cases, the absence of flaws in the stress concentration zone delays damage initiation and propagation. This case confirms that defect size and proximity to stress-concentrated regions influence fracture behavior.

This analysis demonstrates that the fracture behavior of the glass plate is highly sensitive to the size, location, and distribution of defects. Large defects in stress-concentrated areas accelerate failure, while smaller or more distant defects have a limited influence. By considering random defect distributions, the peridynamic model provides valuable insights into the real-world fracture mechanisms of brittle materials, helping to bridge the gap between idealized and practical scenarios.

6 Summary and Outlook

The mechanical behavior of laminated and monolithic glass structures under quasi-static and dynamic loading conditions is investigated in the thesis. The influence of geometric properties, material characteristics, and manufacturing imperfections on structural behavior was explored using FEM and PD modeling techniques. The approach adopted in this work allowed the simulation of elastic behavior and critical phenomena, such as crack initiation, propagation, and the role of flaws in failure mechanisms under various loading conditions. This methodology established a foundation for more accurate, physically informed models of glass structures, which are important for ensuring reliability in engineering applications. The general information about glass structures, their mechanical behavior, modeling approaches, the actuality, and the goals of the thesis are given in Chapter 1.

Based on existing studies in the field of modeling such materials, it was concluded that a combination of FEM and PD is necessary. In this work, FEM and PD were employed as the primary modeling approaches. Chapter 2 presents the theoretical background for both methods, including a description of all types of analyses.

Chapter 3 focuses on investigating the elastic behavior of monolithic glass and LG under dynamic impact loading. The modeling process requires the reliability of computational models, so the first part of the chapter is associated with conducting a modal pre-analysis for a glass plate to construct an adequate FE-mesh and determine the frequency characteristics that are needed for subsequent dynamic analysis.

The glass plate benchmark was solved in the linear transient dynamic statement. A comparison between analytical and numerical results demonstrated a strong correlation. The visual representation of the plate modes was provided, reinforcing the validity of both the numerical and analytical approaches in capturing the plate's characteristics. For modal analysis, it is recommended to use 2 elements in the glass plate thickness to ensure a relatively high calculation speed and result accuracy.

In the next benchmark, the plate under dynamic impact is under consideration. This problem setup was selected based on the approximate analytical solution to the boundary value problem available for such plates. The comparison between the analytical and numerical solutions for displacements and stresses at different points of the glass plate showed strong agreement. As a result, this model and its parameters were applied in future analyses of more complex models and scenarios.

At the next stage, a series of calculations of the FEM model of a three-layer LG composite with variations in the impact load rate was carried out. A significant correlation was identified between mesh resolution and the accuracy of displacement prediction in the laminate (compared to literature data) at higher impact velocities. Mesh refinement near the impact zone was critical for accurately modeling displacement and stress distributions. For practical applications, using an element size of approximately 2 elements per glass layer (5 elements per LG thickness) and FE mesh size of 2 mm is recommended, balancing simulation accuracy and computational cost. In the course of further research, a series of calculations of a ball impact on a laminate with variations in the loading velocities and the thickness of the PVB interlayer were carried out. Thicker interlayers provide greater flexibility in the LG, which leads to more significant deformations than thinner interlayers. The differences in u_{max} between consecutive interlayer thicknesses 0.38 mm

with 0.76 mm and 0.76 mm with 1.52 mm are consistent across all velocities, ranging between 4.5% and 5.1%. At the same time, higher stress values are observed for thinner interlayers. The general character of the dependence of displacement on velocity for all interlayer thicknesses corresponds to a linear law. A similar picture is observed for stresses. Based on these results, the thickness of the PVB layer was chosen 1.52 mm.

Calculations with variation of plate curvature were also performed for the above-mentioned loading velocities. During the calculations, the dependence of the displacement value on the plate curvature parameter was obtained. With an increase in the curvature parameter, the displacement values decrease. The obtained results were approximated by an exponential law. For curvature parameter values less than 40 mm ($1/8$ of the plate length), the nature of the stress distribution is close to the case of a straight plate, while large values of the curvature parameter correspond to large stress values. With an increase in the curvature parameter to levels greater than 40 mm, a tendency to decrease stresses and their redistribution over the plate surface is observed. This dependence of stresses on the curvature parameter was approximated by a third-degree polynomial law.

A modal analysis was conducted for LG plates with varying curvature. The results emphasize the complex impact of curvature on their vibrational behavior, showing that natural frequencies and elastic wave distributions are highly sensitive to geometric configuration. These results offer important insights for optimizing curvature to meet specific dynamic performance criteria.

The calculations of the dependence of displacements on curvature parameter were verified with other boundary conditions, while the nature of this dependence was preserved.

The dynamic impact response of LG plates by varying the interlayer's elastic modulus and thickness was investigated. An increased interlayer Young's modulus significantly affects both displacements and stresses within the LG. As the modulus increases, the displacement values decrease, indicating a stiffer response. Conversely, the first principal stress values increase with a higher modulus, stabilizing after a certain point. Varying the interlayer thickness also influences the impact response: thicker interlayers result in increased displacements and longer contact times between the ball and plate. This indicates better stress distribution and energy absorption with thicker interlayers.

In Chapter 4 the peridynamic modeling of double-ring bending for the glass plate under quasi-static loading was described. The adequacy of the model was verified through a comparative analysis of the results obtained from peridynamic modeling and the analytical solution of the given problem in terms of displacements. The results showed good agreement, which made it possible to use the model for further investigations. A similar comparison was also conducted for various discretizations by varying the number of nodes through the plate thickness and the horizon parameter. Based on this stage, it was concluded that imperfections in the numerical procedure may cause deviation from the analytical solution. It was also established that the results are sensitive to the model parameters (horizon, lattice) and the density of glass. Additionally, a comparison was made between the results obtained using PD and FEM. The outcomes of this comparison confirm that the proposed peridynamic model can be used for further studies on glass damage.

Chapter 5 deals with the peridynamic damage modeling in a glass plate. In the first stage, the plate was subjected to quasi-static loading. A study was conducted on the influence of the critical bond stretch parameter on the crack initiation time and the crack propagation pattern. Approaches for determining this parameter were described. Based on these approaches, a range of critical stretch values was selected for parametric studies.

In the first group of simulations, a single value of the critical stretch parameter was assigned uniformly across the entire plate. This study showed that as the parameter value decreases, the initiation time also decreases, with the crack initiating on the bottom surface of the glass

plate. Overall, the crack propagation pattern initially forms a circular shape within the loading ring, followed by radial crack growth.

The second group of simulations focused on the effect of layer-dependent critical stretch on the initiation and critical time. The general trend of the initiation time depending on the critical stretch value was consistent with the previous group. However, the critical time for the lowest parameter values increased by approximately 2 times. The number of nodes through the plate thickness was also varied in this group. An increase in the number of through-thickness nodes led to a slight increase in the critical time.

The next stage of the work was an analysis of the glass plate under impact loading by a steel ball, focusing on the initiation and progression of damage patterns. In this calculation, the ball's initial velocity and the critical stretch parameter were varied. With a 5 times increase in velocity and a fixed critical stretch value, the critical time decreased by approximately 3 orders. The dependence of the critical time on the loading velocity has a decreasing character, while the maximum value of the critical bond stretch is close to linear, with a further decrease in the parameter of the critical bond stretch on the lower layer of the plate, the character becomes significantly nonlinear. Also, when the critical bond stretch parameter is reduced at the bottom surface, damage accumulates quickly under high-velocity impact. Specifically, in the high-velocity scenarios studied, the damage is highly localized beneath the impact zone and reaches 100% quickly. This indicates that the critical time remains nearly constant under such conditions. The findings suggest that once a certain impact velocity threshold is exceeded, the structural integrity of the plate fails almost immediately, resulting in a consistent failure pattern regardless of any further increase in velocity.

Further, the impact of defect location and size on the fracture behavior of glass plates under quasi-static loading was under study. The simulation showed that both the location and number of defective nodes significantly influence the critical time and fracture behavior. As defect nodes increase, the critical time drops by 7.8%. A single central defected node caused symmetric, cross-like crack propagation due to uniform stress distribution. Multiple central nodes accelerate failure but preserve symmetry if placed evenly. In the case of defects location under the load ring, increasing defects still reduces critical time, but the effect is less pronounced than in the center due to naturally high stress. Multiple defects add little influence beyond that the stress concentration already induces. On the other side, when defects are located outside the load ring, there is no change in critical time for 1 – 2 nodes; these regions are under low stress. Only with 4 nodes, early damage initiates at defect locations and propagates inward, changing the typical failure pattern. The non-defected model shows fracture behavior similar to the single-node cases in low-stress regions, confirming their minimal impact.

Also, the combined effect of lowered critical bond stretch and local defects on fracture behavior in a glass plate was investigated. Damage initiation starts at the defective node but quickly shifts to the high-stress zone under the load ring. The weakened bottom surface layer plays the dominant role in accelerating crack growth. Radial cracks emerge from the center and expand outward symmetrically. The single defect under the load ring does not influence crack paths; the weakened surface layer dictates the damage evolution. Compared to the model without surface weakening, damage initiation time is reduced by 34.6%. Total damage time increases, reflecting slower, more uniform crack growth. In the case of four defects outside the load ring, damage initiates at defect nodes due to weakened bonds and then spreads inward. A ring-shaped zone forms under the load ring, followed by radial crack growth. One crack intersects the defect group, showing some influence on the crack path. Damage initiation time drops by 29.2%, while critical time increases.

For the cases without imperfections, with defects under and outside the load ring, and with a softer skin layer at the bottom side ($7.5 \cdot 10^{-4}$) were taking out the comparison of the results of

numerical modeling with experimental data (taken from literature). The result of the comparative analysis showed good agreement with the experiment.

The last step includes an investigation of the effect of randomly distributed defects on fracture behavior. To simulate realistic manufacturing imperfections, random defects with varying sizes were introduced across the bottom layer of a glass plate. Three scenarios were analyzed to assess how defect size, location, and distribution affect damage initiation, crack propagation, and fracture patterns. For defect sizes, an exponential distribution was used. The defects' normal uniform distribution through the plate's bottom side is performed. Three different cases were considered. For the case with large and small defects inside the load ring, early damage starts at a large flaw inside the high-stress region. Also, the rapid crack propagation outward and radial cracks form were observed. Here the critical time was $t = 34.51 \text{ ms}$ (10.6% faster than flawless case). Another case with small flaws inside, and larger ones outside the load ring demonstrates that damage starts near load ring at a medium-sized flaw. Furthermore, cracks propagate radially but more slowly. The damage occurred by 6.7% faster. The last case considered no defects inside the load ring. Damage initiated under load ring due to stress concentration. Besides radial cracks forming from the center and external flaws slightly affect the crack path. For this case, the critical time is $t = 37.01 \text{ ms}$ (4.1% faster). Thus, the absence of flaws in stressed zones delays damage, large central defects significantly accelerate failure, and smaller flaws delay propagation compared to large ones.

Based on the results of this thesis, one may conclude that the deformation and strength behavior of laminated and monolithic glass structures under dynamic and quasi-static loading by employing both FEM and PD modeling approaches was investigated. The research developed and validated accurate models for simulating elastic behavior, damage initiation, and progression. The focus was on the influence of material properties and geometric parameters on the elastic performance of laminated glass, as well as the effect of discretization, horizon size, key damage parameters, and flaws on damage formation, initial crack propagation, crack patterns, and overall fracture behavior.

The following principal conclusions can be drawn from the work:

1. The ability of PD theory to take into account long-range force interactions has shown a clear advantage over FEM in problems of modeling fracture processes, in particular, the initiation and propagation of cracks.
2. FEM-based modeling of LG under impact loading successfully replicated elastic behavior and was validated with analytical solutions. The models showed that mesh resolution, ball velocity, and interlayer properties (thickness and elastic modulus) significantly affect displacement and stress distribution. The curvature parameter also influences both modal and dynamic responses.
3. PD models captured fracture behavior in monolithic glass, including crack initiation, propagation, and the effect of geometric discretization (node density, horizon parameter). Comparisons with analytical and FEM results in elastic statement confirmed the robustness of the PD approach. However, the numerical procedure (accuracy) is highly sensitive to horizon parameter and lattice density selection.
4. The critical bond stretch parameter in PD simulations was shown to be a dominant factor in determining both crack initiation time and critical time, observing damage patterns. Variation by layer and a whole plate of this parameter improved the failure modeling process of glass behavior under complex loading conditions.
5. Technological imperfections (defects) significantly influence on fracture behavior, particularly, their size, number, and location relative to high-stress regions. Central or under

ring-located defects reduced critical time and altered crack propagation, while flaws outside the stress zones had minimal effect unless present in large numbers or combined with surface weakening. These findings align well with available in literature experimental results.

6. Randomly distributed defects changed crack paths, influenced critical time, and damage patterns. Large flaws in high-stress zones reduced failure time, while smaller flaws contributed to more distributed, less aggressive damage. The statistical distribution of flaws brought the modeling of fracture behavior closer to a more realistic scenario.

The insights and methodologies developed in this thesis provide a strong foundation for future research and engineering application. Several promising directions emerge:

1. Fracture analysis of laminated glass structures: While this work focused on fracture behavior in monolithic glass panels, a crucial next step is to extend damage and fracture modeling to laminated glass systems, where interactions between glass layers and inter-layers during cracking play a major role.
2. Integration with probabilistic modeling tools: Based on the idea of random distribution, it is necessary to carry out a significant number of calculations, sufficient for further statistical analysis for enable more reliable monolithic and laminated glass structures that account for manufacturing imperfections.

References

- [1] Aenlle, M. L. and Pelayo, F. "Frequency Response of Laminated Glass Elements : Analytical Modeling and Effective Thickness". In: *Applied Mechanics Reviews* 65(March), 2013, pp. 1–13. DOI: 10.1115/1.4023929.
- [2] Altenbach, H. "Theories for laminated and sandwich plates. A review". In: *Mechanics of Composite Materials* 34(3), 1998, pp. 243–252. DOI: 10.1007/BF02256043.
- [3] Alter, C., Kolling, S., and Schneider, J. "An enhanced non-local failure criterion for laminated glass under low velocity impact". In: *International Journal of Impact Engineering* 109, 2017, pp. 342–353. DOI: 10.1016/j.ijimpeng.2017.07.014.
- [4] Aşık, M. Z., Dural, E., Yetmez, M., and Uzhan, T. "A mathematical model for the behavior of laminated uniformly curved glass beams". In: *Composites Part B: Engineering* 58, 2014, pp. 593–604. DOI: 10.1016/j.compositesb.2013.11.004.
- [5] Bahadori, M., Tekerek, E., Mathew, M., Krzysztof, M., Wisner, B., and Kontsos, A. "Composite Material Failure Model Updating Approach Leveraging Nondestructive Evaluation Data". In: *ASME J Nondestructive Evaluation* 4(August), 2021, pp. 1–16. DOI: 10.1115/1.4049781.
- [6] Ballarini, R., Pisano, G., and Royer-Carfagni, G. "The Lower Bound for Glass Strength and Its Interpretation with Generalized Weibull Statistics for Structural Applications". In: *Journal of Engineering Mechanics* 142(12), 2016, pp. 1–20. DOI: 10.1061/(asce)em.1943-7889.0001151.
- [7] Basoglu, M. F., Zerín, Z., Kefal, A., and Oterkus, E. "A computational model of peridynamic theory for deflecting behavior of crack propagation with micro-cracks". In: *Computational Materials Science* 162(November 2018), 2019, pp. 33–46. DOI: 10.1016/j.commatsci.2019.02.032.
- [8] Belytschko, T., Liu, W. K., Moran, B., and Elkhodary, K. I. *Nonlinear Finite Elements for Continua and Structures*. Second. Vol. 1. Wiley, 2014, p. 832.
- [9] Bobaru, F., Foster, J. T., Geubelle, P. H., and Silling, S. A. *Handbook of Peridynamic Modeling*. First. Vol. 1. Chapman and Hall/CRC, 2016, p. 586. DOI: 10.1201/9781315373331.
- [10] Candaş, A., Oterkus, E., and İmrak, C. E. "Dynamic Crack Propagation and Its Interaction With Micro-Cracks in an Impact Problem". In: *ASME. Journal of Engineering Materials and Technology* 143, 2021. DOI: 10.1115/1.4047746.
- [11] Chaparala, S. C., Samala, P. R., Jacobs, J. M., and Pesansky, J. D. "Dynamic Analysis of Large Specialty Glass Panels Under Ball Drop Impact — Numerical Modeling and Measurements". In: *ASME International Mechanical Engineering Congress and Exposition, Proceedings (IMECE)* 4, 2012, pp. 751–757. DOI: 10.1115/IMECE2012-89458.
- [12] Chen, S., Zang, M., Wang, D., Yoshimura, S., and Yamada, T. "Numerical analysis of impact failure of automotive laminated glass: A review". In: *Composites Part B: Engineering* 122, 2017, pp. 47–60. DOI: 10.1016/j.compositesb.2017.04.007.

- [13] Chen, X. and Chan, A. H. C. "Modelling impact fracture and fragmentation of laminated glass using the combined finite-discrete element method". In: *International Journal of Impact Engineering* 112(April 2017), 2018, pp. 15–29. DOI: 10.1016/j.ijimpeng.2017.10.007.
- [14] Chen, X. and Chan, A. H. C. "FEM, DEM and FDEM applications on impact fracture of glass and laminated glass – a review". In: *Proceedings of the Institution of Civil Engineers - Engineering and Computational Mechanics* 177(3), 2024, pp. 102–112. DOI: 10.1680/jenclm.23.00052.
- [15] Chen, X., Chan, A. H., and Yang, J. "Simulating the breakage of glass under hard body impact using the combined finite-discrete element method". In: *Computers & Structures* 177, 2016, pp. 56–68. DOI: 10.1016/j.compstruct.2016.08.010.
- [16] Dahale, M., Neale, G., Lupicini, R., Cascone, L., McGarrigle, C., Kelly, J., Archer, E., Harkin-Jones, E., and McIlhagger, A. "Effect of weave parameters on the mechanical properties of 3D woven glass composites". In: *Composite Structures* 223(October 2018), 2019, p. 9. DOI: 10.1016/j.compstruct.2019.110947.
- [17] Del Linz, P., Wang, Y., Hooper, P. A., Arora, H., Smith, D., Pascoe, L., Cormie, D., Blackman, B. R., and Dear, J. P. "Determining Material Response for Polyvinyl Butyral (PVB) in Blast Loading Situations". In: *Experimental Mechanics* 56(9), 2016, pp. 1501–1517. DOI: 10.1007/s11340-016-0179-5.
- [18] Diana, V. and Ballarini, R. "Crack kinking in isotropic and orthotropic micropolar peridynamic solids". In: *International Journal of Solids and Structures* 196-197, 2020, pp. 76–98. DOI: 10.1016/j.ijsolstr.2020.03.025.
- [19] Dondeti, S. and Tippur, H. V. "A Comparative Study of Dynamic Fracture of Soda-Lime Glass Using Photoelasticity, Digital Image Correlation and Digital Gradient Sensing Techniques". In: *Experimental Mechanics* 60(2), 2020, pp. 217–233. DOI: 10.1007/s11340-019-00549-5.
- [20] Dubé, M., Doquet, V., Constantinescu, A., George, D., Rémond, Y., and Ahzi, S. "Modeling of thermal shock-induced damage in a borosilicate glass". In: *Mechanics of Materials* 42(9), 2010, pp. 863–872. DOI: 10.1016/j.mechmat.2010.07.002.
- [21] Dural, E. "Experimental and numerical treatment of delamination in laminated glass plate structures". In: *Journal of Reinforced Plastics and Composites* 35(1), 2016, pp. 56–70. DOI: 10.1177/0731684415613163.
- [22] Dural, E. and Vural, S. "Influence of boundary conditions on the behavior of laminated glass curved beam with delamination effect: An experimental and numerical investigation". In: *Heliyon* 10(3), 2024, pp. 1–24. DOI: 10.1016/j.heliyon.2024.e24253.
- [23] Eisenträger, J., Naumenko, K., Altenbach, H., and Meenen, J. "A user-defined finite element for laminated glass panels and photovoltaic modules based on a layer-wise theory". In: *Composite Structures* 133, 2015, pp. 265–277. DOI: 10.1016/j.compstruct.2015.07.049.
- [24] Foraboschi, P. "Analytical model for laminated-glass plate". In: *Composites Part B: Engineering* 43(5), 2012, pp. 2094–2106. ISSN: 1359-8368. DOI: 10.1016/j.compositesb.2012.03.010.
- [25] Galuppi, L. and Royer-Carfagni, G. "Analytical approach à la Newmark for curved laminated glass". In: *Composites Part B: Engineering* 76, 2015, pp. 65–78. DOI: 10.1016/j.compositesb.2015.01.047.

- [26] Galuppi, L. and Royer-Carfagni, G. "A homogenized model for the post-breakage tensile behavior of laminated glass". In: *Composite Structures* 154, 2016, pp. 600–615. DOI: 10.1016/j.compstruct.2016.07.052.
- [27] Ha, Y. D. "An extended ghost interlayer model in peridynamic theory for high-velocity impact fracture of laminated glass structures". In: *Computers and Mathematics with Applications* 80(5), 2020, pp. 744–761. DOI: 10.1016/j.camwa.2020.05.003.
- [28] Hu, W., Wang, Y., Yu, J., Yen, C. F., and Bobaru, F. "Impact damage on a thin glass plate with a thin polycarbonate backing". In: *International Journal of Impact Engineering* 62, 2013, pp. 152–165. DOI: 10.1016/j.ijimpeng.2013.07.001.
- [29] Hu, Y., Liu, F., Feng, G., and Zhang, D. "Numerical Simulation of Elastic Deformation Based on Peridynamic Differential Operator". In: *ASME 2020 39th International Conference on Ocean, Offshore and Arctic Engineering. Volume 2B: Structures, Safety, and Reliability* 2B, 2020, pp. 1–10. DOI: 10.1115/OMAE2020-19015.
- [30] Imachi, M., Tanaka, S., Bui, T. Q., Oterkus, S., and Oterkus, E. "A computational approach based on ordinary state-based peridynamics with new transition bond for dynamic fracture analysis". In: *Engineering Fracture Mechanics* 206(October 2018), 2019, pp. 359–374. DOI: 10.1016/j.engfracmech.2018.11.054.
- [31] Janda, T., Schmidt, J., Hála, P., Konrád, P., Zemanová, A., Sovják, R., Zeman, J., and Šejnoha, M. "Reduced order models of elastic glass plate under low velocity impact". In: *Computers and Structures* 244, 2021. DOI: 10.1016/j.compstruc.2020.106430.
- [32] Javili, A., Morasata, R., Oterkus, E., and Oterkus, S. "Peridynamics review". In: *Mathematics and Mechanics of Solids* 24(11), 2019, pp. 3714–3739. DOI: 10.1177/1081286518803411.
- [33] Jha, P. K., Desai, P. S., Bhattacharya, D., and Lipton, R. "Peridynamics-based discrete element method (PeriDEM) model of granular systems involving breakage of arbitrarily shaped particles". In: *Journal of the Mechanics and Physics of Solids* 151(March), 2021, p. 104376. DOI: 10.1016/j.jmps.2021.104376.
- [34] Johnson, K. *Contact Mechanics*. Reprint. Cambridge University Press, 2008, p. 468.
- [35] Karpenko, O., Oterkus, S., and Oterkus, E. "An in-depth investigation of critical stretch based failure criterion in ordinary state-based peridynamics". In: *International Journal of Fracture* 226(1), 2020, pp. 97–119. DOI: 10.1007/s10704-020-00481-z.
- [36] Karpenko, O., Oterkus, S., and Oterkus, E. "Influence of Different Types of Small-Size Defects on Propagation of Macro-cracks in Brittle Materials". In: *Journal of Peridynamics and Nonlocal Modeling* 2(3), 2020, pp. 289–316. DOI: 10.1007/s42102-020-00032-z.
- [37] Kinsella, D. T. and Persson, K. "A numerical method for analysis of fracture statistics of glass and simulations of a double ring bending test". In: *Glass Structures & Engineering* 3, 2018, pp. 139–152. DOI: 10.1007/s40940-018-0063-z.
- [38] Krohn, M. H., Hellmann, J. R., Shelleman, D. L., Pantano, C. G., and Sakoske, G. E. "Biaxial flexure strength and dynamic fatigue of soda–lime–silica float glass". In: *Journal of the American Ceramic Society* 85(7), 2002, pp. 1777–1782. DOI: 10.1111/j.1151-2916.2002.tb00352.x.
- [39] Krohn, M. H., Hellmann, J. R., Shelleman, D. L., Pantano, C. G., and Sakoske, G. E. "Effect of enameling on the strength and dynamic fatigue of soda-lime-silica float glass". In: *Journal of the American Ceramic Society* 85(10), 2002, pp. 2507–2514. DOI: 10.1111/j.1151-2916.2002.tb00488.x.

- [40] Ledbetter, S. R., Walker, A. R., and Keiller, A. P. "Structural use of Glass". In: *Journal of Architectural Engineering* 12, 2006, pp. 137–150. DOI: 10.1061/(ASCE)1076-0431(2006)12:3(137).
- [41] Linz, P. D., Liang, X., Hooper, P. A., Wang, L. Z., and Dear, J. P. "An analytical solution for pre-crack behaviour of laminated glass under blast loading". In: *Composite Structures* 144, 2016, pp. 156–164. DOI: 10.1016/j.compstruct.2016.02.058.
- [42] Littlewood, D. J. "Simulation of Dynamic Fracture Using Peridynamics, Finite Element Modeling, and Contact". In: *ASME 2010 International Mechanical Engineering Congress and Exposition*, 2010, pp. 1–9. DOI: 10.1115/IMECE2010-40621.
- [43] Littlewood, D. J., Parks, M. L., Foster, J. T., Mitchell, J. A., and Diehl, P. "The Peridigm Meshfree Peridynamics Code". In: *Journal of Peridynamics and Nonlocal Modeling* 6(1), 2024, pp. 118–148. DOI: 10.1007/s42102-023-00100-0.
- [44] Lu, G. and Chen, J. "Dynamic cracking simulation by the nonlocal macro-meso-scale damage model for isotropic materials". In: *International Journal for Numerical Methods in Engineering* 122(12), 2021, pp. 3070–3099. DOI: 10.1002/nme.6654.
- [45] Madenci, E. and Oterkus, E. *Peridynamic Theory and Its Applications*. First. Springer Science & Business Media, 2014, p. 289. DOI: 10.1007/978-1-4614-8465-3.
- [46] Mehrmashhadi, J., Bahadori, M., and Bobaru, F. "On validating peridynamic models and a phase-field model for dynamic brittle fracture in glass". In: *Engineering Fracture Mechanics* 240, 2020, pp. 1–34. DOI: 10.1016/j.engfracmech.2020.107355.
- [47] Mohagheghian, I., Wang, Y., Jiang, L., Zhang, X., Guo, X., Yan, Y., Kinloch, A., and Dear, J. "Quasi-static bending and low velocity impact performance of monolithic and laminated glass windows employing chemically strengthened glass". In: *European Journal of Mechanics, A/Solids* 63, 2017, pp. 165–186. DOI: 10.1016/j.euromechsol.2017.01.006.
- [48] Müller-Braun, S., Brokmann, C., Schneider, J., and Kolling, S. "Strength of the individual glasses of curved, annealed and laminated glass used in automotive windscreens". In: *Engineering Failure Analysis* 123(June 2020), 2021, pp. 1–14. DOI: 10.1016/j.engfailanal.2021.105281.
- [49] Müller-Braun, S. and Schneider, J. "Biaxially curved glass with large radii - determination of strength using the coaxial double ring test". In: *Glass Structures and Engineering* 2(2), 2017, pp. 121–131. DOI: 10.1007/s40940-017-0050-9.
- [50] Musgraves, J. D., Hu, J., and Calvez, L. *Springer Handbook of Glass*. Springer Nature, 2019. DOI: 10.1007/978-3-319-93728-1.
- [51] Naumenko, K. and Eremeyev, V. A. "A layer-wise theory for laminated glass and photovoltaic panels". In: *Composite Structures* 112(1), 2014, pp. 283–291. DOI: 10.1016/j.compstruct.2014.02.009.
- [52] Naumenko, K. and Eremeyev, V. A. "A non-linear direct peridynamics plate theory". In: *Composite Structures* 279, 2022, p. 114728. ISSN: 0263-8223. DOI: 10.1016/j.compstruct.2021.114728.
- [53] Naumenko, K., Pander, M., and Würkner, M. "Damage patterns in float glass plates: Experiments and peridynamics analysis". In: *Theoretical and Applied Fracture Mechanics* 118(October 2021), 2022. DOI: 10.1016/j.tafmec.2022.103264.

- [54] Nguyen-Xuan, H., Phung-Van, P., and Rabczuk, T. *Proceedings of the International Conference on Advances in Computational Mechanics 2017*. August. Springer Nature Singapore Pte Ltd. 2018, 2017, pp. 1–1137. ISBN: 9789811071485.
- [55] Niazi, S., Chen, Z., and Bobaru, F. “Crack nucleation in brittle and quasi-brittle materials: A peridynamic analysis”. In: *Theoretical and Applied Fracture Mechanics* 112, 2021, p. 102855. DOI: 10.1016/j.tafmec.2020.102855.
- [56] Oñate, E. *Structural Analysis with the Finite Element Method. Linear Statics. Volume 1. Basis and Solids*. First. Vol. 1. Springer Nature, 2009. DOI: 10.1007/978-1-4020-8733-2.
- [57] Osnes, K., Børvik, T., and Hopperstad, O. S. “Testing and modelling of annealed float glass under quasi-static and dynamic loading”. In: *Engineering Fracture Mechanics* 201, 2018, pp. 107–129. DOI: 10.1016/j.engfracmech.2018.05.031.
- [58] Osnes, K., Holmen, J. K., Grue, T., and Børvik, T. “Perforation of laminated glass: An experimental and numerical study”. In: *International Journal of Impact Engineering* 156(January), 2021. DOI: 10.1016/j.ijimpeng.2021.103922.
- [59] Oterkus, E. and Oterkus, S. “Recent advances in peridynamic theory: A review”. In: *AIMS Materials Science* 11(3), 2024, pp. 515–546. DOI: 10.3934/matricsci.2024026.
- [60] Ou, S., Ou, J., Liu, J., Li, Y., Tang, B., Peng, Q., He, D., Wang, Y., Mao, Y., Chang, J., Du, F., and Lv, T. “Improving the light transmission of silica glass using silicone as an anti-reflection layer for solar panel applications”. In: *Ceramics International* 50(18, Part A), 2024, pp. 31869–31875. DOI: 10.1016/j.ceramint.2024.05.484.
- [61] Pan, Z., Yang, J., Wang, X.-E., Xie, D., and Zhao, C. “Scratch-induced micro-fracture behaviour and translational failure of glass: An experimental and numerical study”. In: *Thin-Walled Structures* 205, 2024, p. 112341. DOI: 10.1016/j.tws.2024.112341.
- [62] Patri, M. and Samui, A. B. “Chapter 29 - Glass fibre composites for aerospace and other applications”. In: *Technical Organic and Inorganic Fibres from Natural Resources*. Ed. by Mondal, M. I. H. Woodhead Publishing in Materials. Elsevier Science Ltd, 2025, pp. 795–834. ISBN: 978-0-443-15459-1. DOI: 10.1016/B978-0-443-15459-1.00021-8.
- [63] Pisano, G. and Royer-Carfagni, G. “A micromechanical derivation of the macroscopic strength statistics for pristine or corroded/abraded float glass”. In: *Journal of the European Ceramic Society* 37(13), 2017, pp. 4197–4206. DOI: 10.1016/j.jeurceramsoc.2017.04.046.
- [64] Pisano, G., Royer Carfagni, G., and Schneider, J. “Statistical interference of crack healing on the strength of thermally-treated glass. Experiments and modelling”. In: *Engineering Fracture Mechanics* 205(November), 2019, pp. 511–531. DOI: 10.1016/j.engfracmech.2018.11.025.
- [65] Quinn, G. D. and Swab, J. J. “Fracture toughness of glasses as measured by the SCF and SEPB methods”. In: *Journal of the European Ceramic Society* 37(14), 2017, pp. 4243–4257. DOI: 10.1016/j.jeurceramsoc.2017.05.012.
- [66] Raza, M. A., Tao, S., Pei, P., Dar, U. A., Atif, M., Sheikh, M. Z., Gao, G., and Tang, Z. “Characterizing the flexural/damage behavior of Aluminosilicate glass at low/high loading rates: Application of SHPB for mode-I loading of laminated glass”. In: *Composite Structures* 329, 2024, p. 117816. ISSN: 0263-8223. DOI: <https://doi.org/10.1016/j.compstruct.2023.117816>.

- [67] Reddy, J. N. *Introduction to the Finite Element Method*. Fourth. Vol. 1. 1. McGraw-Hill Education, 2019, p. 1151. ISBN: 978-1-25-986190-1.
- [68] Ren, H., Zhuang, X., and Rabczuk, T. “Dual-horizon peridynamics: A stable solution to varying horizons”. In: *Computer Methods in Applied Mechanics and Engineering* 318, 2017, pp. 762–782. DOI: 10.1016/j.cma.2016.12.031.
- [69] Rin, N. and Han, C. “Lifetime prediction method for moisture-induced degradation of glass-to-glass solar cell modules using spatially distributed diode model”. In: *Solar Energy Materials and Solar Cells* 225(December 2020), 2021, pp. 1–14. DOI: 10.1016/j.solmat.2021.111052.
- [70] Rudshaug, J., Aasen, K. O., Hopperstad, O. S., and Børvik, T. “A physically based strength prediction model for glass”. In: *International Journal of Solids and Structures* 285(October), 2023, p. 16. DOI: 10.1016/j.ijsolstr.2023.112548.
- [71] Samieian, M. A., Cormie, D., Smith, D., Wholey, W., Blackman, B. R., Dear, J. P., and Hooper, P. A. “On the bonding between glass and PVB in laminated glass”. In: *Engineering Fracture Mechanics* 214(October 2018), 2019, pp. 504–519. DOI: 10.1016/j.engfracmech.2019.04.006.
- [72] Sayyed, M. I. and Lakshminarayana, G. “Structural, thermal, optical features and shielding parameters investigations of optical glasses for gamma radiation shielding and defense applications”. In: *Journal of Non-Crystalline Solids* 487(January), 2018, pp. 53–59. DOI: 10.1016/j.jnoncrysol.2018.02.014.
- [73] Schmidt, J., Zemanová, A., Zeman, J., and Šejnoha, M. “Phase-field fracture modelling of thin monolithic and laminated glass plates under quasi-static bending”. In: *Materials* 13(22), 2020, pp. 1–29. DOI: 10.3390/ma13225153.
- [74] Schulze, S.-H., Pander, M., Naumenko, K., and Altenbach, H. “Analysis of laminated glass beams for photovoltaic applications”. In: *International Journal of Solids and Structures* 49(15), 2012, pp. 2027–2036. ISSN: 0020-7683. DOI: 10.1016/j.ijsolstr.2012.03.028.
- [75] Shahriari, M. and Saeidi Gogarchin, H. “Numerical investigation of the impact fracture performance of a composite laminated windshield considering the Park-Paulinho-Roesler cohesive zone model”. In: *Composite Structures* 249, 2020, p. 112568. DOI: 10.1016/j.compstruct.2020.112568.
- [76] Shelby, J. E. *Introduction to Glass Science and Technology*. Royal Society of Chemistry, Oct. 2020. ISBN: 0-85404-639-9. DOI: 10.1039/9781839169229.
- [77] Shetty, M., Wei, J., Dharani, L., and Stutts, D. “Analysis of Damage in Laminated Architectural Glazing Subjected to Wind Loading and Windborne Debris Impact”. In: *Buildings* 3(2), 2013, pp. 422–441. DOI: 10.3390/buildings3020422.
- [78] Shitanoki, Y., Bennison, S., and Koike, Y. “Analytic Models of a Thin Glass – Polymer Laminate and Development of a Rational Engineering Design Methodology”. In: *Journal of Applied Mechanics* 81, 2014, pp. 1–7. DOI: 10.1115/1.4028902.
- [79] Shitanoki, Y., Bennison, S. J., and Koike, Y. “Structural behavior thin glass ionomer laminates with optimized specific strength and stiffness”. In: *Composite Structures* 125, 2015, pp. 615–620. DOI: 10.1016/j.compstruct.2015.02.013.
- [80] Silling, S. A. “Reformulation of elasticity theory for discontinuities and long-range forces”. In: *Journal of the Mechanics and Physics of Solids* 48(1), 2000, pp. 175–209. DOI: 10.1016/S0022-5096(99)00029-0.

- [81] Silling, S. A. and Askari, E. "Peridynamic Modeling of Impact Damage". In: *ASME/JSME 2004 Pressure Vessels and Piping Conference. Problems Involving Thermal Hydraulics, Liquid Sloshing, and Extreme Loads on Structures*. 489, 2004, pp. 197–205. DOI: 10.1115/PVP2004-3049.
- [82] Silling, S. A. and Askari, E. "A meshfree method based on the peridynamic model of solid mechanics". In: *Computers and Structures* 83(17-18), 2005, pp. 1526–1535. DOI: 10.1016/j.compstruc.2004.11.026.
- [83] Silling, S. A., Epton, M., Weckner, O., Xu, J., and Askari, E. "Peridynamic states and constitutive modeling". In: *Journal of Elasticity* 88(July), 2007, pp. 151–184. DOI: 10.1007/s10659-007-9125-1.
- [84] Silling, S. A. and Lehoucq, R. B. *Peridynamic Theory of Solid Mechanics*. Vol. 44. Elsevier, 2010, pp. 73–168. DOI: 10.1016/S0065-2156(10)44002-8.
- [85] Tan, S., Yao, X., Long, S., Zhang, X., and Zang, S. "Static and dynamic strength of soda-lime glass under combined compression-shear loading". In: *Journal of Non-Crystalline Solids* 516, 2019, pp. 14–25. DOI: 10.1016/j.jnoncrysol.2019.04.024.
- [86] Teotia, M. and Soni, R. K. "Applications of finite element modelling in failure analysis of laminated glass composites: A review". In: *Engineering Failure Analysis* 94, 2018, pp. 412–437. DOI: 10.1016/j.engfailanal.2018.08.016.
- [87] Thiemeier, T., Brückner-Foit, A., and Kölker, H. "Influence of the fracture criterion on the failure prediction of ceramics loaded in biaxial flexure". In: *Journal of the American Ceramic Society* 74(1), 1991, pp. 48–52. DOI: 10.1111/j.1151-2916.1991.tb07295.x.
- [88] Timoshenko, S. and Woinowsky-Krieger, S. *Theory of Plates and Shells*. Second. McGRAW-HILL, New York, 1959, p. 580.
- [89] Topbas, A. "An overview of the state-of-the-art report for glass structures". In: *Proceedings of the AEI 2008 Conference - AEI 2008: Building Integration Solutions* 328(September 2008), 2008. DOI: 10.1061/41002(328)35.
- [90] Vazic, B., Wang, H., Diyaroglu, C., Oterkus, S., and Oterkus, E. "Dynamic propagation of a macrocrack interacting with parallel small cracks". In: *AIMS Materials Science* 4(1), 2017, pp. 118–136. DOI: 10.3934/matensci.2017.1.118.
- [91] Vedrtam, A. and Pawar, S. J. "Experimental and simulation studies on fracture of laminated glass having polyvinyl butyral and ethyl vinyl acetate interlayers of different critical thicknesses due to impact load". In: 58(6), 2017, pp. 169–178. DOI: 10.13036/17533546.58.6.005.
- [92] Vedrtam, A. and Pawar, S. J. "Laminated plate theories and fracture of laminated glass plate – A review". In: *Engineering Fracture Mechanics* 186, 2017, pp. 316–330. DOI: <https://doi.org/10.1016/j.engfracmech.2017.10.020>.
- [93] Weibull, W. "A Statistical Distribution Function of Wide Applicability". In: *Journal of Applied Mechanics* 18(3), Sept. 1951, pp. 293–297. DOI: 10.1115/1.4010337.
- [94] Wereszczak, A. A., Ferber, M. K., and Musselwhite, W. "Method for identifying and mapping flaw size distributions on glass surfaces for predicting mechanical response". In: *International Journal of Applied Glass Science* 5(1), 2014, pp. 16–21. DOI: 10.1111/ijag.12059.
- [95] Yankelevsky, D. Z. "Strength prediction of annealed glass plates—A new model". In: *Engineering Structures* 79, 2014, pp. 244–255. DOI: 10.1016/j.engstruct.2014.08.017.

- [96] Yu, H. and Li, S. "On energy release rates in Peridynamics". In: *Journal of the Mechanics and Physics of Solids* 142, 2020, p. 104024. DOI: 10.1016/j.jmps.2020.104024.
- [97] Zemanová, A., Zeman, J., and Šejnoha, M. "Comparison of viscoelastic finite element models for laminated glass beams". In: *International Journal of Mechanical Sciences* 131-132(May), 2017, pp. 380–395. DOI: 10.1016/j.ijmecsci.2017.05.035.
- [98] Zhang, X., Liu, H., Maharaj, C., Zheng, M., Mohagheghian, I., Zhang, G., Yan, Y., and Dear, J. P. "Impact response of laminated glass with varying interlayer materials". In: *International Journal of Impact Engineering* 139(September 2019), 2020, p. 15. DOI: 10.1016/j.ijimpeng.2020.103505.
- [99] Zhang, X., Hao, H., and Ma, G. "Laboratory test and numerical simulation of laminated glass window vulnerability to debris impact". In: *International Journal of Impact Engineering* 55, 2013, pp. 49–62. DOI: 10.1016/j.ijimpeng.2013.01.002.
- [100] Zhang, X., Hao, H., and Ma, G. "Dynamic material model of annealed soda-lime glass". In: *International Journal of Impact Engineering* 77, 2015, pp. 108–119. DOI: 10.1016/j.ijimpeng.2014.11.016.
- [101] Zienkiewicz, O., Taylor, R., and Zhu, J. *The Finite Element Method: Its Basis and Fundamentals*. Sixth. 1. Elsevier, 2005, p. 802.
- [102] Zienkiewicz, O., Taylor, R., and Zhu, J. *The Finite Element Method: Its Basis and Fundamentals*. Seventh. Elsevier Ltd., 2013, p. 714. DOI: 10.1016/C2009-0-24909-9.

Publications

Articles

1. Naumenko, K., Larin, O., Sukhanova, O., and Pander, M. "Towards the classification and numerical prediction of fracture patterns in float glass using peridynamics". In: *Engineering Failure Analysis* 180, 2025, 109802. DOI: 10.1016/j.engfailanal.2025.109802.
2. Sukhanova, O., Larin, O., and Naumenko, K. "Investigation of Interlayer Influence on the Dynamic Impact Response of the Laminated Glass Plate". In: *PhD Seminar of the Faculty of Mechanical and Systems Engineering, Esslingen University*. Springer Nature Switzerland, 2025, pp. 20–30. DOI: 10.1007/978-3-031-79093-5_2.
3. Altenbach, H., Larin, O., Naumenko, K., Sukhanova, O., and Wurfner, M. "Elastic plate under low velocity impact: Classical continuum mechanics vs peridynamics analysis". In: *AIMS Materials Science* 9(5), 2022, pp. 702–718. DOI: 10.3934/matricsci.2022043.
4. Sukhanova, O., Larin, O., Naumenko, K., and Altenbach, H. "Dynamics of Curved Laminated Glass Composite Panels Under Impact Loading". In: *Nonlinear Mechanics of Complex Structures*. *Advanced Structured Materials*, vol. 157. Springer, Cham, 2021. DOI: 10.1007/978-3-030-75890-5_6.
5. Sukhanova, O., and Larin, O. "Linear dynamic properties in curved laminated glasses". In: *Bulletin of the National Technical University "KhPI". Ser.: Dynamics and Strength of Machines* 1, 2021, pp. 44–47. DOI: 10.20998/2078-9130.2021.1.230161.
6. Sukhanova, O., Larin, O., and Ziętek, B. "Dynamics of glass windows in mining vehicles under the impacts of rock pieces: numerical and analytical comparison for computational models validation". In: *IOP Conference Series: Earth and Environmental Science* 942, 2021, 012009. DOI: 10.1088/1755-1315/942/1/012009.
7. Sukhanova, O., and Larin, O. "Analysis of the dynamics of laminated glass composite panels under impact loading". In: *Visnyk TNTU (Tern.)* 98(2), 2020, pp. 24–32. DOI: 10.33108/visnyk_tntu2020.02.024.
8. Sukhanova, O., and Larin, O. "Analysis of the dynamics of laminated composite panels with different glass curvatures under impact loading". In: *Bulletin of the National Technical University "KhPI". Ser.: Dynamics and Strength of Machines* 1, 2020. (ukr).

Conference contributions

1. Sukhanova, O., Larin, O., and Naumenko, K. "Peridynamic modeling of damage in float glass with distribution of initial flaws". In: *Euromech Colloquium 643 – Advances in Peridynamic Material Modeling*. Venice, Italy, Sept. 25–27, 2024.
2. Sukhanova, O., Larin, O., and Naumenko, K. "Peridynamics modeling of damage in glass plate with initial surface imperfections". In: *Peridynamic Day*. DLR Braunschweig, Germany, Aug. 20, 2024.
3. Sukhanova, O., Larin, O., and Naumenko, K. "Investigation of Interlayer Influence on the Dynamic Impact Response of the Laminated Glass Plate". In: *PhD Seminar of the Faculty*

of Mechanical and Systems Engineering, Esslingen University. June 21, 2024.

4. Sukhanova, O. "Analysis of laminated glass structures under dynamic impact loading". In: DAAD Meeting for Scholarship Holders. Leipzig, Germany, Mar. 15–17, 2024.
5. Sukhanova, O., and Larin, O. "Study of the influence of the curvature of a flat double-glazed window on the spectrum of its natural frequencies and the form of oscillations". In: MicroCAD 2021. (ukr).
6. Sukhanova, O., Larin, O., and Ziętek, B. "Dynamics of glass windows in mining vehicles under the impacts of rock pieces: numerical and analytical comparison for computational models validation". In: XXI Conference of PhD Students and Young Scientists, 2021.
7. Sukhanova, O., and Larin, O. "Analysis of laminated glass structures under impact loading". In: XV International Scientific and Practical Conference of Master's and Postgraduate Students "Theoretical and Practical Research of Young Scientists". Dec. 1–3, 2021.
8. Sukhanova, O., Larin, O., Naumenko, K., and Altenbach, H. "Dynamics of curved laminated glass composite panels under impact loading". In: 6th International Conference NONLINEAR DYNAMICS. 2020.